FACULDADE DE ENGENHARIA DA UNIVERSIDADE DO PORTO

Modelling and simulation of plasma thrusters for electric propulsion technologies

Victor H. Granados

PROGRAMA DOUTORAL EM ENGENHARIA FÍSICA

Thesis prepared to obtain the PhD. Degree in Engineering Physics

Supervisor: Paulo Manuel de Araújo Sá, PhD.

Second Supervisor: Mario J. Pinheiro, PhD.

January 22nd, 2018

Modelling and simulation of plasma thrusters for electric propulsion technologies

Victor H. Granados

Thesis prepared to obtain the PhD. Degree in Engineering Physics

Approved by

President: Paulo Manuel Salgado Tavares de Castro, PhD.

Referee: Mario Merino Martínez, PhD.

Referee: Jorge Manuel Amaro Henriques Loureiro, PhD.

Referee: Mario José Gonçalves Pinheiro, PhD.

Referee: Ivo Yves Vieira, PhD.

Referee: João Bernardo Lares Moreira de Campos, PhD.

Referee: Carlos Daniel Diogo Matias Pintassilgo, PhD.

January 22nd, 2018

Abstract

Nowadays we find an increasing interest for low-thrust, high-specific-impulse, thrusters since the aerospace industry has moved towards miniaturization of satellites, which demands high efficiency in fuel consumption. Deep-space exploration has also become of interest for human spaceflights, where travel times are key to the feasibility of the missions. Plasma thrusters are filling in the gap of the new era of space exploration where spacecrafts and satellites need to either travel long distances or orbit for long periods of time.

The electrohydrodynamic (EHD) thruster is a plasma-based propulsion technology system that has been studied in the past mostly with simplistic one-dimensional models due to the lack of computation capabilities and understanding of the physics involved. A new two-dimensional, self-consistent model for EHD single-stage thrusters is proposed in order to understand its operation under different conditions (e.g., gas pressure, gas temperature, geometry of electrodes). The model is employed with three working gases (argon, nitrogen and oxygen) and it is flexible for inclusion of any desired gas, even mixtures, given all of its required characteristics (electronic and/or vibrational states, diffusion and mobility coefficients, etc). Three different geometries for the EHD thruster were studied and compared in terms of performance parameters. The secondary electron emission from the cathode was included as the main mechanism for sustaining the discharge by introducing secondary electrons into the plasma bulk. The considered EHD processes interlock the incompressible gas dynamics, the physics of ionized gases, the accelerating electric field, and the migration of ions in the drift-diffusion approximation. The model was solved using finite-element techniques in a two-dimensional axisymmetric domain considering the appropriate boundary conditions that apply to the nominal operation of an EHD thruster.

The variables that impact the performance of the EHD thrusters were found and described in order to understand their role on the weakly-ionized plasma discharge and gas flow generation. The variation of the geometry of the electrodes and their separation sheds light into how their differences change the gas flow profile and overall performance.

Resumo

Hoje em dia encontramos um interesse cada vez maior nos propulsores de baixa impulsão e alto impulso especifico, já que a industria aeroespacial tem-se movido para a miniaturização de satélites, os quais requerem alta eficiência no consumo de combustível. A exploração do espaço profundo tem-se tornado de interesse para os voos espaciais tripulados, onde os tempos de viagem são chave para a fiabilidade das missões. Os propulsores a plasma estão a preencher a lacuna da nova era de exploração espacial onde as naves e os satélites podem viajar longas distancias ou orbitar por longos períodos de tempo.

O propulsor electrohidrodinâmico (EHD) é uma tecnologia de propulsão baseada em plasma que tem sido estudada no passado maioritariamente com modelos unidimensionais simplistas devido à falta de capacidades computacionais e entendimento da física envolvida. Neste trabalho é proposto um novo modelo bidimensional e autoconsistente de um propulsor com apenas um andar para entender a sua operação sobre diversas condições (e.g., pressão do gás, temperatura do gás, geometria dos elétrodos). No modelo são usados três gases de operação (árgon, azoto e oxigénio) e é flexível para a inclusão de qualquer gás desejado, incluindo misturas, desde que sejam dadas todas as suas caraterísticas requeridas. Três geometrias diferentes para o propulsor EHD foram estudadas e comparadas em termos de parâmetros de desempenho (força de propulsão, velocidade de exaustão do gas, quociente propulsão-potência, etc). A emissão de eletrões secundários do cátodo foi incluída como o mecanismo principal para manter a descarga ao introduzir eletrões secundários no volume do plasma. Os procesos EHD considerados ligam a dinâmica do gás incompresível, a física dos gases ionizados, o campo elétrico acelerador e a migração de iões na aproximação de difusão livre. O modelo foi resolvido usando técnicas de elementos finitos em um domínio bidimensional axisimétrico, considerando as condições de fronteira apropriadas que aplicam a operação nominal de um propulsor EHD.

As variáveis que têm impacto no desempenho dos propulsores EHD foram encontradas e descritas para entender o seu papel na descarga do plasma fracamente ionizado e a geração do fluido de gás. A variação da geometria dos elétrodos e a separação entre estes lançam luz na forma como as suas diferenças modificam o perfil de fluido do gás e o desempenho do propulsor em geral.

Acknowledgments

I wish to thank the *Ministerio de Ciencia, Tecnología y Telecomunicaciones* (MICITT) from the government of the Republic of Costa Rica for supporting my professional endeavors with its scholarship program *Fondo de Incentivos del Programa de Posgrados*. A valuable aid to this Costa Rican trying to follow his dreams away from home.

I also extend my gratitude to my advisers, the professors Paulo Araújo Sá, PhD and Mario J. Pinheiro, PhD, both whom have stood by my side during the past years teaching me the values of scientific production. Their guidance and encouragement will remain forever imprinted in my professional career. I wish to make you proud.

To the anonymous referees of my articles, experts on the field of plasma physics, whose contributions helped to polish the production value of my work, and by extension the present thesis document.

A word of acknowledgment to the *Centro de Estudos de Fenómenos de Transporte* (CEFT), from the Engineering Faculty of Porto University (FEUP) for their welcoming reception.

I want to thank the *Departamento de Engenharia Física* (DEF), from the Engineering Faculty of Porto University (FEUP) and its members, for receiving me with open arms and offering their support and collaboration. Without them, this thesis would have taken longer to complete.

To my caring parents: Miriam and Hugo, and to my beloved sister Fabiola, they have supported me blindly over the years in my pursue of academic excellence, this accomplishment goes to you.

To my colleagues and friends: Nuno Gomes, PhD, Gabriela Ruphuy, PhD, and Eng. Mario Saenz, which made this bumpy road a lot easier by being there at the right moments.

To my best friend Vitor Laranjeira and his family, whom have made me feel at home in Portugal throughout the years, they are family now. *Muito obrigado*.

The Author

"-But, after all, what do you get with analytically knowing
the exact position of an electron around the atom at all times?
-Uhm... a Nobel Prize!"

Mario Saenz and Victor Granados about the inherent probabilistic characteristics of nature.

Contents

List of Figures

List of Tables

List of Abbreviations

$\mathbf{B}$	Magnetic field vector [T].
$\mathbf{E}$	Electric field vector [V.m^{-1}].
$\mathbf{J}$	Current density vector [A.m^{-2}].
$\mathbf{u}$	Fluid velocity vector [m.s^{-1}].
I_{sp}	Specific Impulse [s].
T	Thrust [N].
T_g	Gas temperature [K].
T_e	Electron temperature [eV].
d	Distance between electrodes [m].
ρ_c	Space charge density [C.m^{-3}].
ε_0	Permittivity of vacuum, $8.854187817... \times 10^{-12}$ [F.m^{-1}].
n_e	Electron density [m^{-3}].
n_ε	Electron energy density [eV.m^{-3}].
n_j	Ion density of species j [m^{-3}].
$\boldsymbol{\mu}_e$	Electron mobility tensor [m^2.V^{-1}.s^{-1}].
$\boldsymbol{\mu}_\varepsilon$	Electron energy mobility tensor [m^2.V^{-1}.s^{-1}].
$\mathbf{D}_e$	Electron diffusivity tensor [m^2.s^{-1}].
$\mathbf{D}_\varepsilon$	Electron energy diffusivity tensor [m^2.s^{-1}].
η	Dynamic viscosity [Pa.s].
ρ_f	Fluid density [kg.m^{-3}].
p	Pressure [Pa].
R_b	Ballast resistance [MΩ].
C_b	Blocking capacitance [pF].
TWR	Thrust-to-weight ratio.
T/P ratio	Thrust-to-power ratio [N.W^{-1}].
RC	Resistive-Capacitive.
RF	Radio Frequency.
ECR	Electron Cyclotron Resonance.
ICR	Ion Cyclotron Resonance.
EP	Electric Propulsion.
EHD	Electrohydrodynamic.
FEEP	Field Emission Electric Propulsion.
HDLT	Helicon Double Layer Thruster.
MPD	Magnetoplasmadynamic.
VASIMR	Variable Specific Impulse Magnetoplasma Rocket.
NASA	National Aeronautics and Space Administration (U.S.A federal agency).
ICH	Ion Cyclotron Heating.
SEE	Secondary Electron Emission.
SEEC	Secondary Electron Emission Coefficient, γ_i.

Chapter 1

Introduction

1.1 Motivation

The fundamental motivation for the development of this study lies down on the fact that plasma rockets are technologies conceived for deep-space exploration and satellite operation, promising to supplement and even replace chemical rockets used nowadays in traditional spacecrafts for such purposes.

The electrohydrodynamic (EHD) thrusters are plasma-based devices that produce a ionic flow between two or more electrodes by ionizing the gas surrounding one or more electrodes and transporting the charged species with its electric field, such transport of ions results in collisions with neutral species and creates a drag on the same direction of the ionized stream by momentum exchange. These devices have the advantage of possessing no moving parts and only employing an electric field in order to operate.

Applications of electrohydrodynamics also include flow control for the layers of air adjacent to wings in airplanes, pumps for extra-terrestrial vehicles or probes where movable parts filled with dust may become an issue; furthermore, there is a recent interest on the cooling of electronics by eliminating the noise-producing fan and replacing it with silent localized EHD pumps.

Canning et al. (2004) conducted a series of experiments for EHD devices (called Asymmetrical Capacitor Thrusters) for NASA and successfully compared his results to a simple one-dimensional model. Additionally, Masuyama and Barret (2013) recently rose the question about the potential use of EHD thrusters for use in drones and other aircrafts by means of experimenting with single and dual stage configurations for air under atmospheric pressure and by pointing out that the thrust-to-power ratio (T/P ratio) is typically higher than in other aircraft engines.

Currently, the models for the EHD thrusters are still lacking from the literature for higher-than-one dimensional analysis and it is of interest in the scientific community to understand the variables that affect their performance and how they bear upon them. In order to fill in the knowledge gap, the present research introduces a self-consistent two-dimensional model of a single stage EHD thruster and simulates under different electrodes's geometrical configurations, working gases, and other key conditions; and it finds steady-state solutions that sheds light into the

operation of these devices.

The present work comprises a comparative study between different electric propulsion technologies employed in rockets and their advantages and disadvantages for space travel, along with a advancement on the characterization of an specific plasma thruster (EHD) which currently lacks a thorough study.

1.2 Objectives

The present work contains the first two initial objectives in order to contextualize the reader into the topic of electrohydrodynamic (EHD) thrusters. The following objectives comprise the three main objectives, where the focus steers into the original contribution of the author in the field of EHD propulsion.

1. To identify the basic variables and parameters related to rocket propulsion, using chemical rockets as the basis.

2. To compare plasma propulsion technologies with other current propulsion systems for spacecrafts.

3. To model and simulate electrostatic thrusters using finite element methods in order to prove its applicability for more complex configurations.

4. To compare the performance of EHD thrusters using three different working gases and three different cathode geometries.

5. To characterize the effect of the most relevant parameters in the performance of the electrohydrodynamic (EHD) thrusters in order to understand their role in the design process of these thrusters.

1.3 Scope of work

The present work comprises the modeling and simulation of EHD thrusters at low pressures ([0.5-100] Torr). The pressure was not increased further because the species present in the discharge vary alongside the pressure and the model would have to change the chemical kinetics in order to perform such increase, which was not the focus of the study. The proposed model presented is two-dimension axysimmetrical, meaning that we assume all of the physical characteristics and properties to be independent of the azimuthal coordinate in a cylindrical coordinate system (axis of symmetry is $\hat{z}$). The thruster is single-staged which implies the use of only two electrodes -an anode and a cathode-. Multi-stage thrusters, although exhibit merit for its study, do not lie within the scope of the current work.

Three working gases are employed for the simulation of the EHD thrusters, i.e. argon, nitrogen and oxygen; the species for the modeling of each gas only considers the main ground-state molecules and representative ions, and excludes its vibrational and rotational states (with the exception of the atomic argon, presenting a compound of electronically excited species into one species). The model is supposed to characterize the trend of the thruster's behavior and adding

more species to the model is expected to improve it, although it will also significantly increase the computational times required to find steady-state solutions since the increment in species also represents a steep increase in the reactions needed to include them in the kinetics model. More gases may be studied under the same model by adding their properties such as chemical kinetics, surface reactions, dynamic viscosity, etc.

There are different methods to represent the gas and the dynamics of its molecules in a plasma discharge and the composition of the working gas on the EHD thruster depends on several factors such as pressure, gas temperature, electron temperature and reduced electric field (E/N). The amount of reactions that represent the specific gas dynamics is not well established in the literature for the studied cases, although a set of representative reactions are typically chosen according to the conditions of the discharge. For the case of the electron-impact reactions we need to use statistical data in order to find their influence on each specific discharge, which is done by assuming a Maxwellian electron energy distribution function (EEDF) since those reaction rates are calculated all over the space (the reduced electric field is not constant). An over estimation of the higher-energy electron population is carried when assuming a Maxwellian EEDF and the typical action to correct it is by solving the kinetic Boltzmann equation for electrons in order to have a more accurate EEDF, but since the reduced electric field is non-constant over the simulation region the calculations proved to be unpractical and it was decided to maintain a Maxwellian EEDF.

1.4 Contribution to the field of study

A new self-consistent two-dimensional axysimmetrical model for EHD thrusters is introduced, considering a range of gases (along with their most representative ground-state heavy species and ions) and three different cathode geometries. Steady-state solutions are presented and compared in between.

Simulations of the DC discharges at low pressure, i.e., [0.5-100] Torr coupled with fluid dynamics through the Navier-Stokes equation. Previous models found on literature consider the gases at atmospheric pressure and/or are not fully coupled with the fluid dynamics of the phenomena, instead they either assume a constant fluid velocity along the space or consider a zero value in their equations and most of them do not include the volume force (electrostatic Lorentz force) that needs to be simultaneously solved with the rest of the differential equations on each step.

Understanding of the influence of gas pressure, gas temperature, discharge current, secondary electron emission and gap between electrodes in the performance parameters for a two-dimensional situation. Analytical models for EHD thrusters currently consider only one-dimensional cases, which do not scale properly when the electrodes shapes change and specially when the cathode is hallow. Most geometries studied so far employ spherical cathodes placed on the axis of symmetry, not convenient for thrust production purposes.

The work developed on this thesis produced three articles on a peer-reviewed journal dedicated to the plasma physics subject:

1. Granados, Victor H., Pinheiro, Mario J., and Sá, Paulo A., Electrostatic propulsion device for aerodynamics applications, Physics of Plasmas, 23(7), 073514 (2016). doi: 10.1063/1.4958815.

2. Granados, Victor H., Pinheiro, Mario J., and Sá, Paulo A., Single-stage EHD thruster response to several simulation conditions in nitrogen gas. Physics of Plasmas, 24(9):093508, (2017). doi: 10:1063/1:4986219.

3. Granados, Victor H., Pinheiro, Mario J., and Sá, Paulo A., Study of the design and efficiency of single stage EHD thrusters at the sub-atmospheric pressure of 1.3 kPa. Physics of Plasmas, 24(12):123513, (2017). doi: 10:1063/1:5018424.

During the completion of the research, the author presented several communications, both oral and poster, to the following conferences on plasma physics:

1. EHD thruster discharge simulation on N_2-O_2 mixture at low pressure, XXXIII edition of the International Conference on Phenomena in Ionized Gases (ICPIG), Estoril, Portugal, July 2017.

2. Performance of an EHD thruster by the use of the two-term approximation Boltzmann equation and the Maxwell equation for the EEDF for air at low pressure, 2nd Doctoral Congress in Engineering (DCE), Porto University, Portugal, June 2017.

3. Performance optimization of an EHD thruster: the influence of secondary emission and the electrodes gap, 69th Annual Gaseous Electronics Conference (GEC), Ruhr-University Bochum, Germany, October 2016.

4. Estudo do desempenho de um dispositivo EHD para aplicações aerodinâmicas, 20^{a} Conferência Nacional de Física, Universidade de Minho, Braga, Portugal, Set. 2016.

5. Influence of temperature and pressure on a single-stage EHD thruster performance on nitrogen gas, 28th Symposium on Plasma Physics and Technology, Prague, Czech Republic, June 18-21, 2016.

6. Simulation of an EHD thruster in pure argon at low pressure, 32nd ICPIG conference, Iasi, Romania, July 26-31, 2015.

7. Modelling and Optimization of an Electrohydrodynamic (EHD) Thruster, 42nd European Physical Society Conference on Plasma Physics, Lisbon, Portugal, June 22-26, 2015.

8. Simulation of a DC-discharge ionic wind generator in low pressure nitrogen, Doctoral Congress in Engineering (DCE), Physics Engineering Symposium, Porto University, Porto, Portugal, Vol 1, June 2015.

1.5 Project Structure

Regarding the present study, a mathematical description for rockets motion is presented on Chapter 2. Definition of the main variables and parameters of rocket propulsion through the case of chemical rockets is detailed in order to set up a point of comparison for the newer technologies. A review and classification of several electric propulsion systems is also discussed as well as how the advantages and disadvantages of each technology -according to their performance- evidence their possible use on different scenarios.

Chapter 3 presents a detailed explanation of electrodynamic thruster models, starting with a one-dimensional ideal model and continuing with a two-dimensional model including the equations, gas characteristics, cathode geometries and boundary conditions considered in the models investigated on the present work.

Chapter 4 depicts the resulting characteristics of EHD thruster simulations using three working gases: i) argon (a noble gas), nitrogen (main component of air), and oxygen (an electronegative gas); and three cathode geometries: conical, cylindrical, and funnel-like. All cases are considered with a pressure of 0.5 Torr ($\approx$ 66.7 Pa) and a constant gas temperature of 300 K. The spatial distributions of electric potential and fluid velocity magnitude are studied along the radial, axial and total components of the gas velocities at the thruster's exit plane. The transient characteristics of voltage between electrodes and secondary electron emission flux from the cathode are also considered to depict the time-dependency of the discharges and how they reach the desired steady-state. Thrust and thrust-to-power ratio are resulting parameters to consider in order to compare their performance among cases.

For Chapter 5 the pressure of all the working gases was increased twenty times until 10 Torr ($\approx$ 1.3 kPa), while maintaining most parameters at the same values and the results are compared with the lower pressure case. Also an exhaustive analysis of the electron and ion densities (Ar^+, Ar_2^+, N_2^+, O^+, O^-, O_2^+, and O_2^-) and space charge densities (nitrogen and oxygen gases) is presented in order to shed light into the constitution of the plasma between the electrodes of the thruster at the steady state of the discharge.

On Chapter 6 we may find the response of the EHD thruster model to a wide range of variations on the conditions that influence its performance in order to better understand their role in the discharge driving the plasma. The conditions explored are i) the gas pressure [0.5-100] Torr, ii) the gas temperature [190-400] K, iii) the ballast resistance [200-1000] MΩ, iv) the secondary electron emission coefficient, γ_i, [10^{-5}-10^{0}], and the gap between electrodes [0-10] cm.

Finally, conclusions concerning the development of electric propulsion technologies and future work paths are presented on Chapter 7.

Chapter 2

Principles of rocket propulsion

Even though the main contribution of the present work is focused on a specific type of plasma thruster, it becomes necessary to introduce to the reader certain concepts of propulsion in order to present a more complete picture of the subject. The latter is done by going through some basic principles of rocketry, its most relevant parameters and electric plasma-based propulsion systems known up to date.

2.1 General overview

According to Sutton (2000), rocket propulsion is defined as "the process of imparting a force to a flying vehicle, such as a missile or a spacecraft, by the momentum of ejected matter. This matter, called propellant, is stored in the vehicle and ejected at high velocity. In chemical rockets the propellants are chemical compounds that undergo a chemical combustion reaction, releasing the energy for thermodynamically accelerating and ejecting the gaseous reaction products at high velocities. Chemical rocket propulsion is thus differentiated from other types of rocket propulsion, which use nuclear, solar, or electrical energy as their power source and which may use mechanisms other than the adiabatic expansion of a gas for achieving a high ejection velocity."

A simple generalized rocket diagram is shown on Figure 2.1

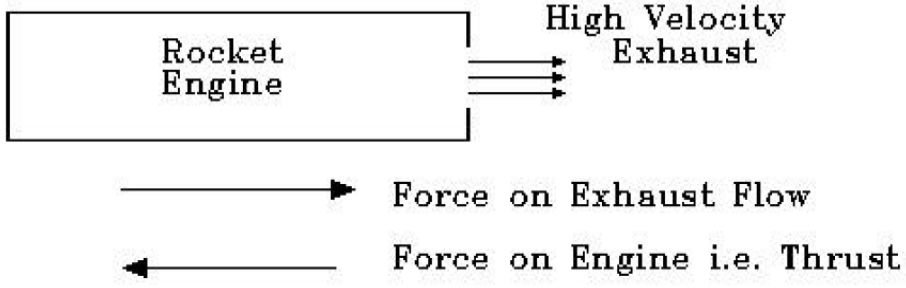

Figure 2.1: Basic rocket diagram (taken from Wootton (1997))

Since a rocket does not use any of the constituent parts of the surrounding atmosphere (e.g. jets), then it means it can operate both inside the atmosphere and outside of it, which makes it perfect for space propulsion. On a chemical rocket, a fuel and a oxidizer are often supplied in the combustion chamber. The reaction between this two parts produce a high pressure and a high temperature in the combustion chamber and as a consequence of such reaction the resultant gaseous products are expelled through the rocket nozzle (since the pressure outside is lower than on the chamber). This movement of gases produce a high velocity matter flux, giving thrust to the rocket on the opposite direction (see Figure 2.2).

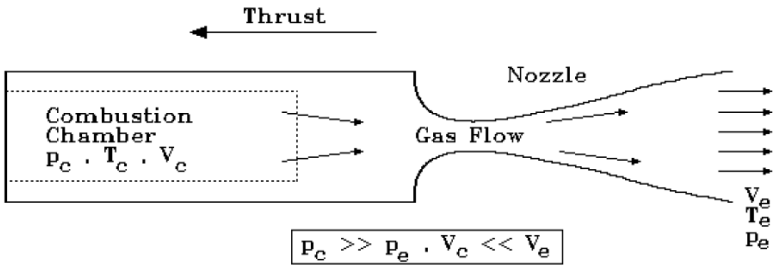

Figure 2.2: Basic chemical rocket diagram (taken from Wootton (1997))

As Figure 2.2 indicates, the pressure inside the chamber (p_c) is greater than the pressure outside the rocket (p_e). Besides, due to the expansion of the gases in the nozzle the exhaust gas attains a higher velocity (V_e) than inside the chamber (V_c) and thus the momentum gained of the expelled mass.

Now, let us consider a rocket, traveling at a velocity of magnitude V in a given direction at $t = 0$. The rocket possess a total mass of $m + \Delta m$, considering a differential of mass Δm as fuel. Now let us consider the same rocket at a later time $t = \Delta t$, at this moment the rocket continues in the same direction but its velocity magnitude has increased by ΔV and the fuel Δm has been expelled in the opposite direction of the rocket's movement with a velocity of magnitude V_e. Both velocities V and V_e are with respect to an observer located in an inertial frame of reference outside the rocket and fuel itself.

We may relate the velocity of the exhaust propellant from the observer frame of reference, V_e, with the velocity of the exhaust in the rocket frame of reference, v_e, by simple vector addition, which taking into account the dirrection can be converted into the scalar equation:

$$V_e = V - v_e \tag{2.1}$$

Now applying Newton's second law of motion to the whole system, i.e. rocket and exhaust, and considering the external forces that may apply to the system, F_i, we have that:

$$\sum F_i = \lim_{\Delta t \to 0} \frac{\Delta P}{\Delta t} \tag{2.2}$$

where ΔP is the change of linear momentum of the system. When $t = 0$ we consider the linear momentum to be P_1 as:

$$P_1 = (m + \Delta m)V \tag{2.3}$$

since all the system is moving initially with the velocity of magnitude V. At $t = \Delta t$ we have:

$$P_2 = m(V + \Delta V) + \Delta m V_e \tag{2.4}$$

since the rocket (m) is traveling at an increased velocity of magnitude $V + \Delta V$ and the exhaust (Δm) is moving at the exhaust velocity magnitude V_e.

We may now describe the change in linear momentum using the rocket frame of reference as:

$$\Delta P = m\Delta V - \Delta m v_e \tag{2.5}$$

Also we should consider that $dm = -\Delta m$ since the ejection of positive Δm implies a decrease in rocket mass, then we re-write Netwon's second law of motion as

$$\sum F_i = m\frac{dV}{dt} + v_e\frac{dm}{dt} \tag{2.6}$$

If we consider that the system is under no external forces ($\sum F_i = 0$). Then we have

$$m\frac{dV}{dt} = -v_e\frac{dm}{dt} \tag{2.7}$$

We will assume an exhaust velocity independent of time (constant but not necessarily uniform), then we may integrate the previous expression and consider an initial total mass including the propellant of m_0 and a final total mass (the rocket and the remaining unused fuel) of m_1. We now have Tsiolkovsky's rocket equation:

$$\Delta V = v_e \ln\left(\frac{m_0}{m_1}\right) \tag{2.8}$$

The ΔV in the previous equation represents the increase in velocity that the rocket will gain when expelling its fuel at velocity v_e relative to the rocket and having "lost" such fuel from an initial total mass m_0 to a certain total mass m_1.

The real "lost" or burnt fuel is the difference $m_0 - m_1$, which may be described as

$$m_0 - m_1 = m_1\left(e^{\Delta V/v_e} - 1\right) \tag{2.9}$$

2.2 Rockets Main Parameters

As described on Charles (2009), there are some important parameters to define in order to understand the basics of rocket propulsion. For the purpose of this study, only parameters which are comparable in between rockets -regardless of their kind- are taken into consideration. The latter due to the huge amount of performance parameters that belong to each particular type of propulsion media.

The **thrust** (T) represents the force applied to the spacecraft by the resultant effect of ejecting fuel on the opposite direction. Thrust is given by the time rate of change of the propellant's momentum:

$$T = \frac{d(m_p v_e)}{dt} = v_e \frac{d(m_p)}{dt} \tag{2.10}$$

Where m_p is the propellant mass and v_e is the propellant exhaust velocity (assumed constant). T is expressed in N, v_e in m.s^{-1} and $d(m_p)/dt$ in kg.s^{-1}.

According to Charles (2009):

> "The **specific impulse** (I_{sp}), or ratio between the thrust and the rate of propellant consumption by the sea-level weight, can be expressed as the exhaust velocity divided by the gravitational acceleration, g (9.81 m.s^{-2}).
>
> $$I_{sp} = \frac{T}{\frac{dm_p}{dt} g} = \frac{v_e}{g} \tag{2.11}$$
>
> The I_{sp} is expressed in units of seconds and can be viewed as a measure of the propellant fuel consumption rate and the magnitude of the exhaust velocity. High exhaust velocities v_e or high I_{sp} allows the maximization of missions payload mass and turns electric propulsion more attractive".

Electric propulsion bases its premise on maximizing the exhaust velocity while reducing the rate of propellant consumption.

On chemical rockets, the efficiencies are not commonly used directly in designing rocket units, although they allow an understanding of the energy balance of a rocket system (see Sutton (2000)). Their definitions are arbitrary, depending on the losses considered, and what it is defined as a consistent set of efficiencies. The energy balance diagram for a chemical rocket on Figure 2.3 shows the typical losses found on such systems.

The **propellant flow rate** represents the loss of mass by the rocket per time unit (kg/s) since the rocket is a variable-mass object. It indicates how fast the rocket is burning its fuel during its operation.

The **mass ratio** is the ratio of the total mass of the vehicle to its empty mass as represented by m_0/m_1 in Equation 2.8. The total mass must consider all units such as the chamber, nozzle, controls, fuel, the payload, etc. The empty mass must consider the vehicle after all its fuel has been expelled (or before filling their tanks).

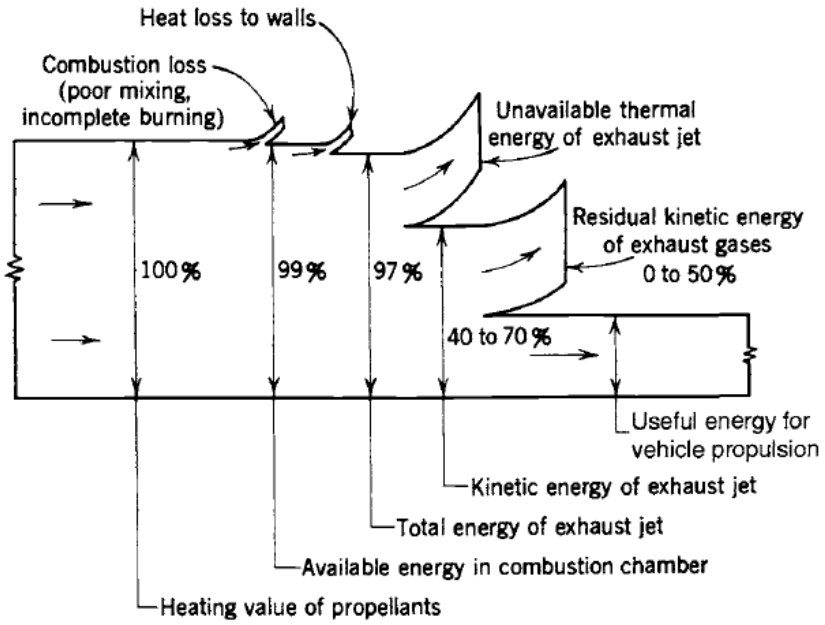

Figure 2.3: Typical energy balance diagram for a chemical rocket (taken from Sutton (2000))

For example, the V2 rocket, developed during the World War II, had a total mass of 12900 kg and an unfueled mass of 4000 kg which makes its mass ratio of 3.225 (see Wu (2014)).

Another efficiency factor to consider in spacecrafts is the **thrust-to-weight ratio** ($\frac{T}{W}$ or TWR), which defines the moving force produced by the spacecraft in relation with its own weight and it is defined as follows:

$$TWR = \frac{T}{W} = \frac{Thrust}{Weight} = \frac{Thrust}{mg} \tag{2.12}$$

Where m is the spacecraft's mass and g is the gravitational acceleration. In the case of a rocket during liftoff, the produced thrust is in opposition to its weight which makes $Thrust = ma$; then the TWR redefines as:

$$TWR = \frac{ma}{mg} = \frac{a}{g} \tag{2.13}$$

When the condition $TWR > 1$ holds, then it means the rocket produces an acceleration higher than the gravitational acceleration, implying the rocket is on liftoff. According to McCormack (2004): "Vertical takeoff from the Earth requires a thrust force that exceeds the weight of the complete missile by some 30 to 50 percent (a thrust-to-weight ratio of 1.3 to 1.5)".

A useful measurement of performance of a rocket, aircraft, general vehicles, and even power sources is the **power-to-mass ratio** (also called specific power), which indicates the amount of power produced by a body per unit mass. The power-to-mass ratio represents how efficiently a source or vehicle can produce output power in relation to its mass. It is particularly convenient to compare different means of transportation, specially when the mass of the vehicle represents a key

constrain. For example, a motorcycle presents a higher power-to-mass ratio than a conventional car since the power output might be similar in operational conditions (same speed) but the motorcycle has a significantly lower mass than the car, which makes it a more efficient mean of transportation.

For electric propulsion systems, the **thrust-to-power ratio** (T/P ratio) is another efficiency indicator since it compares the amount of thrust performed by a rocket from a given amount of electric power output spent. T/P ratio is particularly useful on the present research since we may determine how power-efficient the electric propulsion system is according to its propellant, geometry and other parameters with the same operating power.

Since there are many kinds of transportation systems, both for air and space, and there is no particular mean that can be considered as the "perfect machine", then we need to consider the pros and cons of each technology and its applicability grounds. Electric propulsion is one technology that promises great advances in the field of deep-space exploration, particularly the plasma thrusters, which will be detailed on the following section.

2.3 Electric Propulsion

Space exploration, satellites positioning, probes operation and other similar space-related missions have an increasing interest on lowering the fuel consumption of their spacecrafts and conventional chemical propulsion has proven cost-inefficient for such task. Electric propulsion presents an alternative solution to the transport of cargo on space due to its high specific-impulse nature. For the purposes of the present study, plasma thrusters will be studied as they depict one of the most promising versions of electric propulsion for space travel nowadays.

2.3.1 Plasma Basics For Propulsion

As seen in the previous chapter, the thrust in a rocket depends on both the velocity and the mass flow rate of the exhaust (Equation 2.10). Chemical rockets obtain thrust by expelling the propellant in gaseous form at a high mass flow rate (and a exhaust velocity of the range of [2-5] km/s) making them devices of considerable mass; an undesirable feature for deep space exploration. On the other hand, plasma rockets exploit the principle of increasing the exhaust velocity and reducing significantly the mass flow rate. The latter is achieved by using propellant in the form of plasma instead of gas since plasma is a more energetic state and thus is able to reach higher exhaust velocities (range of [5-50] km/s). The total thrust produced by a plasma rocket is usually on the order of the μN and mN depending of its kind, although there are a few plasma rockets on development which perform on the range of [1-5] N (see Choueiri (2009) and Goebel and Katz (2008)).

According to Charles (2009): "An electric thruster typically comprises three components or regions as shown in Figure 2.4: the plasma coupling (cavity) region, the ion extraction/acceleration region and the ion beam neutralization/detachment region (or plasma plume). The latter two are often defined as the thruster exhaust. The main distinction between a gridded ion thruster and a

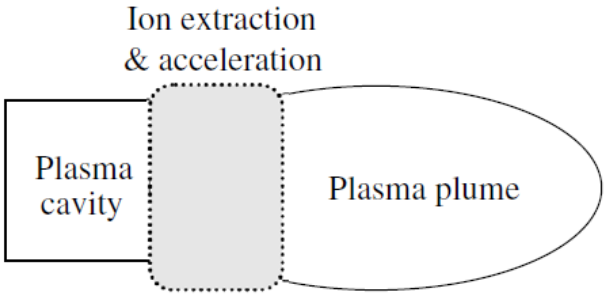

Figure 2.4: Schematic showing the three components of an electric thruster (plume neutralizer not shown). (taken from Charles (2009))

plasma thruster is the use, or not, of electrically biased multi-aperture grids for the extraction and acceleration of the ion beam which then has to be neutralized".

2.3.2 Plasma Thrusters Categorization

Different categories might rise to classify the various plasma thrusters, depending on the desired scope. Table 2.1 presents a common categorization separating the thrusters for ionization and acceleration methods into three major groups. Some authors do not necessarily agree with the following classification of these technologies.

Table 2.1: Categories of Plasma Propulsion Technologies

Electrothermal propulsion	**Electrostatic propulsion**	**Electromagnetic propulsion**
Resistojets	Ion thrusters	MPD[3] Thrusters
Arcjets	FEEP[1] thrusters	Hall-effect Thrusters
Electrothermal hydrazine	Microwave or Radio-frequency ion	VASIMR[4]
Microwave electrothermal	Plasma separator ion	Helicon
Pulsed electrothermal	EHD[2] thrusters	Inductive pulse

While some thrusters employ only electric fields as means of ionization and acceleration (as it is the case of the present work), other use magnetic fields or a combination of both in order to exert force to the propellants via the Lorentz force. Some authors differ in where to allocate certain thrusters in the categories of Table 2.1, considering them electrostatic or electromagnetic propulsion, mostly due to the employment of their magnetic fields, whether it is for ionization, acceleration or detachment of the gases inside their chambers.

Electrothermal propulsion depends on thermal heating of the propellant in order to increase its energy and thus increasing the exhaust velocity. The physical phenomenon of the propellant is highly thermodynamical and has very few relation with the electric or magnetic fields, both

[1] FEEP: Field Emission Electric Propulsion
[2] EHD: Electrohydrodynamic
[3] MPD: Magnetoplasmadynamic
[4] VASIMR: Variable Specific Impulse Magnetoplasma Rocket

induced or applied. As depicted in Figure 2.5, a resistojet uses ohmic heating on the propellant in a heat exchange chamber and a Arcjet relies on DC current heating, AC current heating, and RF heating (more on the topic can be found on Jordan (2000)).

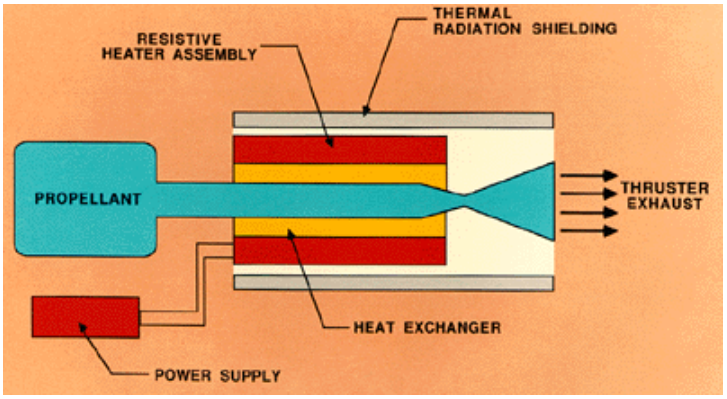

Figure 2.5: Basic elements of a resistojet rocket (taken from Jordan (2000)).

Electrostatic propulsion employs high-voltage electrostatic fields in order to accelerate, via electrostatic Lorentz force, the ions of a plasma, obtaining high exhaust velocities. The acceleration of the ions is typically guided by a grid with two or more electrodes. The acceleration grid is considered the *ion extraction and acceleration region* according to Figure 2.4. Due to the fact that an acceleration grid extracts the ions of the plasma towards the exhaust, a neutralizing media is used in order to electrically balance the total fluid, otherwise the accumulation of opposite charges on the exhaust and the cavity would rise undesired electrostatic forces opposing thrust production (see Figure 2.6). The neutralizing electron gun is on its own a key device that characterize and influences the performance of the ion thrusters most notably in terms of maximum achievable bias voltage. Grid erosion is a considerable constraint in the lifetime and performance of electrostatic thrusters since the particles on the propellant constantly bombard the grid on its way to the exhaust.

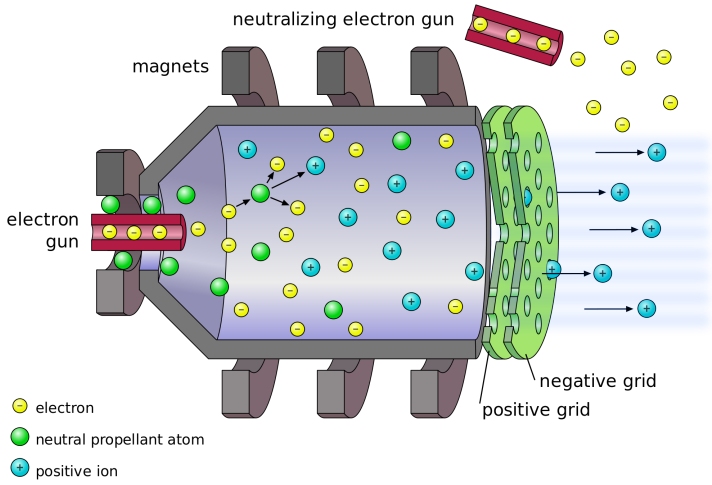

Figure 2.6: Ion Thruster diagram (taken from Anthony (2012)).

The most remarkable mission of an ion thruster is the Deep Space-1 spacecraft, launched in 1998 by NASA as their first rocket to ever use electrostatic propulsion instead of conventional chemical powered rockets.

The main electrostatic thrusters are detailed on Figure 2.7, where we may notice the variety of layouts in the components, differing from their ionization method, the disposition of the electrodes and the presence (or lack of) acceleration grids (the authors consider Hall thrusters in the electrostatic category since the acceleration is driven by the electric field between the internal anode and external cathode/neutralizer).

The FEEP thruster differentiates from other types because they employ a liquid metal as propellant instead of a gas. It also presents a strong electric field in the tip of the emitter -by applying a high voltage between the emitter and the extractor- in order to cause a jet of charged particles to rush towards the extractor which then turns into gaseous phase by electrospray ionization.

The DC electron bombardment ion thruster possesses a hollow cathode that injects electrons, along with a precursor gas, into the chamber as the main ionization mechanism and the walls of the same chamber function as the anode. It also uses acceleration grids and a neutralizer as other thrusters in the same category (see Byers (1969); Wirz et al. (2001) for more on the development and testing of these devices).

The RF ion thrusters typically employ a radio-frequency antenna in order to insert the necessary energy into the feed of gas in the chamber to achieve ionization. On the other hand, microwave ion thrusters use electromagnetic waves to insert the energy into the gas via electron cyclotron resonance (ECR) but they also add magnetic fields to form the ECR layer that generates the high-energy electrons for ionization of the neutrals, confining and stabilization of the plasma inside the chamber (see Miyoshi et al. (1991, 2007)).

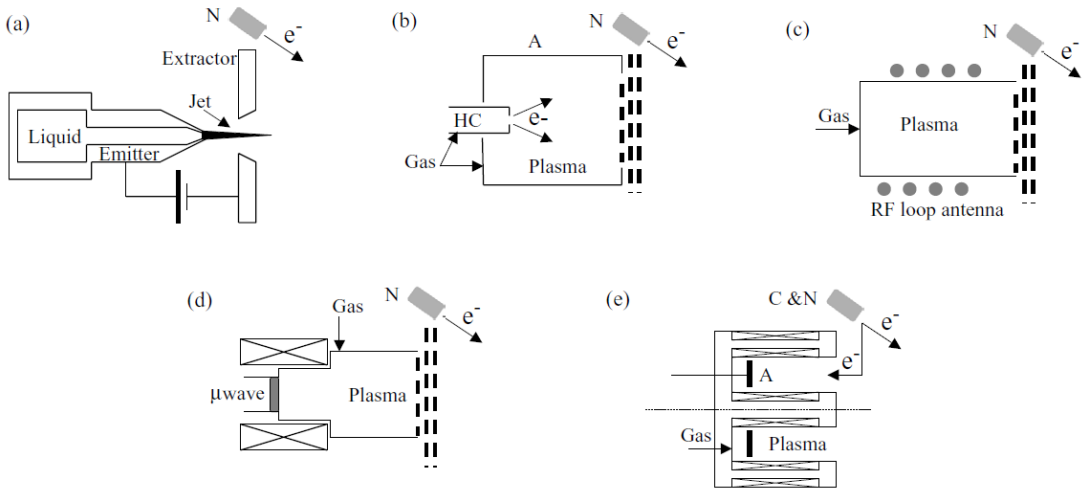

Figure 2.7: Schematic of main electrostatic thrusters: (a) FEEP thruster, (b) DC electron bombardment ion thruster, (c) RF ion thruster, (d) Microwave ion thruster and (e) Hall thruster; A=anode, C=cathode, HC=hollow cathode, N=neutralizer (taken from Charles (2009)).

The electrostatic thrusters commonly called “lifters” or “ionocrafts” (Figure 2.8), formally known as electrohydrodynamic (EHD) thrusters differ from the others of its kind because they use the surrounding air for creating thrust, instead of being fed with propellant gas. They also contain no moving parts, an ideal feature for pumps and flow control. They could be mainly considered for aeronautical applications and have awaken a new interest for possible applications on drones due to its high energy efficiency (see Wilson et al. (2009); Masuyama and Barret (2013)).

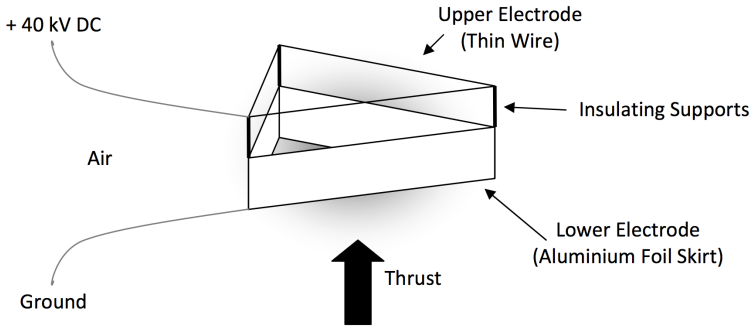

Figure 2.8: Lifter diagram, ionic wind flows from the upper electrode to the lower electrode, thus creating thrust (taken from Chu (2013)).

The ionization of the gas occurs near the electrode with lower radius of curvature due to the corona effect while the electric field formed between electrodes drives the ionized species towards the second electrode, which collide with neutrals transferring momentum and thus creating a flow between electrodes.

The electrohydrodynamic (EHD) thrusters will have special attention on the present work because they play an important role in the development of future investigations.

Electromagnetic propulsion differs from the previous ones from a key factor, it uses magnetic fields in order to better confine and deflect the plasma from its production until its detachment on the plume region. The plasma densities are typically higher due to a better confinement and the interaction of the plasma with the internal walls is significantly reduced. The acceleration method is due to interaction with the electromagnetic field and no grids are present.

There are different methods of operation of electromagnetic thrusters, most of them use the total Lorentz force (due to both Electric and Magnetic fields) for acceleration of the plasma into the exhaust. Magnetoplasmadynamic (MPD) thrusters, as seen on Figure 2.9, are similar to arcjets but improved in the sense that the first include magnetic fields for guiding and compressing the plasma and the plasma is generated by a high current, which includes the Joule heating for ionization of the propellant gas. MPD thrusters rely on the $\mathbf{J} \times \mathbf{B}$ force in order to accelerate and detach the plasma from the chamber (see Arefiev and Breizman (2005) and Choueiri (2009)).

There are thrusters which apply several mixed techniques to introduce energy into the plasma, an example of such is the VASIMR that uses Helicon RF antennas for ionization and a second stage with ion cyclotron heating (ICH) coupler for further energizing the plasma before the exhaust stage (for more on the subject see Molina-Cabrera and Tolyarenko (2011), Bering et al. (2008), Carter et al. (2002), Chang-Diaz et al. (1999) and Squire et al. (2011)).

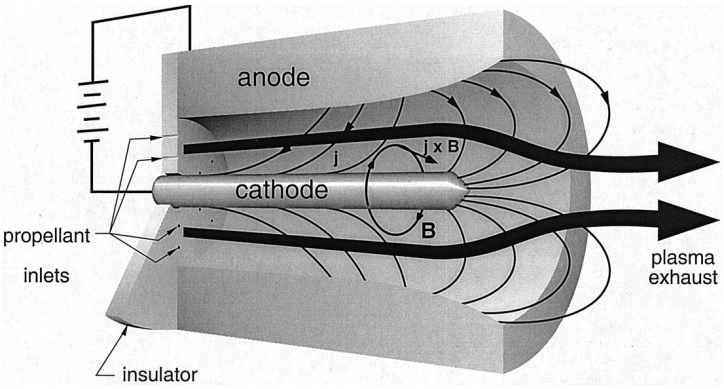

Figure 2.9: Cross section of a MPD thruster showing the $\mathbf{J} \times \mathbf{B}$ force (taken from Jahn and Choueiri (2002)).

The Hall thrusters, such as the one portrayed in Figure 2.10, are typically cylindrical devices similar to MPD thrusters but with an external cathode/neutralizer and an internal anode in order to create an axial electric field, while a radial magnetic field is set between the inner and outer poles. The electrons flowing between electrodes interact with the magnetic field to produce ionization inside the chamber. The $\mathbf{E} \times \mathbf{B}$ drift is in the azimuthal direction around the chamber channel maintaining the ionization region near the chamber exit. The ion gyro-radius is large enough so that the ions hit the chamber walls while the electrons are trapped (smaller gyro-radius). The total current density together with the magnetic field produce the $\mathbf{J} \times \mathbf{B}$ Lorentz force which is the main mechanism that produces the thrust, where $\mathbf{J} = -en_e\mathbf{v}_e$ is the Hall current density. Erosion from the chamber walls is an important restriction in the lifetime of the thruster since ions are constantly impinging its surface. The precursor gas is injected through the anode.

The working gases used to produce the plasma on the chamber of the thrusters varies depending on the thruster ionization mechanism and over all performance, but noble gases are the most commonly employed due to their low reactivity (safety purposes) and inert nature, which avoids oxidation on the walls (typically helium, argon, krypton and xenon). Among the non-radioactive noble gases, xenon has the highest energy level of electrons which makes it relatively easy to ionize since its outermost shell electrons are available for extraction and since it possesses the highest atomic weight among the noble gases mentioned before, it could potentially produce higher thrust. Argon is the least expensive noble gas available in the market so it is advantageous for industrial applications, when adequate. Curran et al. (2000) report the effect of adding noble gases to a H^- production in a hydrogen plasma.

There are alternatives for the use of precursor gases to produce plasma besides noble gases. Molecular nitrogen (N_2) and oxygen (O_2) are the most abundant gases on the earth's atmosphere so they are clear candidates for their study, specially in EHD thrusters and flow control applications. According to Adamovich et al. (2017): "Another critical aspect of EP (electric propulsion) is identifying alternative propellants to xenon to reduce the overall cost of EP while prolonging the mission duration".

Many variables come into play when designing a rocket, making it a difficult task to assess

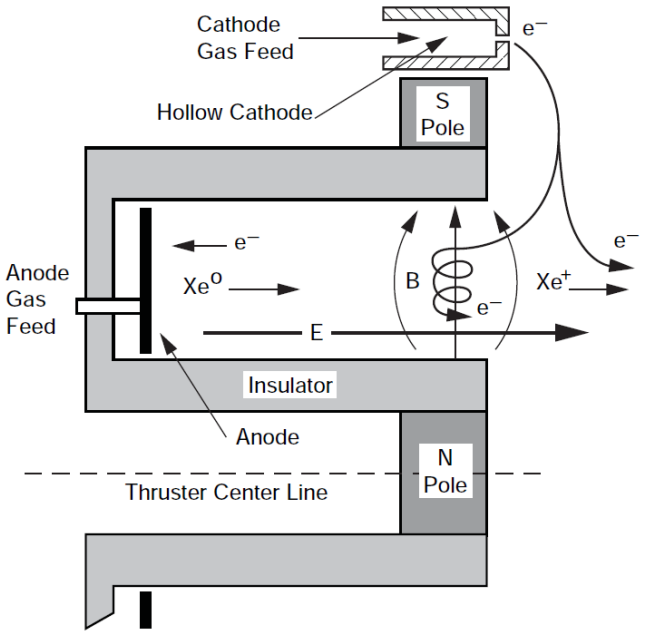

Figure 2.10: Cross section of a Hall thruster showing the crossed electric and magnetic fields with the charged particles paths (taken from Goebel and Katz (2008)).

the best one in an absolute. Different characteristics are desirable from one mission to the next one and there lies the main reason for the proliferation of different plasma thrusters. A summarize of some plasma thrusters that have operated during flight and their basic performance parameters can be found on Table 2.2. Notice the typically high energy conversion efficiency as well as the high range of the specific impulses and typical thrust from all the listed plasma thrusters. The magnitude called "Electric Power/Thrust" is defined as the inverse of the trust-to-power (T/P) ratio in this document.

There are several challenges to overcome on plasma propulsion in order to fully profit from its advantages such as: complexity of operation, energy hunger, erosion of materials after long periods of operation and more. The human exploration of outer space needs the development of suitable technologies that will allow us to travel faster, further and more efficiently than ever before. There is a big gap in our space-traveling capabilities as a human race and it is our mission as scientists and engineers to push the boundaries of human knowledge in order to fill that gap. For a more detailed scope on electric propulsion, its categorization, operating principles and their history the reader may refer to Charles (2009), Choueiri (2004), Jordan (2000), Martínez-Sánchez and Pollard (1998) and Molina-Cabrera et al. (2011).

The following chapter will focus on how to model electrohydrodynamic thrusters, the effect that drives them, the kinetic model for the considered working gases and it will introduce the proposed geometries of the present study.

Table 2.2: Performance parameters for several plasma thrusters that have flown (taken from Jordan (2000)).

Propulsion Type	**Specific Impulse (s)**	**Thrust/ Weight (N/kg/g)**	**Specific Power (kW/kg)**	**Electric Power/ Thrust (kW/N)**	**Energy Conversion Efficiency**	**Propellant Utilization Efficiency**	**Typical Thrust (mN)**	**Impulse Bit (mN-s)**	**Total Impulse (N-s)**
Electrothermal Arcjet	480 - 810	0.003 - 0.005	0.25 - 0.5	6 - 15	91 - 95 %	27 - 37 %	100 - 2000		12,000
Augmented Hydrazine	294-304	0.018 - 0.036	0.5	1.5 - 3			180 - 300		
Resistojet	280 - 305	0.02 - 0.05	0.4 - 0.8	1.3 - 2	60 %	35 %	180 - 500		300,000
Ion Bombardment	2500 - 3310	0.0001 - 0.0006	0.03 - 0.12	22 - 36	87 - 91 %	46 - 66 %	10 - 160		$>3x10^6$
Radiofrequency Ion	3000 - 3150	0.00017	0.07	39	64 %	71 - 80 %	15		
Contact Ion									
Field emission Ion	4,000 - 11,000			33 - 60			.001 - 1000	$1x10^{-6}$	
MPD	600	0.00005	0.01	10 - 19		15 %	23	<500<	> 1,000
Pulsed Plasma	830 - 1200	0.000004	0.003 - 0.005	83 - 100	80 %	7 - 9 %	0.3 - 0.75		15,000 - 20,000
Hall Effect	950 - 1950	0.0006 - 0.003	0.1 - 0.45	16 - 19	91 - 93 %	42 - 67 %	11 - 512		$2.3x10^6$

Chapter 3

Electrohydrodynamic modeling

3.1 Introduction

Electrohydrodynamics is the study of the flow of an electrically charged fluid under the action of and electric field, formally introduced by Hauksbee (1709) when he noticed a smooth air blowing in the vicinity of a electrically charged tube. Chattock (1899) investigated electrodynamics as a source of pressure difference and measured the ratio of velocity of the negative ions relative to the positive ions in a pin-to-plate configuration.

The first works on electrohydrodynamic thrusters can be followed to Thomas Townsend Brown in the beginning of 1920's. Brown proposed a series of devices that would produce force using electric fields as seen on the GB patent GB300311 (See Townsend Brown (1928)).

According to Masuyama (2012): "The discovery of the force, then called Biefeld-Brown Effect, was made during experimentation on Coolidge tubes. The mechanism responsible for the force was not well understood, as can be seen in Brown's patent referencing a coupling of electromagnetism and gravity."

Seversky (1964) patented the first EHD based propulsion system. On the patent it reads: "This invention relates to improved heavier-than-air aircraft, and more specifically to structures which are capable of either hovering or moving in any direction at high altitudes by means of ionic discharge". The patent suggests the use of several gridded electrodes covering a rather large area in order to increase the electric wind volume.

During the 1960's Robinson (1961, 1962) and Christenson and Moller (1967) conducted theoretical and experimental research on the EHD thrusters but reported very low kinetic energy conversion efficiency (in the range of 1%). Later, Bondar and Bastien (1986) demonstrated that increasing the fluid velocity leads to a higher energy conversion efficiency.

Singhal and Garimella (2005), concluded that it is possible to increase in conversion efficiency by increasing the incoming velocity into an EHD-pump by simulation techniques. In parallel, Rickard et al. (2006) demonstrated that the ionic wind velocity may be increased when more stages of electrodes in cascade are added to the configuration (they tested up to 7 stages in series).

Pekker and Young (2011) developed a simple one-dimensional model for an ideal EHD thruster providing an estimate for the net produced thrust and energy efficiency. It was shown that the performance of EHD thrusters drops very fast at high altitudes, which points to the decrease in atmospheric pressure as the main reason. Masuyama (2012) study a wire-to-cylinder thruster configuration and the performance of dual-stage three-electrode wire-to-rod-to-cylinder electrode geometries, demonstrating that in order to generate thrust between the intermediate and the collector electrodes it was needed a large voltage and that a reverse corona was formed at the intermediate cylinder electrode, which was counterproductive for the setting of a strong electric field.

On the last years the electrohydrodynamic (EHD) thrusters gained a new interest on the scientific community due to the fact that non-manned aircrafts are a reality for surveillance and military applications. Special interest has risen from the high electrical efficiencies on which this devices operate (See Chu (2013)).

Several application for the ionic wind have come to light on the last decade such as electronics cooling for microprocessors and dust pumps for exploration of the martian surface by rovers (Zhao et al. (2008)). Boundary layer enhancement, fluid pumping/control as well as heat transfer via forced convection are specific applications of EHD effects of current interest (Fylladitakis (2014)). Micro-thrusters for space explorations have been recently investigated with improving results over older configurations (see Blanco and Roy (2017)).

The main goal of the present work is to contribute to the advancement of the performance of EHD thrusters for aerospace missions, specifically in the geometry of the electrodes and its layout, the working gas and its efficiency for each electrode geometry considered. Numerical techniques and tools (Comsol.com (2016)) are used for the description and calculation of fluid and electrical parameters essential to the understanding of EHD thrusters along with the boundary conditions needed to solve the differential equations involved.

Initially, the one-dimensional model for the EHD thruster will be detailed in order to understand the notions of the thruster's behavior under the simplest configuration. Afterwards a more detailed model of a two-dimensional axysimmetrical EHD thruster is presented, including all the necessary equations to solve and geometry of the electrodes in order to simulate its behavior under steady-state operation.

3.2 Ideal model of one-dimensional EHD thrusters

Electrohydrodynamic (EHD) thrusters are devices that produce thrust from the movement of a fluid using an electric field. The ionization and acceleration of the gas is carried out by the electric field alone. Typically two electrodes are place at a certain distance and each of them present a significantly different curvature radius. The latter consists of an asymmetric capacitor in which the electric field is more intense on the surface of the electrode with the smaller curvature radius (typically positive electrode), favoring corona effect to appear (see Jewell-Larsen et al. (2008); Masuyama (2012)).

The corona effect takes over the ionization process of the surrounding gas. At this point, the ionized particles are submitted to the acceleration of the electric field between electrodes. The accelerating ions -on their way to the opposite electrode (usually the grounded electrode)- collide with neutral gas particles, transferring to them momentum, thus creating a stream of gas between electrodes as seen on Figure 3.1. The stream of ionized gas is usually called ionic wind and it is the responsible for the generation of thrust (see Ieta and Ellis (2013); Zhao et al. (2008)).

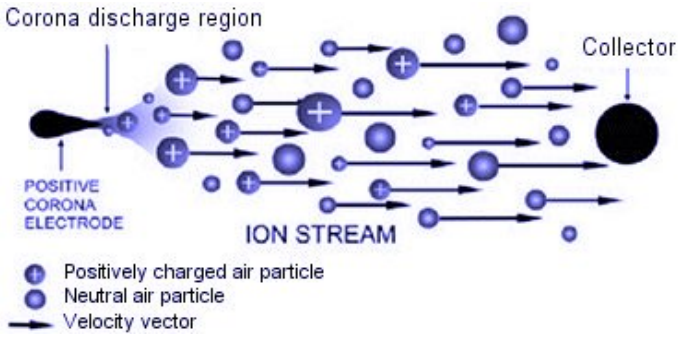

Figure 3.1: Ion stream between two electrodes when DC high-voltage is applied (taken from Jewell-Larsen et al. (2008)).

The corona effect or corona discharge is the phenomenon that EHD thrusters use for ionization of the gas. It is a nonuniform discharge that produces a non-equilibrium low-ionized plasma at atmospheric pressure. More on DC plasma discharges, their principles, mechanisms that affect them and their behavior using different gases may be found on Allis (1956); Boeuf (1988); Raizer (1991); Lisovskiy et al. (2000); Lieberman and Lichtenberg (2005); Staack et al. (2008); Gudmundsson and Hecimovic (2017).

On EHD thrusters the electrodes are hold at a certain voltage so the electric field's strength is higher at the electrode with a smaller curvature radius (usually called emitter). The air surrounding the small curvature radius electrode gets ionized and the corona forms in its proximity (more details on Masuyama (2012)).

Peek's empirical formula (Equation 3.1) estimates the critical electric field strength needed to form the corona around the emitter electrode for the case of two parallel wires:

$$E_{cr} = 30\delta\left(1+\frac{0.301}{\sqrt{\delta r}}\right) \tag{3.1}$$

Where $\delta = \frac{3.92p}{T}$, p is pressure in cm Hg, T is temperature in kelvin, r is the radius in cm, and E_{cr} is given in kV/cm. It gives an estimation of the typical values to consider in the EHD thruster when two parallel wires are present as electrodes or it can be considered as a rough approximation if the geometry of the electrodes differ.

Thrust is obtained by the force of the ionic wind, for the case of single-stage EHD thruster (as depicted in Figure 3.2) using the next one-dimensional equation as derived from Cooperman

(1960):

$$F = \frac{C'V(V - V_0)}{d} \tag{3.2}$$

Equation 3.2 depicts the production of thrust in terms of the voltage applied between the electrodes, the separation of the electrodes (d) and the modified Cooperman factor (C') for a wire parallel to a flat plate. It also shows that the thrust is directly proportional to the applied voltage between electrodes and inversely proportional to the gap between them.

The modified Cooperman factor is defined in terms of the Cooperman factor (C) as:

$$C' = \frac{Cd^2}{\mu_i} = \frac{2\mu_i \pi \varepsilon_0 L}{d^2 ln(\frac{f_{geo}}{r})} \frac{d^2}{\mu_i} = \frac{2\pi\varepsilon_0 L}{ln(\frac{f_{geo}}{r})} \tag{3.3}$$

where ε_0 is the vacuum permittivity[1], μ_i is the ion mobility, L is the plate length, r is the wire radius and f_{geo} is an empirical geometric factor.

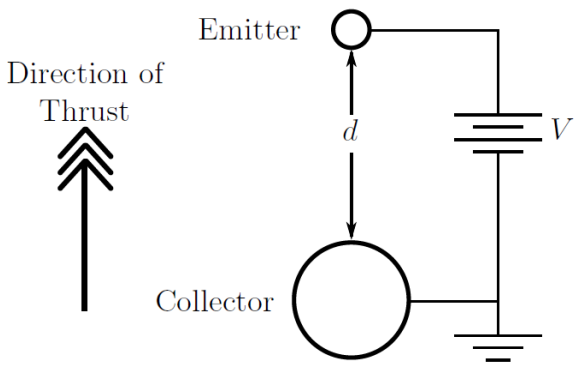

Figure 3.2: Single stage thruster geometry (taken from Masuyama (2012)).

Another analysis we may follow to describe the thrust is by seeing the electric field as uniform and given by:

$$E = \frac{V}{d} \tag{3.4}$$

then we define the current density in terms of the drift velocity ($v_D = \mu_i E$):

$$j = \rho_c v_D = \rho_c \mu_i E \tag{3.5}$$

The current between electrodes may be seen as the integral of the current density crossing an area A, perpendicular to the movement of ions,

$$I = \int_S j \cdot dA = \rho_c \mu_i E A \tag{3.6}$$

[1] $\varepsilon_0 = 8.854187817... \times 10^{-12}$ F.m^{-1}

then using Equations 3.6 and 3.4, the charge density is defined as:

$$\rho_c = \frac{Id}{\mu_i VA} \tag{3.7}$$

In order to find the electrostatic force we solve the volume integral of the space between electrodes ($dV = Adx$)

$$F = \int_V \rho_c E dV = \int_0^d \rho_c EA dx = \frac{Id}{\mu_i} \tag{3.8}$$

Then the electrohydrodynamic thrust is then defined in terms of the discharge current, the distance between electrodes and the ion mobility

$$F = \frac{Id}{\mu_i} \tag{3.9}$$

Since the power sources are usually driven by voltage, the current is a response from the impedance of the gas between electrodes. The current from a corona discharge is considered as:

$$I = CV(V - V_0) \tag{3.10}$$

then the thrust may be expressed in terms of voltage as initially consider in Equation 3.2 (seeing that $C = C'\mu_i/d^2$).

We may now wonder if the distance between electrodes impacts the thrust directly or inversely since the term appears in opposite positions in Equations 3.2 and 3.10. We must, then, consider that for changing distances between electrodes if the current or the voltage between electrodes maintains fixed or if it changes in proportion in order to find such influence.

Several advantages can be pointed out from the EHD thrusters such as: no moving parts, little maintenance, no propellant needed (aeronautical applications), high electrical efficiency (See Chu (2013)), no air pollution, among others.

As with any technology, EHD thrusters present challenges, for example the need for a light electrical source as well as the creation of sufficient amount of ionic wind (the bigger the volume of plasma, the higher the produced thrust).

The one-dimensional analysis consists in a first approach to understanding the corona effect and experimentally represent the behavior of the ionic wind but it fails in representing the interaction of the ionized species and the transfer of momentum with the neutrals. A more complete model for the EHD phenomena is needed to understand these discharges.

3.3 Self-consistent two-dimensional model of EHD thrusters

The electrohydrodynamic processes embody interlocking aspects of non-compressible gasdynamics (Navier-Stokes equation), ionized gas physics, self-consistent accelerating electric field ade-

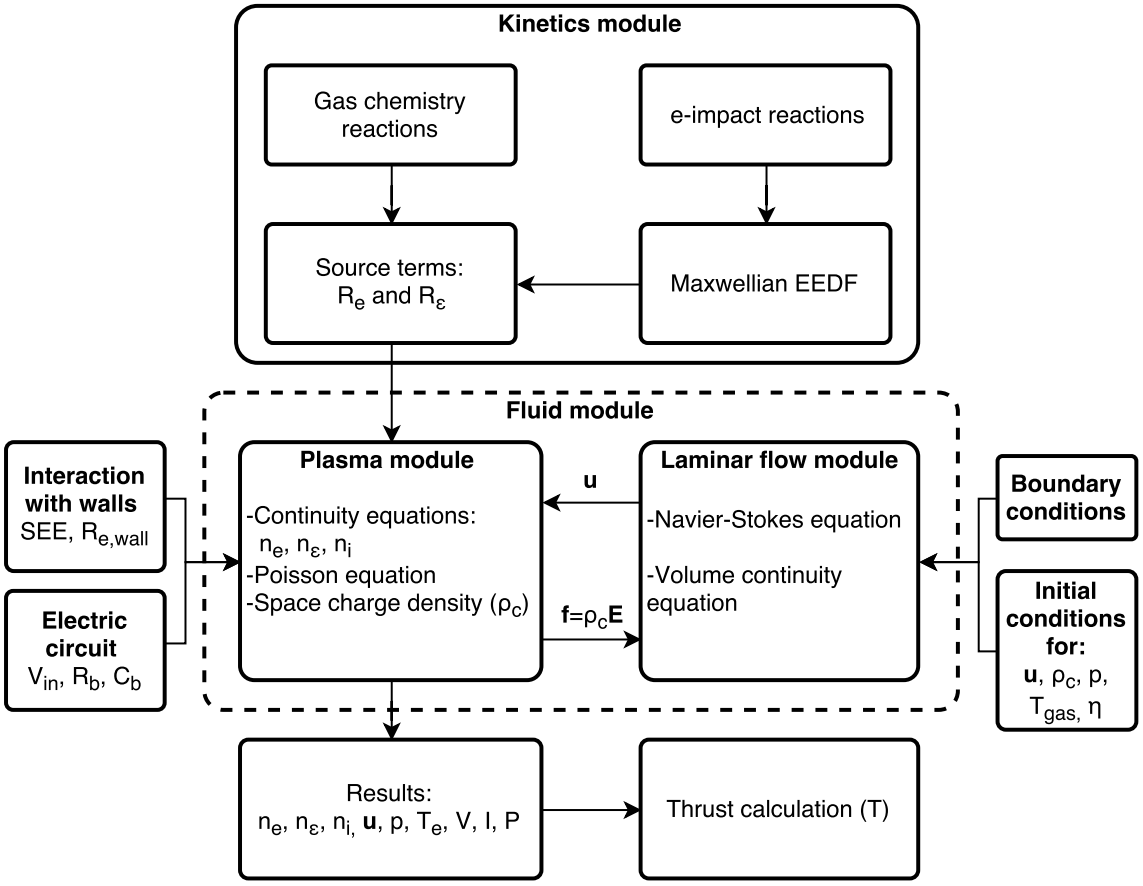

Figure 3.3: Pseudo-flow chart connecting the modules to solve the EHD thruster dynamics.

quately described by Poisson's equation, and migration of charged particles in an electric field in the drift-diffusion approximation.

Figure 3.3 shows a pseudo-flow chart of the complete model used which illustrates both the coupling between the various modules and the entrance parameters needed for the calculations. On the diagram, $\mathbf{u}$ represents the bulk fluid velocity vector, $\mathbf{f} = \rho_c \mathbf{E}$ is the electric field force density (where ρ_c is the space charge density and $\mathbf{E}$ is the electric field), R_e and R_ε are the electron and electron energy source terms, respectively, n_e, n_ε and n_i are the electron, electron energy and ion densities, respectively, n_g is the gas density, SEE represents the secondary electron emission from the cathode, $R_{e,wall}$ is the contribution to the electron source term due to electron interactions with the walls, V_{in}, R_b and C_b are the input voltage, ballast resistor and the blocking capacitor, T_e is the electron temperature, p represents the gas pressure, T_{gas} is the gas temperature, η is the gas dynamic viscosity, V, I and P stand for voltage, current and power, respectively, and finally, T represents the net thrust produced by the apparatus.

Three main modules are coupled in the model: i) a kinetic module, where a Maxwellian electron energy distribution function is called to produce electron transport coefficients and electron impact rate coefficients from a set of collisional cross-section data, used in kinetic rate balance equations of the various neutral and ionic heavy species active in the discharge region; ii) a plasma

model, for the accelerating electric field between electrodes and the migration of charged particles in an electric field, in the drift-diffusion approximation, and iii) a laminar flow module, which makes use of the Navier-Stokes equation to take into account the viscous non-compressible laminar gas dynamics considered. The plasma and laminar flow modules may be included in a more general module, called the fluid module, which allows to describe the transport of electrons and ions by the conventional equations related to the first moments of the Boltzmann equation: the continuity equation, the momentum equation (in the drift-diffusion approximation), and the energy equation for electrons. Each of these equations requires the input of transport coefficients, rate coefficients and electron rate coefficients as calculated in the kinetic module.

The Appendix A shows a flowchart of the sequence taken by the solver to find steady-state solutions to the EHD thruster simulations.

We should report that in our calculations, the gas density as well as the pressure and temperature of the neutral species is homogeneous. Therefore, we do not take into account the heating of the gas by the electric field because we are not considering the gas energy equation in our model. In the present model, the only gas parameter that changes with the electric field is the gas velocity.

The application of high voltage between two asymmetric electrodes produces a space-charge, consisting of ions and electrons in the discharge region. The plasma module uses the Poisson equation to compute the self-consistent electrostatic field; in that equation the space charge density term takes into account the plasma chemistry due to the inclusion of the densities of ions (n_i) and electrons (n_e). Owing to these results, it follows the necessity of a kinetic module, where for each of the three gases appointed, we consider a set of electron collisions cross-sections with the neutrals (elastic and inelastic, including ionization), plus volume and surface chemical reactions in order to model the behavior of the gas during the discharge.

3.3.1 Determination of the self-consistent electric field

The electrostatic field in the presence of a space-charge is computed using the Poisson equation:

$$\nabla^2 V = -\frac{\rho_c}{\varepsilon} \tag{3.11}$$

where ε is the plasma permittivity ($\varepsilon = \varepsilon_0\, \varepsilon_r$), $V(\mathbf{r})$ is the electric potential, and $\rho_c(\mathbf{r})$ is the space charge density computed taking into consideration the plasma chemistry by means of the equation:

$$\rho_c = e\left(\sum_{j=1}^{N} Z_j n_j - n_e\right) \tag{3.12}$$

where Z_j is the charge number of ions and n_j and n_e are the ions and electron densities, respectively. Then, the electric field is computed as:

$$\mathbf{E} = -\nabla V \tag{3.13}$$

3.3.2 Species governing equations

In order to emulate the behavior of the EHD fluid, we consider the continuity equation for the electron density, n_e:

$$\frac{\partial n_e}{\partial t} + \nabla \cdot \mathbf{\Gamma}_e = R_e - (\mathbf{u} \cdot \nabla) n_e \tag{3.14}$$

and the continuity equation for the electron energy density, n_ε:

$$\frac{\partial n_\varepsilon}{\partial t} + \nabla \cdot \mathbf{\Gamma}_\varepsilon + \mathbf{E} \cdot \mathbf{\Gamma}_e = R_\varepsilon - (\mathbf{u} \cdot \nabla) n_\varepsilon \tag{3.15}$$

In Equation 3.14, $\mathbf{\Gamma}_e$ is the electron flux in the drift-diffusion approximation:

$$\mathbf{\Gamma}_e = -(\boldsymbol{\mu}_e \cdot \mathbf{E}) n_e - \nabla(\mathbf{D}_e n_e) \tag{3.16}$$

and in Equation 3.15, $\mathbf{\Gamma}_\varepsilon$ is the electron energy flux:

$$\mathbf{\Gamma}_\varepsilon = -(\boldsymbol{\mu}_\varepsilon \cdot \mathbf{E}) n_\varepsilon - \nabla(\mathbf{D}_\varepsilon n_\varepsilon) \tag{3.17}$$

In the set of Equations (3.14) - (3.17), $\mathbf{\Gamma}_e$ is the electron flux, $\mathbf{\Gamma}_\varepsilon$ is the electron energy flux, $\mathbf{u}$ is the fluid velocity, $\mathbf{E}$ is the electric field, R_e is the electron density source, R_ε is the electron energy density source, $\mathbf{D}_e$ is the electron diffusivity tensor, $\mathbf{D}_\varepsilon$ is the electron energy diffusivity tensor, also $\boldsymbol{\mu}_e$ and $\boldsymbol{\mu}_\varepsilon$ represent the tensors for the electron and electron energy mobility, respectively.

On the left side of Equation 3.14, the first term stands for the temporal variation of the electron density while the second term denotes the divergence of the electron flux. On the right side the last term stands for the convection of electrons. On the right side of Equation 3.16, the first term represents the migration of electrons due to the applied electric field while the second represents the diffusion of electrons from high to low electron density regions.

Equation 3.15 is analog to Equation 3.14 but now in terms of electron energy density, with the inclusion of the third term on the left side of Equation 3.15 that represents the heating of the electrons due to the applied electric field. This term is a heat source or sink depending on whether the electrons are moving in the same or opposite direction of the external electric field.

Also, using Einstein's relation, $D = \frac{2}{3}\mu\bar{\varepsilon}$, (see Gogolides and Sawin (1992); Hagelaar and Pitchford (2005); Blickle et al. (2007)) for a Maxwellian electron energy distribution function (EEDF) we can derive, from the electron mobility ($\boldsymbol{\mu}_e$), the electron diffusivity ($\mathbf{D}_e$), energy diffusivity ($\mathbf{D}_\varepsilon$) and electron energy mobility ($\boldsymbol{\mu}_\varepsilon$):

$$\mathbf{D}_e = \boldsymbol{\mu}_e T_e \tag{3.18}$$

$$\mathbf{D}_\varepsilon = \boldsymbol{\mu}_\varepsilon T_e \tag{3.19}$$

$$\boldsymbol{\mu}_{\varepsilon} = \frac{5}{3}\boldsymbol{\mu}_{e} \tag{3.20}$$

where T_e is the electron temperature, defined as a function of the mean electron energy ($\bar{\varepsilon}$),

$$T_e = \frac{2}{3}\bar{\varepsilon} \tag{3.21}$$

The electron mobility tensor, $\boldsymbol{\mu}_e$, is simplified into a constant (μ_e) as we consider the mobility to be isotropic. Thus, the electron diffusivity, energy diffusivity and electron energy mobility are functions of the electron temperature.

The electron source term (R_e) is the sum of electron impact reaction rates of all the M considered reactions:

$$R_e = \sum_{j=1}^{M} x_j k_j N_0 n_e \tag{3.22}$$

where x_j is the mole fraction of the target species for the reaction j, k_j is the rate coefficient of reaction j and N_0 is the total neutral number density. The electron energy density source (R_ε) is the sum of electron impact reaction rates multiplied by the energy loss/gain corresponding to each of the P reactions taken into account:

$$R_\varepsilon = \sum_{j=1}^{P} x_j k_j N_0 n_e \Delta\varepsilon_j \tag{3.23}$$

where $\Delta\varepsilon_j$ is the energy loss/gain from reaction j. Since we consider several heavy species for each gas, we need the reaction rate coefficients of their collisional processes, which can be computed for electron collisions using a set of cross section data and assuming, for simplicity, a Maxwellian distribution function, $F_M(\varepsilon)$, from the usual equation:

$$k_j = \left(\frac{2e}{m_e}\right)^{1/2} \int_0^{\infty} \varepsilon \sigma_j(\varepsilon) F_M(\varepsilon) d\varepsilon \tag{3.24}$$

where ε is the electron energy (in eV) and $\sigma_j(\varepsilon)$ represents the elastic and inelastic (excitation and ionization) electron cross sections considered for each reaction.

The Maxwellian distribution function is defined as:

$$F_M(\varepsilon) = \bar{\varepsilon}^{-3/2} \beta_1 exp\left(-\frac{\varepsilon\beta_2}{\bar{\varepsilon}}\right) \tag{3.25}$$

where β_1 and β_2 are defined as:

$$\beta_1 = \Gamma(5/2)^{3/2}\Gamma(3/2)^{-5/2} \tag{3.26}$$

$$\beta_2 = \Gamma(5/2)\Gamma(3/2)^{-1} \tag{3.27}$$

and where the Γ represents the Gamma function, defined as

$$\Gamma(s) = \int_0^\infty t^{s-1} e^{-t} dt \tag{3.28}$$

The previous definition of a Maxwellian EEDF is the one defined by the Plasma Module user's guide from COMSOL Multiphysics® (see Comsol.com (2016)), which is the software used to implement the model of the EHD thruster.

The use of a Maxwellian distribution function can lead to an overestimation of ionization and the lowering of kinetic reaction coefficient with lower threshold. At any rate, it will give an overestimated value of the electronic temperature. Even if the latter is true we use the Maxwellian distribution function instead of a Boltzmann distribution function because in our study, we are basically interested in the main behavior of the plasma parameters on the thruster performance, and additionally we aim to speed up the numerical calculations. On section 3.3.7 we will discuss more on the topic of the EEDF chosen for the study.

3.3.3 Chemical kinetics

One of the key mechanisms which guarantees the plasma discharge stability is the secondary electron emission form the cathode. Ions are driven towards the cathode by the electric field and those that impact the cathode surface with sufficient energy will release secondary electrons into the bulk, which in turn will be driven by the strong electric field near the cathode, gaining enough energy to begin ionization, thus maintaining the discharge (see Austin and Starke (1902); Bruining (1954)).

In the present work we consider the interaction of ions with the cathode surface using the secondary electron emission coefficient, γ_i, and specifying the mean energy of emitted secondary electrons, ε_i.

We expect, but have not yet included in the present model, that the plasma electron density should increase dramatically with use of metal oxides, yielding high γ_i values. The secondary electron emission coefficient affects the discharge and a parametrization of the γ_i value is presented on Chapter 6 in order to have a better understanding of its impact on the thruster performance.

The interaction with the walls is modelled by a balance of incident fluxes, both for electrons and electron energies:

$$\mathbf{n} \cdot \mathbf{\Gamma}_e = \left(\frac{1}{2} v_{e,th} n_e \right) - \sum \gamma_i (\mathbf{\Gamma}_i \cdot \mathbf{n}) \tag{3.29}$$

$$\mathbf{n} \cdot \mathbf{\Gamma}_\varepsilon = \left(\frac{5}{6} v_{e,th} n_\varepsilon \right) - \sum \gamma_i \varepsilon_i (\mathbf{\Gamma}_i \cdot \mathbf{n}) \tag{3.30}$$

where $v_{e,th}$ is the electron thermal speed, the first term on the right side of Equation 3.29 represents the electrons lost in the wall due to random motion within a few mean free paths, the second term of the right side of Equation 3.29 depicts the secondary emission flux and the second term of right side of Equation 3.30 refers to secondary emission energy flux.

The surface reaction is specified in terms of sticking coefficients, γ_f, which has a value of 1 over the reactive surfaces such as the cathode, and a value of 0 over non-reactive surfaces

$$R_{e,wall} = \left(\frac{\gamma_f}{1-\gamma_f/2}\right)\frac{1}{(\Gamma_{tot})^m}\frac{1}{4}\sqrt{\frac{8RT_s}{\pi M_n}}\prod_{k=1}^{Q} c_k \tag{3.31}$$

where Γ_{tot} is the total electron flux incident on the cathode, m is the order of the reaction minus 1, c_k is the molar concentration of species k, R is the gas constant, T_s is the surface temperature, M_n is the mean molecular weight of the gas mixture and Q is the total number of considered species.

We considered self-consistent kinetic models for each gas, which includes electron-impact reactions (elastic and ionization), and chemical kinetics reactions in order to model the behavior of the gas during the discharge. The rate coefficients of the processes considered in the kinetic model are detailed in Tables 3.1, 3.2 and 3.3.

Two sets of coupled transport equations for charged species and neutral species were solved simultaneously, linked by kinetic generation terms, and describing processes taking place within the weakly-ionized plasma, which includes quasi-neutral effects, and non-neutral effects such as cathode and anode sheaths.

Given that the calculation process is time consuming and memory intensive and we aim to increase the speed of the numerical calculations, our model depicts only the most significant species since the amount of reactions can grow rapidly and the calculation times become impractical, see Loureiro and Ferreira (1986); Gousset et al. (1991). Thus, even if not fully developed kinetic models, in the argon case we considered three species Ar, Ar^* (a pool of all electronically excited states of argon in one compound state with energy threshold of 11.5 eV), Ar^+ and Ar_2^+ which is formed by means of charge exchange collision with neutrals; for nitrogen, we take into account N_2, N_2^+, N, N^+ and N_4^+ and for the electronegative oxygen, we include O_2, O_2^+, O_2^-, O, O^+, and O^- for the fundamental electronic states only (not considering vibrational and rotational states in the cases of molecules). We have a consistent treatment of both the electron and heavy particle kinetics and, therefore, the first step to this goal is to describe the electron kinetics as electrons gain energy from the electric field, which they subsequently redistribute among the atomic and molecular internal degrees of freedom, mainly dissociation and ionization. These processes of gain and loss of electron energy are adequately described by the electron Boltzmann equation, but since we are interested in the main impact of the plasma parameters on the thrust performance, in our study we use the Maxwellian distribution for the electron energy distribution function (EEDF), instead of a Boltzmann distribution function, to obtain the electron rate coefficients and the electron transport and collisional data under discharge conditions. These electron information is necessary in order to predict the populations of the various species in the discharge. Therefore, the Maxwellian

electron energy distribution function must be solved simultaneously with a system of rate balance equations for the various heavy particle species.

For nitrogen at lower pressure we should expect as dominant species N_2^+ and N^+, but especially at higher gas density other species might be present and should be included such as N_4^+ and N_3^+. Similarly for oxygen corona discharge, when the pressure increases the dominant species changes (see more on the topic on Capitelli et al. (2000); Wang et al. (2017); Gordiets et al. (1998a,b)).

Table 3.1: Electron-impact and chemical reactions with rate coefficients for argon discharge.

Reaction	Rate coefficient[1] [m^3/s or m^6/s]	Reference
$e+Ar \rightarrow e+Ar$	$f(\sigma)$	Morgan (2015)
$e+Ar \rightarrow e+Ar^*$	$f(\sigma)$	Morgan (2015)
$e+Ar \rightarrow 2e+Ar^+$	$f(\sigma)$	Morgan (2015)
$e+Ar^* \rightarrow 2e+Ar^+$	$f(\sigma)$	Morgan (2015)
$e+Ar_2^+ \rightarrow Ar^*+Ar$	$5.06\times10^{-15}(T_e)^{-0.67}$	O'Malley et al. (1972)
$Ar^*+Ar^* \rightarrow e+Ar+Ar^+$	6.2×10^{-16}	Bogaerts and Gijbels (1995); Lam et al. (2000)
$Ar^*+Ar \rightarrow Ar+Ar$	3.0×10^{-21}	Bogaerts and Gijbels (1995); Lam et al. (2000)
$Ar^+ + 2Ar \rightarrow Ar_2^+ + Ar$	2.25×10^{-43}	Fitzwilson and Chanin (1973)

[1] $f(\sigma)$ symbolizes that electron-impact reactions rates are functions of cross-section data.

Table 3.2: Electron-impact and chemical reactions with rate coefficients for nitrogen discharge.

Reaction	Rate coefficient[1] [m^3/s or m^6/s]	Reference
$e+N_2 \rightarrow e+N_2$	$f(\sigma)$	IST-Lisbon (2015)
$e+N_2 \rightarrow 2e+N_2^+$	$f(\sigma)$	IST-Lisbon (2015)
$e+N_2 \rightarrow e+2N$	$f(\sigma)$	Itikawa (2015)
$e+N_2^+ \rightarrow 2N$	$2.8\times10^{-13}(300/T_e)^{0.5}$	Kossyi et al. (1992)
$e+N_2^+ + N_2 \rightarrow 2N_2$	$2.6\times10^{-39}(300/T_e)^{1.5}$	Kossyi et al. (1992)
$e+N_2^+ \rightarrow N_2$	$1\times10^{-25}(T_g/T_e)^{4.5}$	Kossyi et al. (1992)
$e+N_4^+ \rightarrow N_2+N_2$	$2\times10^{-12}(T_g/T_e)^{0.5}$	Kossyi et al. (1992)
$2e+N^+ \rightarrow e+N$	$2\times10^{-39}(10^4/T_e)^{6.04}$	Prevosto et al. (2016)
$e+N^+ + N_2 \rightarrow N+N_2$	$6.07\times10^{-34}(T_e)^{-2.5}$	Prevosto et al. (2016)
$N_2^+ + N \rightarrow N^+ + N_2$	$7.2\times10^{-19}\exp(T_g/300)$	Kossyi et al. (1992)
$N_4^+ + N_2 \rightarrow N_2^+ + 2N_2$	$2.1\times10^{-22}\exp(T_g/121)$	Kossyi et al. (1992)
$N_2^+ + 2N_2 \rightarrow N_4^+ + N_2$	5.0×10^{-41}	Kossyi et al. (1992)
$N+N+N_2 \rightarrow N_2+N_2$	$8.27\times10^{-46}\exp(500/T_g)$	Kossyi et al. (1992)
$N^+ + N + N_2 \rightarrow N_2^+ + N_2$	1×10^{-41}	Kossyi et al. (1992)
$N_4^+ + N \rightarrow N^+ + N_2 + N_2$	1×10^{-17}	Kossyi et al. (1992)

[1] $f(\sigma)$ symbolizes that electron-impact reactions rates are functions of cross-section data.

It is well known that the vibrational levels of ground-state $N_2(X^1\Sigma_g^+,v)$ molecules play a central role in nitrogen discharge (see Guerra et al. (2004)). The complexity of nitrogen arises from the

Table 3.3: Electron-impact and chemical reactions with rate coefficients for oxygen discharge.

Reaction	Rate coefficient[1] [m^3/s or m^6/s]	Reference
$e + O \rightarrow e + O$	$f(\sigma)$	Morgan (2015)
$e + O_2 \rightarrow e + O_2$	$f(\sigma)$	Morgan (2015)
$e + O_2 \rightarrow e + 2O$	$f(\sigma)$	Morgan (2015)
$e + O_2 \rightarrow 2e + O_2^+$	$f(\sigma)$	Morgan (2015)
$e + O \rightarrow 2e + O^+$	$f(\sigma)$	Morgan (2015)
$e + O_2 \rightarrow O_2^-$	$f(\sigma)$	Morgan (2015)
$2e + O_2^+ \rightarrow e + O_2$	$1 \times 10^{-31}(300/T_e)^{4.5}$	Kossyi et al. (1992)
$e + O_2^+ + O_2 \rightarrow 2O_2$	$6 \times 10^{-39}(300/T_e)^{1.5}$	Kossyi et al. (1992)
$e + O_2^+ \rightarrow O + O$	$2 \times 10^{-13}(300/T_e)$	Kossyi et al. (1992)
$e + O + O_2 \rightarrow O + O_2^-$	1×10^{-43}	Kossyi et al. (1992)
$e + O + O_2 \rightarrow O^- + O_2$	1×10^{-43}	Kossyi et al. (1992)
$O^+ + O + O_2 \rightarrow O_2^+ + O_2$	1×10^{-41}	Kossyi et al. (1992)
$O^+ + O_2 \rightarrow O_2^+ + O$	$3.3 \times 10^{-17}\exp(-0.00169T_g)$	Kossyi et al. (1992)
$O_2^- + O \rightarrow O^- + O_2$	3.3×10^{-16}	Tatarova et al. (1997)
$O^- + O \rightarrow O_2 + e$	1.4×10^{-16}	Tatarova et al. (1997)
$O_2^- + O_2 \rightarrow 2O_2 + e$	$2.7 \times 10^{-16}(T_g/300)^{0.5}\exp(-5590/T_g)$	Tatarova et al. (1997)

[1] $f(\sigma)$ symbolizes that electron-impact reactions rates are functions of cross-section data.

strong coupling between different kinetics such as electron, vibrational, chemical and surface kinetics. Disregarding non-equilibrium vibrational kinetics of nitrogen (of diatomic molecules such as oxygen) will affect the pumping of vibrational quantum states through e-V collisions that are accompanied by molecular dissociation. Since atoms are not as efficient as molecules in the momentum transfer process, we expect that V-V mechanisms could reduce the thrust-to-power ratio. Our model, which is still open to improvement, depicts only the most significant species since the amount of reactions can grow rapidly and the calculations become unpractical.

3.3.4 Fluid governing equations

The fluid is assumed to be incompressible since the pressure is considered fairly constant and the flux is viscous laminar which is modelled using the Navier-Stokes equation. An external volume force $\mathbf{f} = \rho_c \mathbf{E}$ is included in the equation in order to couple with electric field forces experienced by the charged particles in the plasma bulk.

$$\rho_f \frac{\partial \mathbf{u}}{\partial t} + \rho_f(\mathbf{u} \cdot \nabla)\mathbf{u} = -\nabla p + \nabla \cdot \left[\eta \left(\nabla \mathbf{u} + (\nabla \mathbf{u})^T\right)\right] + \mathbf{f} \tag{3.32}$$

where ρ_f is the fluid density, $\mathbf{u}$ is the fluid velocity, p is the pressure and η is the dynamic viscosity.

Equation 3.32 is a balance of forces acting on the fluid, where its left hand side represents a sum of inertial forces, namely temporal variation and convection forces. In addition, the first term on the right hand side of Equation 3.32 accounts for pressure forces (pressure gradient), the second

Table 3.4: Surface reactions and SEEC values.

Reaction	Surface[1]	γ_i
$Ar^* \rightarrow Ar$	W, A, C	0
$Ar^+ \rightarrow Ar$	W, A	0
$Ar^+ \rightarrow Ar$	C	0.05
$Ar_2^+ \rightarrow Ar$	W, A	0
$Ar_2^+ \rightarrow Ar$	C	0.05
$N \rightarrow 0.5N_2$	W, A, C	0
$N^+ \rightarrow 0.5N_2$	W, A	0
$N^+ \rightarrow 0.5N_2$	C	0.05
$N_2^+ \rightarrow N_2$	W, A	0
$N_2^+ \rightarrow N_2$	C	0.05
$N_4^+ \rightarrow 2N_2$	W, A	0
$N_4^+ \rightarrow 2N_2$	C	0.05
$O \rightarrow 0.5O_2$	W, A, C	0
$O^+ \rightarrow 0.5O_2$	W, A	0
$O^+ \rightarrow 0.5O_2$	C	0.05
$O^- \rightarrow 0.5O_2$	W, A, C	0
$O2^+ \rightarrow O_2$	W, A	0
$O2^+ \rightarrow O_2$	C	0.05
$O2^- \rightarrow O_2$	W, A, C	0

[1] W: boundary walls, A: anode, C: cathode.

term represents the viscous forces and the third term represents the external electrical force acting on the fluid.

Since the fluid is assumed incompressible for each gas considered in our study, the volume continuity equation is written as

$$\nabla \cdot \mathbf{u} = 0 \tag{3.33}$$

3.3.5 Secondary electron emission

When ions impinge a metallic surface with the right amount of energy they may cause electrons to be released out of such material, this mechanism is known as secondary electron emission or SEE. In plasma physics when the surface in question is an electrode, e.g. a cathode, it is called secondary electron emission from the cathode because electrons (from a "secondary source") are introduced into the surrounding plasma while ions are hitting the electrode's surface and are getting neutralized in the process.

There are several mechanisms that could lead to the emission of electrons from a metallic surface such as photon bombardment, high temperatures, strong electric fields, amongst others. The most relevant case for the present study is the ion bombardment so other processes will be neglected (for more on secondary electron emission see Dekker (1958)).

Considered in the present work are the set of surface kinetic processes of atomic and/or molecular ions re-association at the walls, depending on the gas, and such processes are collected in Table 3.4 along with the secondary electron emission coefficient considered at each of the surfaces, boundary and electrodes surfaces. We consider a uniform secondary electron emission coefficient of $\gamma_i = 0.05$ for the neutralization reactions of every cathode along the three gases. Secondary electrons are emitted from the cathode surface with an energy estimated by the ionization energy threshold and a working function of 5 eV for our model. More specific values of γ_i for each gas and cathode materials is considered in Chapter 6 (see Raizer (1991); Granados et al. (2017a) for more on the topic). Due to the lack of data, surface kinetics is simplified here so that surface recombination and deactivation are treated as effective gas-phase processes.

The sticking coefficient denotes the probability of each reaction to occur at the considered surface. In our case, the neutralization of ions and the drop of excited species into their ground-states is modeled with a probability of 1 (all impinging atoms or molecules stick).

3.3.6 The plasma electric circuit model

The plasma discharge needs to be strong enough so the gas can be ionized around the anode but not too strong that an arc forms between electrodes. EHD thrusters work best in the glow discharge regime. As depicted on Figure 3.4, a RC coupling circuit is used in series with the direct-current source in order to avoid the arc regime between its electrodes. The ballast resistor (R_b) is a tuning parameter that changes amongst simulation cases since a low value could favor an unphysical arc formation with the current increasing exponentially and a high value could reduce the plasma's onset potential, reducing the electric field strength and extinguishing the plasma discharge. The blocking capacitance (C_b) is used to avoid voltage peaks between electrodes. The relation between the input voltage (V_{in}) and the electrodes voltage (V_{plasma}) is the following:

$$V_{plasma} = V_{in} - I_p R_b - R_b C_b \frac{dV_{plasma}}{dt} \tag{3.34}$$

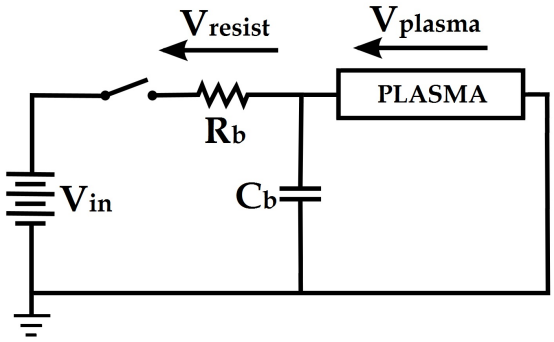

Figure 3.4: RC series coupling circuit.

where I_p represents the current between electrodes and includes the ions and electrons densities at the electrodes walls, and it is defined as:

$$I_p = -\int (\mathbf{n}\cdot\mathbf{J}_i + \mathbf{n}\cdot\mathbf{J}_e) dS \tag{3.35}$$

where $\mathbf{n}\cdot\mathbf{J}_i$ is the normal ion current density at the wall and $\mathbf{n}\cdot\mathbf{J}_e$ is the normal electron current density at the wall. The minus sign on the right hand side of Equation 3.35 corrects for the normal components of the current densities pointing outwards on the surface of the electrodes.

The power spent in order to create and sustain the plasma is calculated from the circuit as:

$$P = V_{plasma} I_p \tag{3.36}$$

Since the ballast resistor limits the total current delivered to the electrodes, we may notice that an immediate comparison must be made with care, since the plasma conductivity is, naturally, different for each gas, implying a different resistance for every case studied. Controlling the ballast resistance allows controlling the current, which in turn, allows increasing the net produced thrust up to a value that provides the conditions for arc formation.

3.3.7 Limitations and remarks on the model

In most fluid models, secondary electron emission is strong enough to enhance electron energy losses at the walls so that the electron velocity distribution function is anisotropic, for example in collisionless thrusters plasma (in particular near the wall/electrodes) and non-Maxwellian, distinguishing the bulk electrons from the beams of secondary electrons emitted from the walls. We should point out that Kaganovich et al. (2007) introduces a model that, although applies to crossed electric and magnetic field configuration, which is not our case study, considers appropriate electron fluxes to the wall and incidentally, they found that in a direction parallel to the walls the electron distribution function is possibly close to a Maxwellian. For more information about the situation in presence of cross electric and magnetic fields, see also the Tutorial by Boeuf (2017) where the author explains the physics and modeling of Hall thrusters, which are considerably different from the EHD thrusters investigated in the present article.

As is well known, the cause of the EEDF to tend to a Maxwellian is the electron-electron collisions as described, for example, on Rockwood (1973, 1974); Sá et al. (1992). Also, the use of a Maxwellian distribution function overestimates the rate coefficients of inelastic collisions, in particular ionization rates, due to a more populated high energy tail of the EEDF. As the influence of electron-electron collisions depends essentially on the ionization degree, the full use of Boltzmann equation, including the consideration of electron-electron collisions, shows that the inelastic rate coefficients may be significantly increased for ionization degrees of 10^{-5} or higher, but only at low mean-energy due to the rapid fall of the electron-electron cross section collisions as electron energy increases. Actually, the conditions where electron-electron collisions are important occur typically in discharges sustained by stepwise ionization and where EEDF is influenced by electron

collisions with excited neutrals, in particular super-elastic collisions which promote electrons into the tail of the EEDF. For more on the electron-electron collisions role in plasma discharges see Sá et al. (1992); Hagelaar and Pitchford (2005).

Our choice of a Maxwellian distribution may be misleading outside a certain range of electron temperatures, mainly below the energy threshold for vibrational levels in molecular gases and above the ionization threshold, where the Maxwellian reportedly gives higher electrons energy.

The use of a Maxwellian EEDF certainly leads to a deviation from the more representative EEDF (obtained by solving the Boltzmann equation for electrons) not able to represent electrons with higher energy populating the tail of the distribution. However, the relatively low applied voltages and the average electron temperature of the order of some eV, well below the gas ionization threshold makes the approximation reasonable, since the electron temperature, T_e, is usually much smaller than the electronic transition energy between two states i and k, ΔE_{ik} ($T_e \ll \Delta E_{ik}$), the rate coefficient of the process varies like $\approx \exp(-\Delta E_{ik}/T_e)$ as seen on Fridman and Kennedy (2004).

Absent from our calculations of the EEDF are the electron collisions with vibrationally excited levels of molecules, either inelastic or super-elastic. According to Loureiro and Ferreira (1986), the inclusion of these e-V collisions would, presumably, produce a significant enhancement of the high energy tail of the EEDF, as a result of e-V super-elastic collisions, increasing the rate coefficients for the various elementary processes induced by electron impact.

In the kinetic model of the heavy species of the molecular gases, we deal with the molecules as if they were atoms, neglecting the internal vibrational and rotational levels. The latter is a limitation of our work due to the complexity of molecular gases which arises from the strong coupling between different kinetics such as electron, vibrational, chemical, and surface kinetics.

The study of the surface kinetics is noteworthy as many of the characteristics of plasma reactors are in practice controlled by walls reactions. As a matter of fact, the surface kinetics affects vibrations due to its strong influence in the atomic concentration and the direct deactivation of vibrationally excited levels at the wall (see Gordiets et al. (1995); Marković et al. (1994)). In addition, wall processes are known to play an important part in the thermal balance of plasmas, as shown by Guerra (2006), including its role in the particle balance of species. In particular, the atomic re-association at the wall being determinant in oxygen and nitrogen discharges (see Pinheiro et al. (1996)).

3.4 Thruster design

The conducted simulations are based on single-stage EHD thrusters with three different cathode configurations, namely: conical cathode, cylindrical cathode and funnel-like cathode. 3D representations of the configurations along side their actual simulation domains are depicted on Figures 3.5, 3.6 and 3.7. A list of geometrical parameters such as gap between electrodes and cross sectional areas of input and output of the thruster nozzles can be found in Table 3.5.

The reactor is schematically shown in Figure 3.10, depicting the axisymmetric computational domain and the thruster geometry. For the general boundary conditions, we consider the fluid to

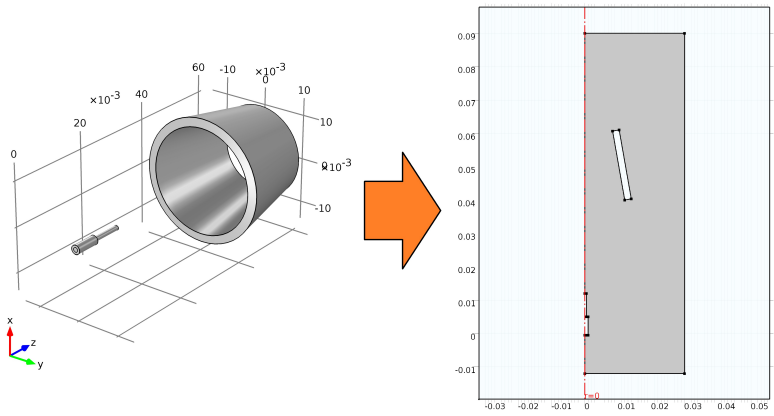

Figure 3.5: Conical cathode, geometry and simulation domain with units in m.

have zero velocity at the surface of both electrodes and the simulation edge parallel to the axis of symmetry in order to simulate a wind tunnel. In the fluid entrance at the bottom of the domain we consider a pressure $p \geq p_0$, with p_0 the average gas pressure, so we solve for both the velocity and pressure at the boundary but guarantee to avoid any back flow. The top domain boundary is an open end with the same pressure as the gas, allowing it to flow and solving for the velocity.

The distance between electrodes, d, is designated as the distance between two parallel planes tangent to both electrodes according to Figure 3.8, since the cathode is a hollow structure and this definition simplifies the notion of distances for the purposes of the study.

In order to calculate the total thrust produced by the flux of gas going through the EHD thruster, we consider $v_z(r)$, the axial component of the exhaust gas velocity, which is normal to the nozzle's output cross sectional area, to be time invariant, but space dependent on the radial component in cylindrical coordinates. The time invariance is a valid approximation since the steady-state is reached within milliseconds after the corona formation (see next chapter). The radial dependency of the gas normal velocity component allows to write the following expression for the total thrust:

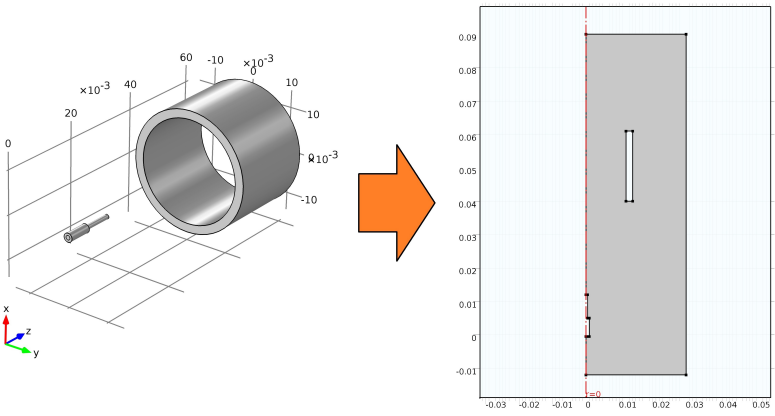

Figure 3.6: Cylindrical cathode, geometry and simulation domain with units in m.

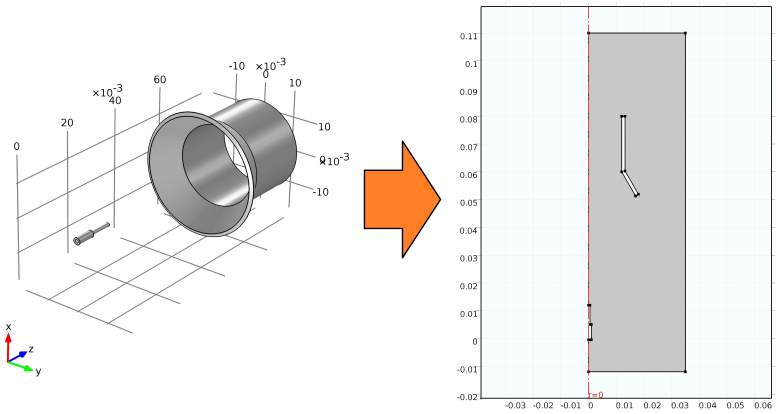

Figure 3.7: Funnel cathode, geometry and simulation domain with units in m.

$$T = 2\pi\rho_f \int_0^R r v_z^2 dr \tag{3.37}$$

where r is the distance from the center of the thruster symmetry axis ($r = 0$) to the cathode's wall, located at R.

A set of boundary conditions were established in order to solve the differential equations: we consider the thruster to be immerse in a duct with open ends, i.e. no background gas flow, zero gas velocity at the duct wall and an exit boundary at a constant pressure.

Important parameters for the improvement of the performance of EHD thrusters are the duct size and the input stream velocity in relation to the thruster outflow velocity resulting from the total electric body force. Three types of thrusters with different duct geometry have been considered: single stage units with conical, cylindrical and funnel cathodes. The duct design has an impact on the amount and divergence of ion charge flux across the generated plasma plume and can also have an impact on the fraction of ions and electrons that get to full acceleration, regulating the onset of major loss mechanisms, e.g., the electron back-streaming to the anode. All three thrusters consider a pin-like anode with an axial length of 1.25 cm and a 2.8 cm gap between electrodes (unless specified otherwise) for comparison purposes.

Since the problem in our hands is highly non-linear and time-dependent, analytical solutions of the equations in two dimensions becomes impractical. We employ, then, numerical techniques

Table 3.5: Two-dimensional axysimmetrical EHD thruster's electrodes geometrical dimensions.

	Cathode geometry		
Parameter	Conical	Cylindrical	Funnel
Input area, A_i (cm^2)	4.52	4.52	8.55
Output area, A_o (cm^2)	2.19	4.52	4.52
Gap between electrodes, d (cm)	2.8	2.8	2.8
Cathode axial length, L_c (cm)	2.0	2.2	3.0
Anode axial length, L_a (cm)	1.25	1.25	1.25

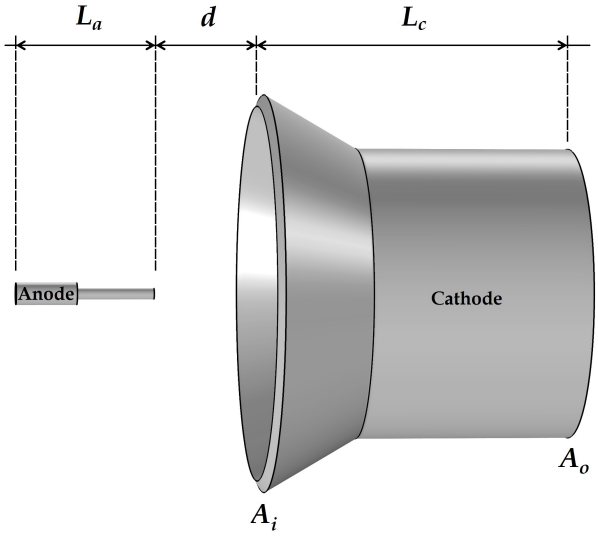

Figure 3.8: EHD thruster with the length of anode (L_a), length of conical cathode (L_c), gap distance (d), and input (A_i) and output (A_o) cross sectional areas.

based on finite element methods implemented with the software COMSOL Multiphysics® (see Comsol.com (2016)) for the calculation of the electrohydrodynamic thrusters evolution under several different simulation conditions until achieving a steady state.

According to the diagram presented on Figure 3.3, the flow dynamics considered in the simulations was implemented by using COMSOL® Laminar Flow module, which consists in a finite-element time-dependent study of the Navier-Stokes equation for incompressible fluids; and the kinetics module, plasma module, external electric circuit, and interaction with walls was implemented with COMSOL® DC Discharge - Plasma Module.

In order to solve the non-linear differential equations, exhibited by the two-dimensional model described on this chapter, the simulation domain needs to be divided into an adequate amount of small sub-domains, called finite elements, where the differential equations will be solved and tested on their vertices. Since there are regions where some phenomena take place with higher probability, we need to adapt a mesh of finite elements that is finer around such places than the rest of the space. The electrodes, for example, are regions where we define more boundary conditions (e.g., electric potential, secondary electron emission and heavy species impingement), so the region surrounding them has to contain the smallest elements in the domain. Figure 3.9 depicts a close look at the mesh surrounding the anode and how the triangular finite elements changes size across the domain. The implementation of the model may be seen in Appendix B.

The general structure of the EHD thrusters is presented on Figure 3.10, with the case of funnel-like cathode, showing the values of relevant geometrical dimensions, the axis of symmetry, the gas inlet and outlet.

The results presented on the following chapters exhibit the implementation of all the equations of the two-dimensional axysimmetrical EHD thruster using different electrodes geometries, working gases and simulations conditions in order to understand their behavior.

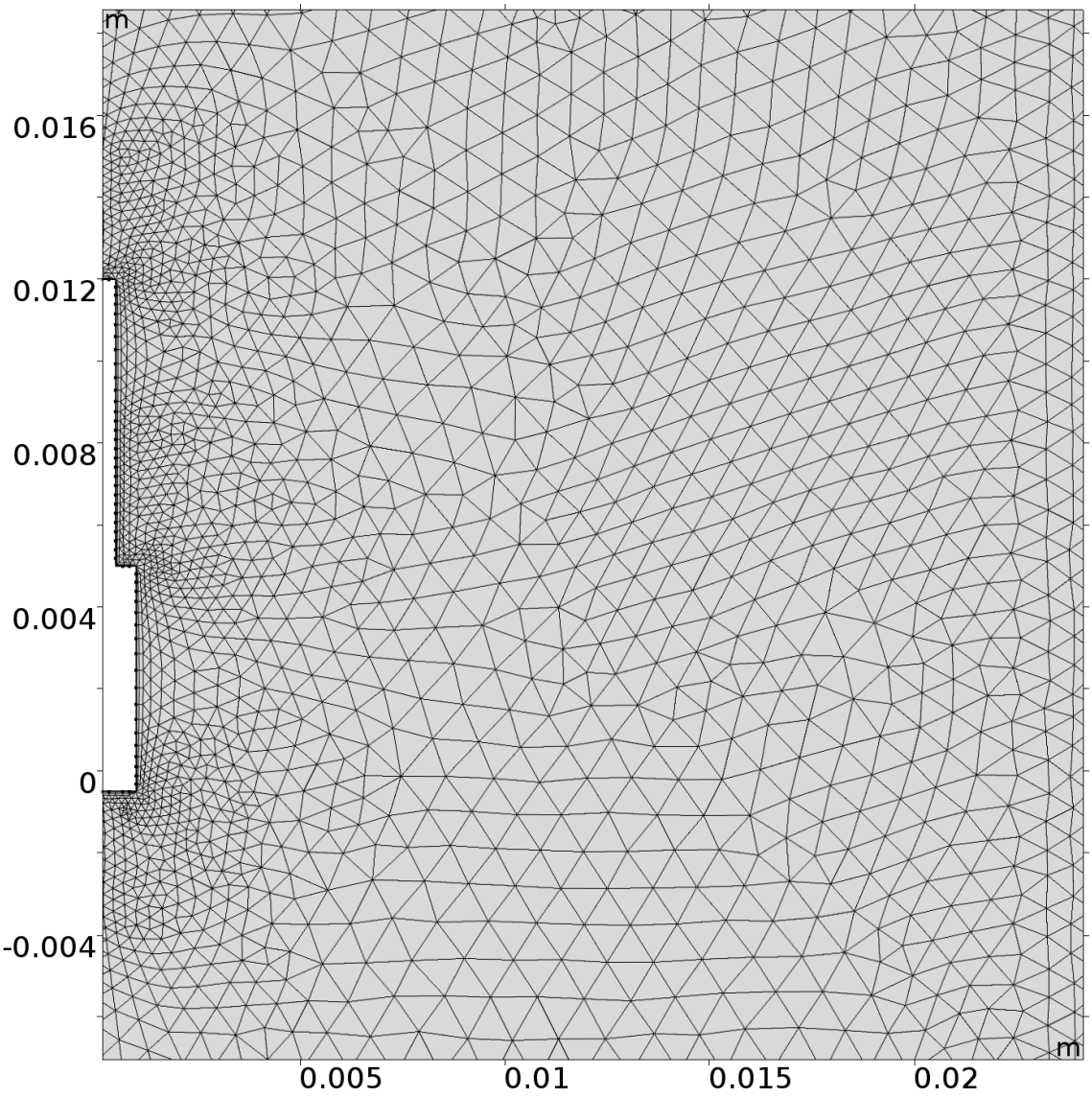

Figure 3.9: Mesh of simulation domain around anode, dimensions in m.

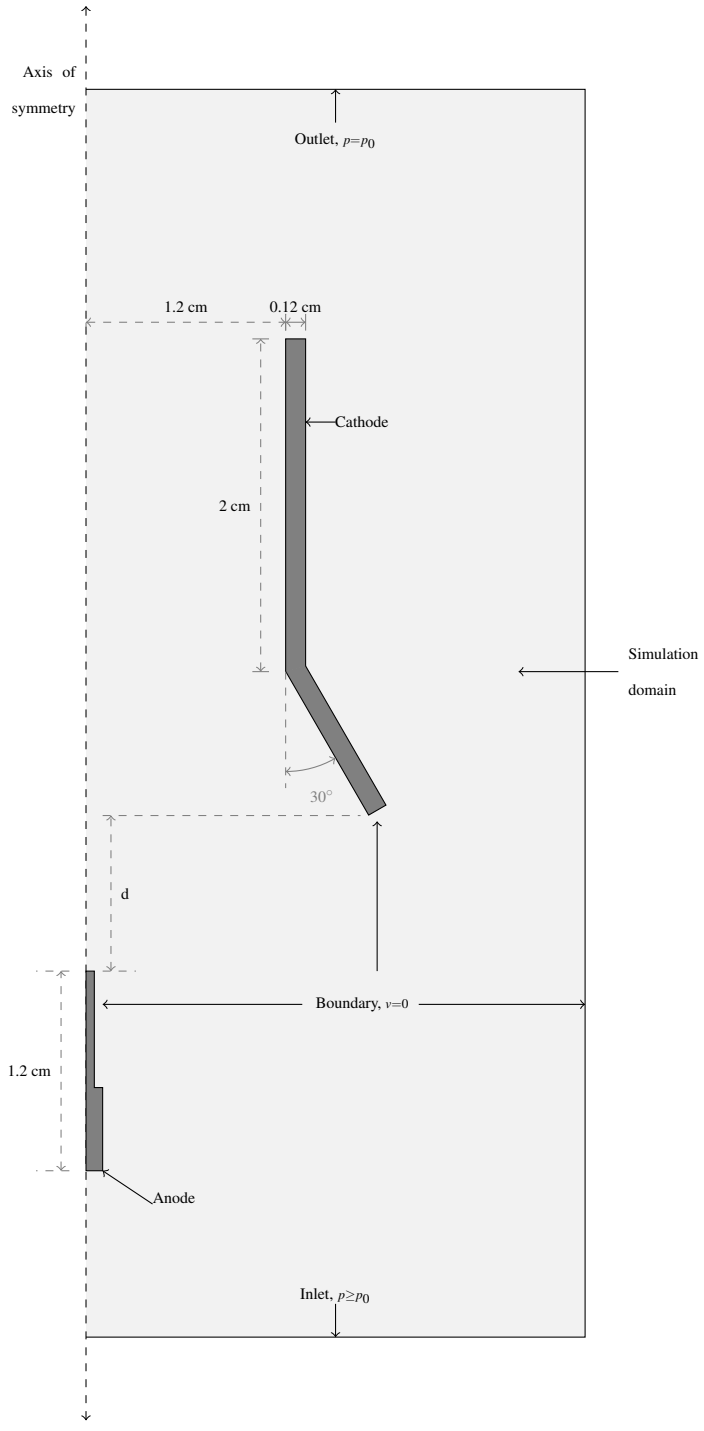

Figure 3.10: Boundary conditions and dimensions of simulation domain for funnel-like cathode geometry.

Chapter 4

Simulation of an electrohydrodynamic thruster at the gas pressure of 0.5 Torr

On the present chapter we analyze the results of simulating the self-consistent two-dimensional model from Chapter 3.3 with a constant gas pressure of 0.5 Torr ($\approx$ 67 Pa). The results, as presented in Granados et al. (2016), are divided by the geometry of the cathode electrode, (i.e. conical, cylindrical and funnel shapes), in which the use of each gas (i.e. argon, nitrogen and oxygen) is subscribed. We also describe the transitional nature of some variables during the discharge before they achieve steady state.

In order to simulate the EHD phenomena, we need to choose the global conditions such as the gas temperature, pressure, input voltage, among others. Table 4.1 summarizes the general simulation conditions considered on the present chapter.

4.1 Conical cathode

The potential distribution is a key factor in the design of the thruster, since the conversion of electric to mechanical energy is made primarily by the electric field. Figure 4.1 shows the electric potential along with the electric field vector at several spatial points for the three working gases

Table 4.1: Simulation conditions for EHD thruster at a gas pressure of 0.5 Torr.

Parameter	Value
Gas temperature, T_g	300 K
Pressure, p	0.5 Torr
Electric source voltage, V_{in}	500 V
Ballast resistance, R_b	[10-1500] MΩ
Blocking capacitance, C_b	1 pF
Secondary e^- emission coefficient, γ_i	0.05
Argon dynamic viscosity	2.23×10^{-5} Pa.s
Nitrogen dynamic viscosity	1.79×10^{-5} Pa.s
Oxygen dynamic viscosity	2.04×10^{-5} Pa.s

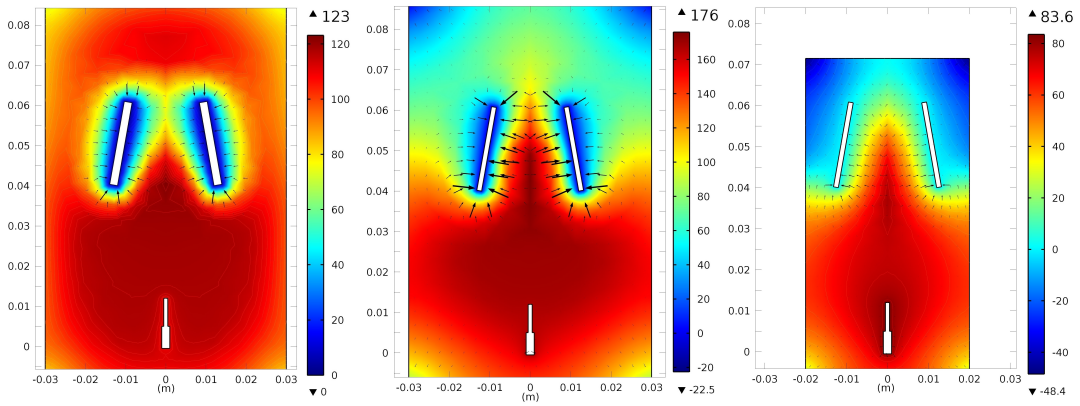

(a) Argon (b) Nitrogen (c) Oxygen

Figure 4.1: Electric potential distributions (V) for the three working gases with the conical cathode configuration. Electric field vectors represented in black arrows. $T_g = 300$ K and $p = 0.5$ Torr.

considered. The arrows indicate the electric field direction and its magnitude is relative to the length of the arrows. It is clear that the electric field is stronger in the regions near the cathodes when the discharge takes place and it is stronger in the case of nitrogen due to a higher potential gradient.

Due to the higher number of electron-impact and chemical reactions considered in the case of oxygen, for conical and cylindrical cathode geometries, we used a smaller computational grid for the results of the present chapter in order to decrease the calculation time, while maintaining the resolution of the finite elements in the center of the chamber.

An approximate relation between the gasdynamic parameters and the electric field, $p + \frac{\varepsilon_0}{2}E^2 = constant$, predicts that in regions of higher electric field the gas pressure is lower than in adjacent regions, see Roth (2001). The production of negative ions in oxygen result in a tendency to neutralize charge near the walls through ion-recombination processes, while in electro-positive plasma environment, the walls tend to be more strongly charged, with an overall favorable result in the case of nitrogen.

It is clear that, among the three different gases investigated, nitrogen gives a streamline more favorable to the gas acceleration as seen on Figure 4.2, which shows the fluid speed distributions. Nitrogen presents a peak velocity magnitude of 19.3 cm/s compared to the smaller values of 5.2 cm/s and 3.42 cm/s for argon and oxygen, respectively. Additionally, the fluid speed increases at the nozzle's output, regardless of the gas, due to the the narrower transverse area of the cone's end.

Figure 4.3 shows the fluid velocity components (axial, radial and total) at the output of the thruster. As depicted, the radial component of the fluid speed is negligible compared to the axial component while the axial component contributes to the major work propelling the gas along the central channel of the thruster. As expected from the boundary conditions of the fluid dynamics, the magnitude of all velocities reach zero at the electrodes walls.

Having argon as working gas creates a counteracting electric field at the outside of the thruster,

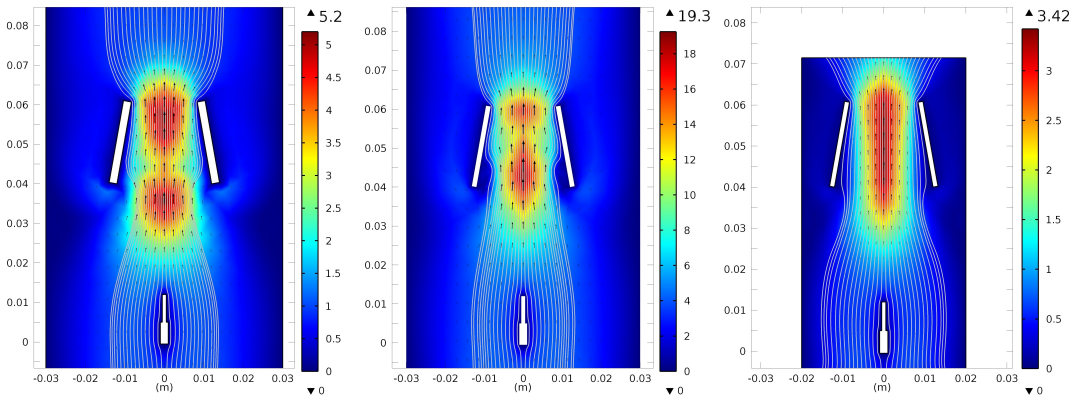

(a) Argon (b) Nitrogen (c) Oxygen

Figure 4.2: Fluid velocity distributions (cm/s) for the three working gases with the conical cathode configuration. Velocity field vectors represented in black arrows. $T_g = 300$ K and $p = 0.5$ Torr.

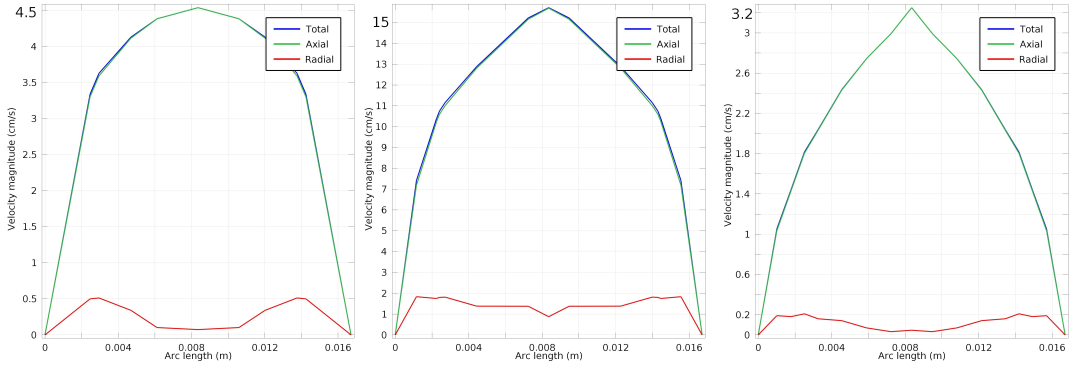

(a) Argon (b) Nitrogen (c) Oxygen

Figure 4.3: Fluid velocity components at output (cm/s) for the three working gases with the conical cathode configuration. $T_g = 300$ K and $p = 0.5$ Torr.

reducing its efficiency. Comparing oxygen with nitrogen, we may notice that in nitrogen the electric potential has a more steep descent, favoring momentum transfer to N_4^+ and N_2^+ ions. At 0.5 Torr, the concentration and volume production of the heavier N_4^+ ions exceeds slightly the other ions.

4.2 Cylindrical cathode

The cylindrical cathode geometry is presented as two parallel plates in the two-dimensional plane shown and due to the parallelism of the walls the electric field inside of the chamber points mostly radially as seen on Figure 4.4 for the three gases.

Clearly, the cylindrical cathode is not favorable in the case of argon, since the ions are mainly attracted to the walls by the electric field instead of axially along the chamber. The fact that electric potential spread through the chamber reaching its end induces an opposing electric field at the exit of the nozzle that ultimately produces an undesired stationary vortex as seen on Figure 4.5. Although laminar flux equations do not model complex vortex formations, in incompressible fluids vortices are created during the process of the separation of boundary layers. We are interested in the cases presenting laminar behavior and the vortex creation shows the limit of our approximation in this respect. At this pressure of 0.5 Torr, this is the only vortex that appeared once with oxygen or nitrogen as the working gases they were not formed.

As seen in Figure 4.5b, with nitrogen as the working gas, the descending plateau seen for the potential favors acceleration of ions, with the axial speed attaining about 8 $\mathrm{cm/s}$ at the nozzle's output. The nitrogen speed distribution shows the gas increasing its value at the entrance of the chamber accompanied by a compression of the fluid, followed by an expansion towards the walls and then gradually slowing down on its departure, a phenomenon that seems to point out that a geometry with a more axial electric field distribution on the chamber could avoid the fluid rushing towards the wall.

On Figure 4.6 we can observe the components of the velocities of the three gases for the cylindrical cathode. Argon gas shows a prominent negative axial component which corresponds to the stationary vortex at the output. The axial component of the nitrogen gas velocity shows a dip at the center of the thrust chamber due to a natural depletion of ions running from the center to the walls. The oxygen's axial component of the fluid velocity attains a maximum at the center, presumably due to the constriction of the discharge in electronegative gases.

4.3 Funnel cathode

Figure 4.7 shows the electric potential of the three gases, including the vectors representing the electric field for a funnel-like cathode. The nitrogen gas case showed a more axially distributed electric field with a larger potential gradient at the entrance of the chamber than the previous cathode configurations, mostly due to the bigger cross sectional area of impact for ions at the entrance of the chamber accompanied by a sliding surface for the neutrals to follow their path into

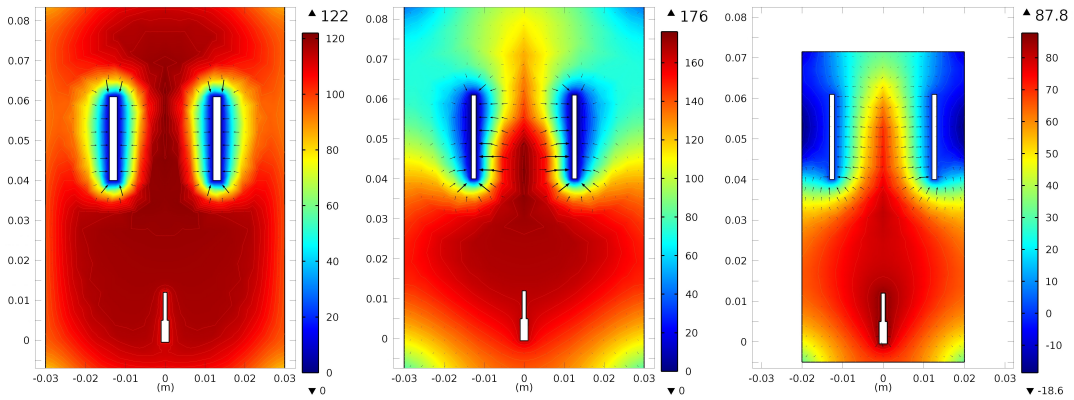

(a) Argon (b) Nitrogen (c) Oxygen

Figure 4.4: Electric potential distributions (V) for the three working gases with the cylindrical cathode configuration. Electric field vectors represented in black arrows. $T_g = 300$ K and $p = 0.5$ Torr.

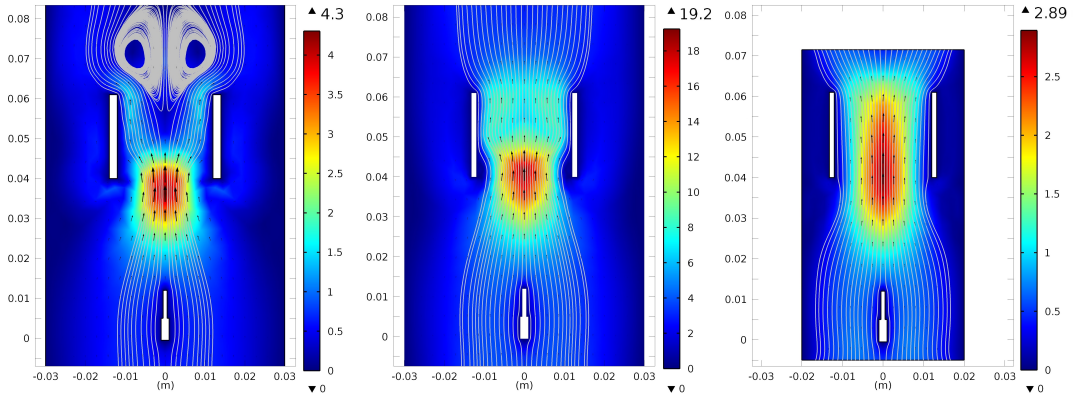

(a) Argon (b) Nitrogen (c) Oxygen

Figure 4.5: Fluid velocity distributions (cm/s) for the three working gases with the cylindrical cathode configuration. Velocity field vectors represented in black arrows. $T_g = 300$ K and $p = 0.5$ Torr.

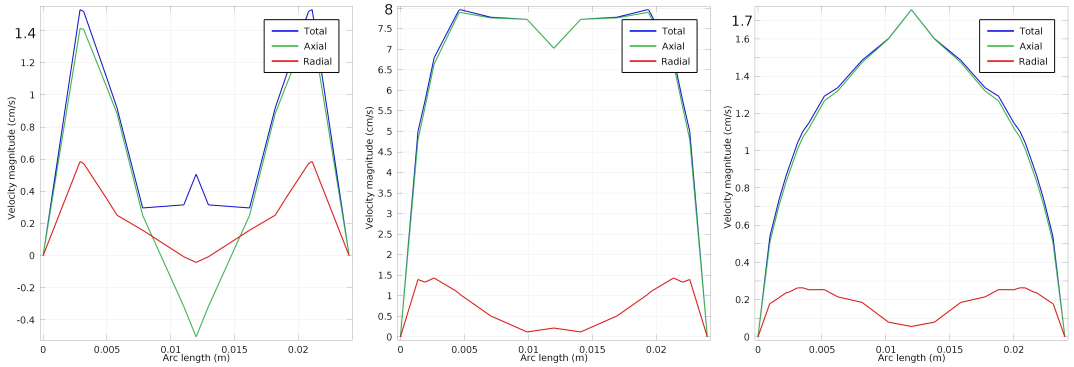

(a) Argon (b) Nitrogen (c) Oxygen

Figure 4.6: Fluid velocity components at output (cm/s) for the three working gases with the cylindrical cathode configuration. $T_g = 300$ K and $p = 0.5$ Torr.

the chamber. On the other hand, the funnel geometry does not seem favorable for neither argon nor oxygen, due to the previously observed tendency of the electric potential distribution not having steep descents and being too radially divergent.

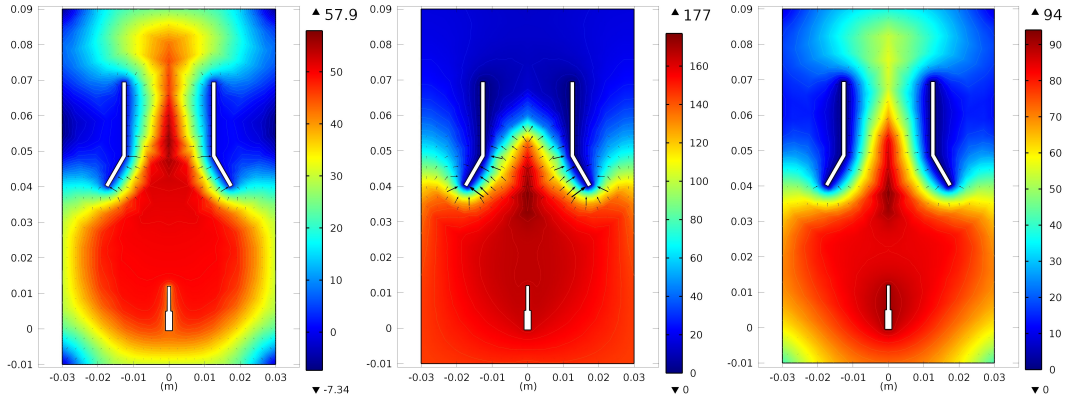

(a) Argon (b) Nitrogen (c) Oxygen

Figure 4.7: Electric potential distributions (V) for the three working gases with the funnel cathode configuration. Electric field vectors represented in black arrows. $T_g = 300$ K and $p = 0.5$ Torr.

We may notice on Figure 4.8 that, with nitrogen environment, the axial gradient of velocity is more prominent than in the other studied gases resulting in a higher fluid speed peak (23.7 cm/s), compared to the peak values of argon (1.40 cm/s) and oxygen (3.29 cm/s). Even though nitrogen achieves its peak velocity value at the entrance of the chamber, its value does not fall rapidly inside the chamber, as seen in Figure 4.9 from the peak value of the axial velocity ($\simeq$ 15.5 cm/s) at the output of the nozzle.

Nitrogen ions transferred a higher momentum to the neutral species than both argon and oxygen's with the funnel-like cathode, as reflected on highest axial velocity values, presumably due to the contribution of heavier ions (N_2^+ and N_4^+) as shown in Figure 4.9.

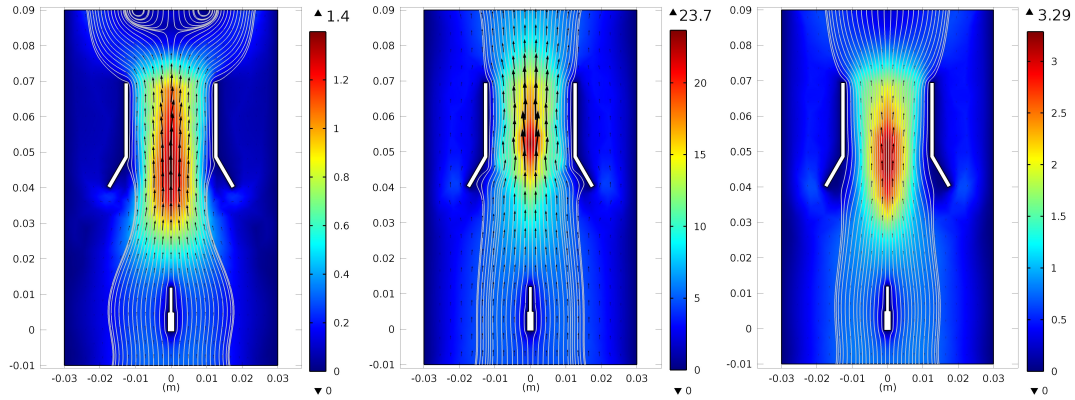

(a) Argon (b) Nitrogen (c) Oxygen

Figure 4.8: Fluid velocity distributions (cm/s) for the three working gases with the funnel cathode configuration. Velocity field vectors represented in black arrows. $T_g = 300$ K and $p = 0.5$ Torr.

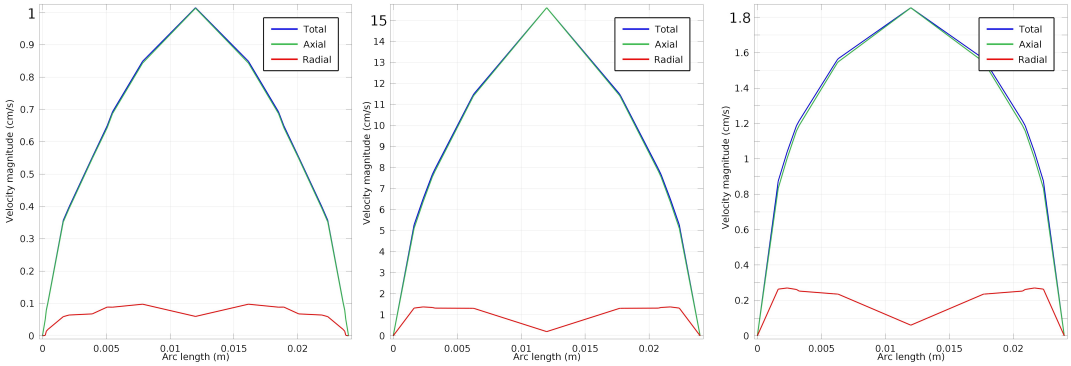

(a) Argon (b) Nitrogen (c) Oxygen

Figure 4.9: Fluid velocity components at output (cm/s) for the three working gases with the funnel cathode configuration. $T_g = 300$ K and $p = 0.5$ Torr.

4.4 Transient dynamics of various plasma parameters

Although results of the parameters of interest comprise of the steady state cases, the simulations are performed as time-dependent, defining an initial state and solving through the evolution of the DC discharge until the steady state is achieved. As depicted in Figure 4.10, the input voltage, V_{in}, has a ramp up function in order to give the simulation enough time to set the initial conditions before the discharge initiates with the voltage between electrodes. We can also observe the voltage applied between electrodes, commonly known as the onset potential and the complementary ballast resistor voltage which regulates the total current being supplied to the thruster. The role of the ballast is to stabilize the plasma, avoiding the creation of a conductive plasma bridge (arcing) between electrodes.

Figure 4.11 depicts the flux of secondary emission into a point of the cathode surface showing the transient nature of the discharge, raising its value dramatically during the onset potential transition, before reaching the steady state.

4.5 Thrust and thrust-to-power ratio

Table 4.2 shows the net thrust produced using the different gases in the thrusters' chamber, along with the power consumption and the Thrust-to-Power (T/P) ratio, a known parameter to determine the amount of thrust obtained for a given power input. Thrust-to-Power ratio is calculated as the quotient between the total produced thrust (T) and the power (P) needed to produce such thrust. According to Masuyama and Barret (2013): "EHD thrusters have documented thrust-to-power ratios as high as 26 mN/W, which is orders of magnitude greater than electrostatic propulsion systems used in space", which refers to the standard atmospheric pressure (760 Torr), implying an applicability in low altitudes. In our simulations we do not obtain T/P ratio as high as Masuyama's since the considered pressure is only a fraction (0.5 Torr), which represents the one of a near space altitude. Young (2009) remarks on the direct proportionality the pressure has on the thrust of EHD

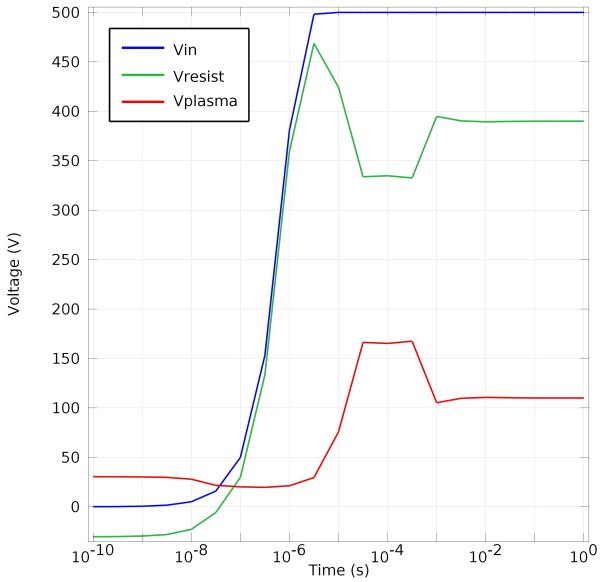

Figure 4.10: Transient of plasma onset voltage (V_{plasma}), ballast resistance voltage (V_{resist}) and input voltage (V_{in}) for the case of argon gas in the cone configuration cathode. $T_g = 300$ K and $p = 0.5$ Torr.

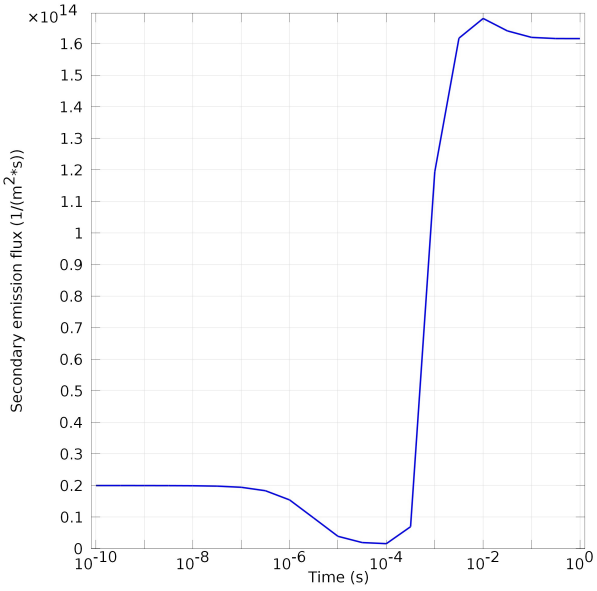

Figure 4.11: Transient of cathode's secondary electron emission flux for the case of argon gas in the cone configuration cathode. $T_g = 300$ K and $p = 0.5$ Torr.

Table 4.2: Net thrust, discharge power and thrust-to-power ratio produced by EHD thrusters on three cathode configurations using three different working gases at pressure $p = 0.5$ Torr.

Cathode configuration	Gas	Thrust, T (nN)	Power, P (mW)	T/P ratio (μN/W)
Conical	Ar	0.446	0.107	4.168
	N_2	3.440	0.140	24.590
	O_2	0.129	0.012	10.670
Cylindrical	Ar	0.074	0.143	0.518
	N_2	2.870	0.140	20.500
	O_2	0.088	0.014	6.477
Funnel	Ar	0.032	0.049	0.653
	N_2	5.181	5.508	0.941
	O_2	0.113	0.037	3.032

devices. In the case of nitrogen and for the conical cathode configuration we obtain the maximum T/P ratio, as 24.59 μN/W. Additionally, in all the cathode geometries analyzed, argon presented the poorest T/P ratio.

Considering the nitrogen gas, the funnel-like cathode presented the highest net thrust (5.181 nN), followed by the conical (3.440 nN) and cylindrical cases (2.870 nN), respectively.

4.6 Conclusions

In this chapter we investigated the effect of the single-stage EHD thruster geometry on the ability to achieve desired exhaust speeds, and primary efficiency considerations, such as the thrust-to-power ratio. For stability purposes, the gas discharge is assisted by an electric circuit controlling the glow-to-arc transition. To avoid excessive time-consuming calculations a reasonable self-consistent set of reactions and proper boundary conditions were considered.

In the funnel geometry, and contrary to the other considered geometries, oxygen has the highest value of T/P ratio, three times higher in magnitude when compared to nitrogen gas.

The most promising cathode geometry is the funnel-like configuration in terms of net produced thrust, specially when considering nitrogen gas, the most abundant gas in the atmosphere.

The next chapters will focus on the characteristics of the plasma discharge of the EHD thruster, particularly on the spatial distribution of all the ionized species and will show the role of relevant parameters, such as pressure, temperature, secondary electron emission, and the distance between electrodes.

Chapter 5

Simulation of an electrohydrodynamic thruster at the gas pressure of 10 Torr

On this chapter we will discuss the results of simulating the proposed model for EHD thrusters when the gas pressure gets increased to 10 Torr ($\approx$ 1.3 kPa) for the three cathode geometries and three working gases. Instead of organizing the results by cathode geometry, as in the previous chapter, we consider doing so by the variables of interest, i.e. spatial distributions of electron and ions densities, electric potential, velocity and thrust production. Most results of the chapter have been previously published by the author of this thesis (see Granados et al. (2017b)).

5.1 Spatial distributions of electron and ion densities

The spatial distributions of electron density shown in Figure 5.1 indicate the concentration of the steady state electron cloud during the discharge for each gas and cathode geometry. We should note that the highest concentration of electrons are situated near the anode of the thruster for argon and nitrogen, while for oxygen gas the concentration extends into the anodic region, located outside the chamber and regardless of the geometry, with a distribution centered at the electrode tip

Table 5.1: Simulation conditions for EHD thruster at a gas pressure of 10 Torr.

Parameter	Value
Gas temperature, T_g	300 K
Pressure, p	10 Torr
Electric source voltage, V_{in}	3000 V
Ballast resistance, R_b	[500-5000] MΩ
Blocking capacitance, C_b	1 pF
Secondary e^- emission coefficient, γ_i	0.05
Argon dynamic viscosity	2.23×10^{-5} Pa.s
Nitrogen dynamic viscosity	1.79×10^{-5} Pa.s
Oxygen dynamic viscosity	2.04×10^{-5} Pa.s

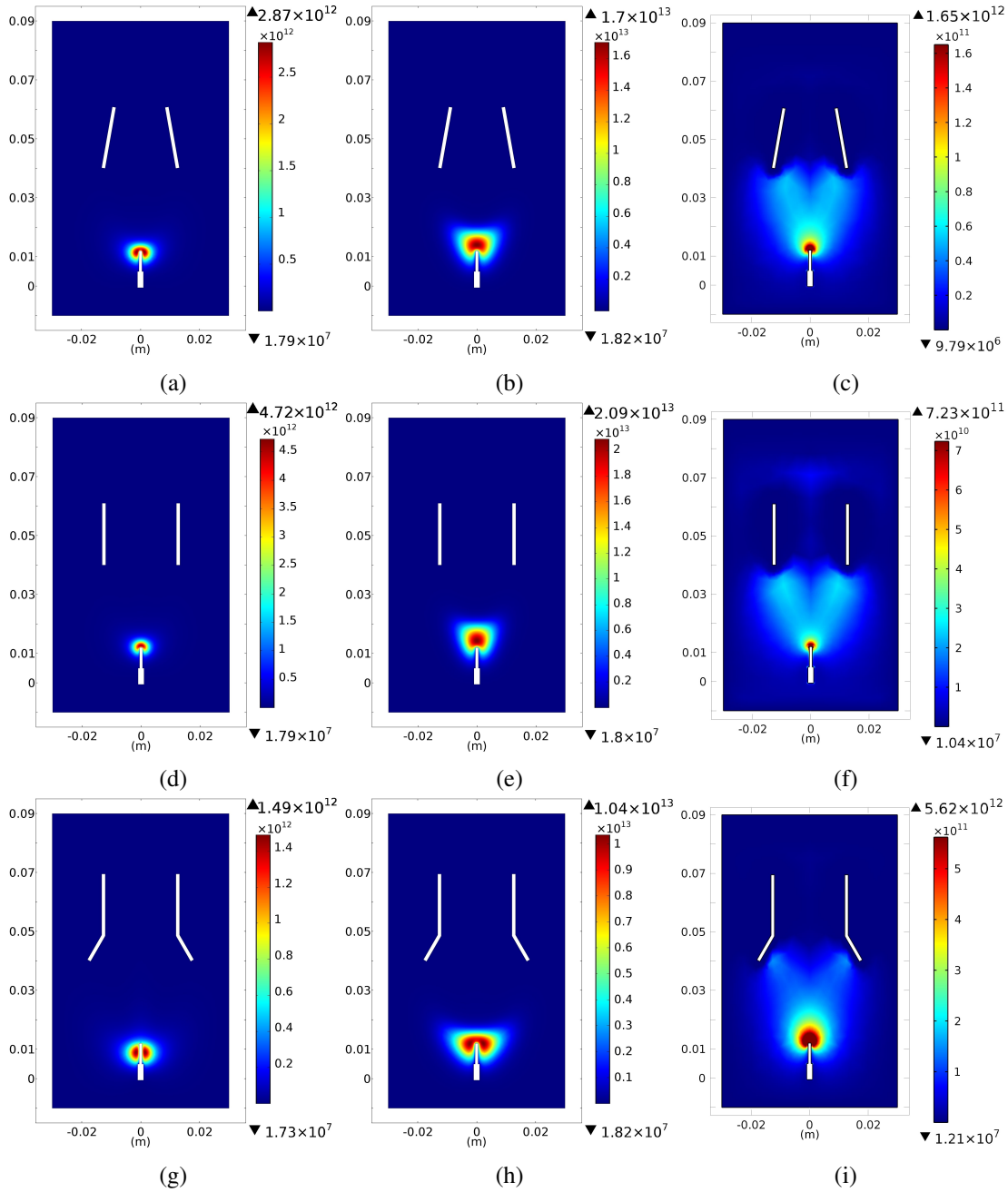

Figure 5.1: Spatial distributions of electron density (m^{-3}), for argon: (a), (d), (g); nitrogen: (b), (e), (h); and oxygen: (c), (f), (i) gases on cone (top row), cylindrical (center row) and funnel (bottom row) cathodes. $T_g = 300$ K and $p = 10$ Torr.

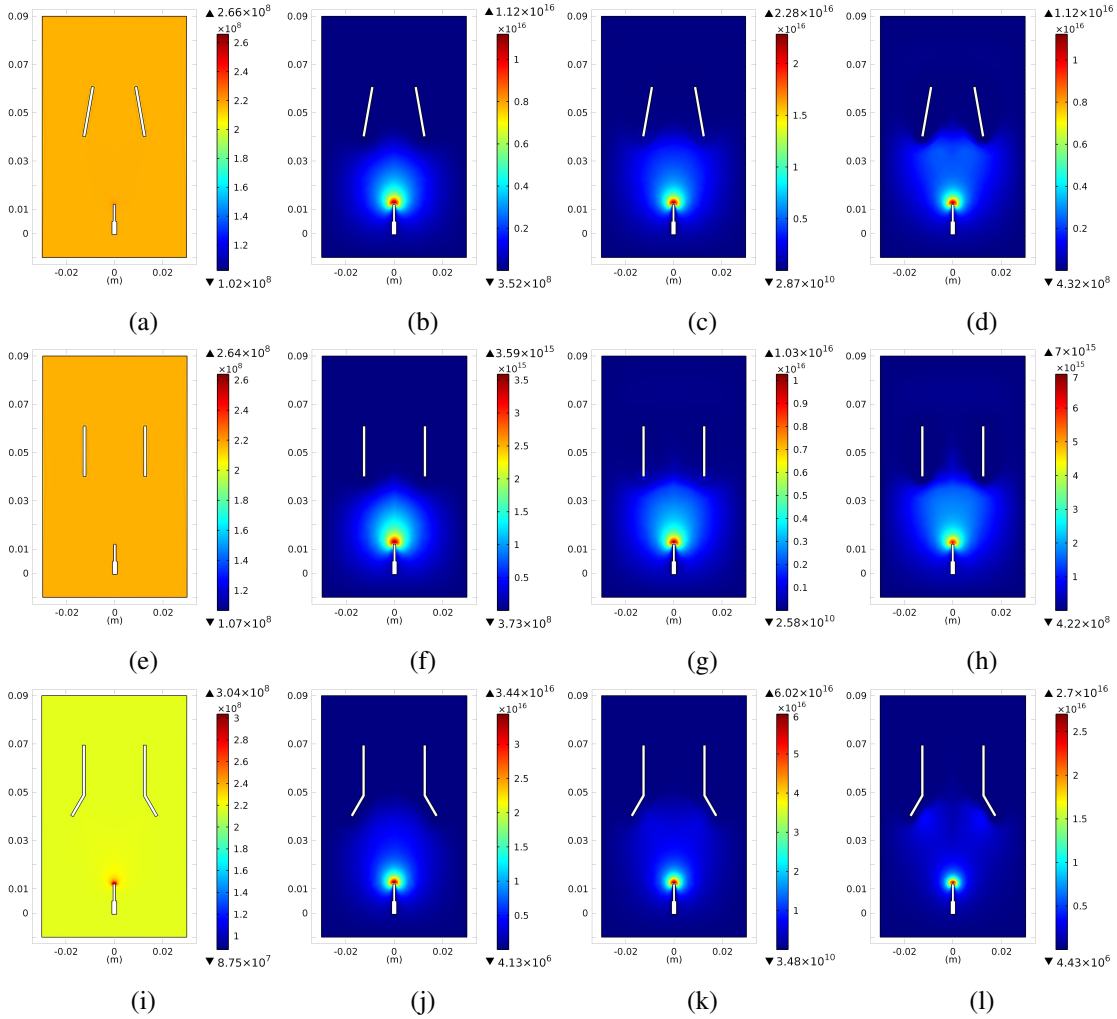

Figure 5.2: Spatial distributions of ion density (m^{-3}), for (a, e, i) O^+, (b, f, j) O^-, (c, g, k) O_2^+ and (d, h, l) O_2^- ions on cone (top row), cylindrical (center row) and funnel (bottom row) cathodes. $T_g = 300$ K and $p = 10$ Torr.

and until the entrance of the cathodic chamber which is driven by the arrangement of equipotential lines, as detailed in the section 5.2.

With the conical cathode configuration Figures 5.1a-5.1c, the electron density peak for the nitrogen gas discharge (1.7×10^{13} m^{-3}) is always higher than its equivalent discharges of argon (2.9×10^{12} m^{-3}) and oxygen (1.7×10^{12} m^{-3}) since they are quickly attached. An analogous pattern is obtained in the cases of the cylindrical and funnel-like cathodes (Figures 5.1d-5.1i).

In Figures 5.1c, 5.1f and 5.1i, it is also noticeable the high electron diffusivity in oxygen, spreading from the anode to the edge of the cathode wall. This is due to the ionization and electron detachment from O_2^- inside a conical region of the thruster. For oxygen gas, the particular tendency shown is for electrons to accumulate near the tip of the anode, extending towards the cathode in a "V" shape. This is due to the negatively charged oxygen atoms/molecules moving to the anode (tip) where they release electrons by electron detachment reactions.

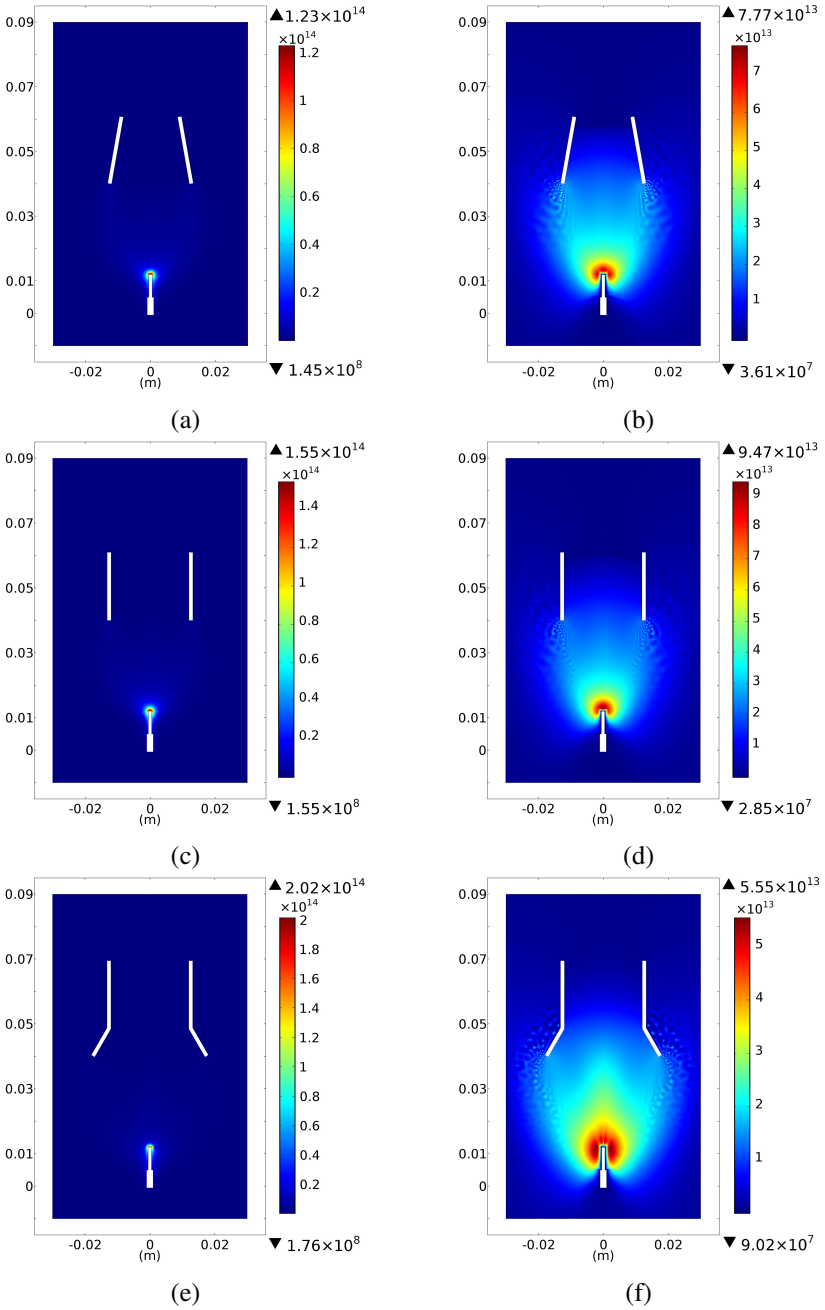

Figure 5.3: Spatial distributions of ion density (m^{-3}), for (a, c, e) Ar^+, and (b, d, f) Ar_2^+ ions. $T_g = 300$ K and $p = 10$ Torr.

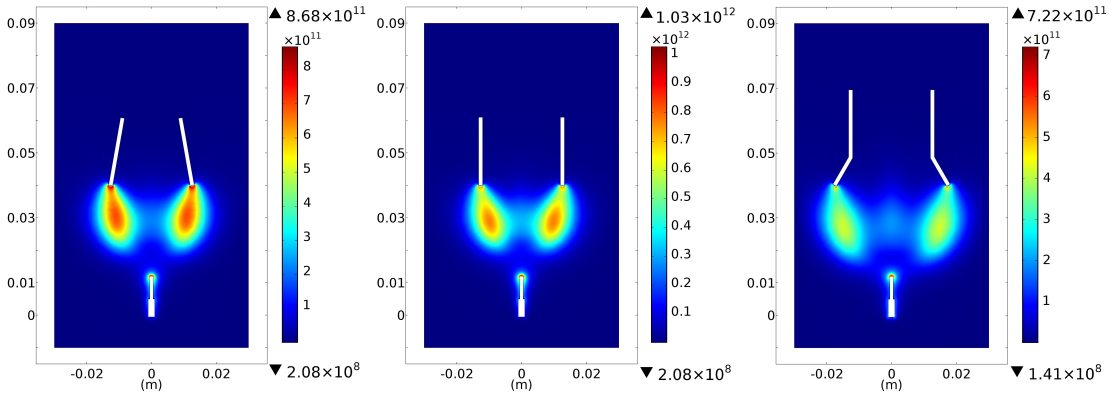

(a) (b) (c)

Figure 5.4: Spatial distributions of ion density (m^{-3}), for N_2^+ ions in (a) conical, (b) cylindrical and (c) funnel cathode. $T_g = 300$ K and $p = 10$ Torr.

Figure 5.2 depicts the ion density spatial distributions for all the considered ions in the discharges using oxygen, an electronegative gas, as the working gas (O^+, O^-, O_2^+ and O_2^-). We may notice again the tendency of the ions to allocate in the surroundings of the anode's tip forming a column towards the cathode, with the exception of residual O^+ ion, which distributes evenly through the space at a much lower density than the rest of the ions (typically eight orders of magnitude smaller), most probably due to the low injected power, not favoring a sufficient degree of dissociation. Regardless of the cathode configuration, the positive specie O_2^+ presents the highest ion density peaks: 2.3×10^{16} m^{-3} for conical, 1.0×10^{16} m^{-3} for cylindrical and 6.0×10^{16} m^{-3} for funnel cathode geometry. Although O_2^+ ion is the most abundant specie, the electronegative O^- and O_2^- ions play an important role on the discharge and the distortion of the electric field, specially in the ionization region surrounding the anode's tip since these species are more effectively produced by electron attachment and ion conversion.

Figure 5.3 shows the ion densities of the Ar^+ and Ar_2^+ ions for the three cathode geometries. The positive Ar^+ concentration peaks near the tip of the anode showing that it is the region where it is mainly created by migration due to electron impact. The Ar_2^+ is equally produced mostly near the anode's tip but they are also produced in a larger region towards the cathode due to the reaction $Ar^+ + 2Ar \rightarrow Ar_2^+ + Ar$, the three-body collision as described by Phelps and Brown (1952). The set of sub-figures that constitute Figure 5.3 shows the smooth distribution of positive ions charge carriers generated primarily near the electrodes and then carried into the main discharge volume by drifting motion in the electric field.

In Figure 5.4 we show that the nitrogen N_2^+ ions present a clear spatial distribution tendency amongst the three cathode configurations considered. These behavior results of a trade between the different electric potential spatial distribution and diffusion, according to the drift-diffusion mechanism.

Figure 5.5 shows the space charge density distribution for nitrogen discharges on the three cathode geometries considered. The space charge density of the nitrogen gas is defined as the

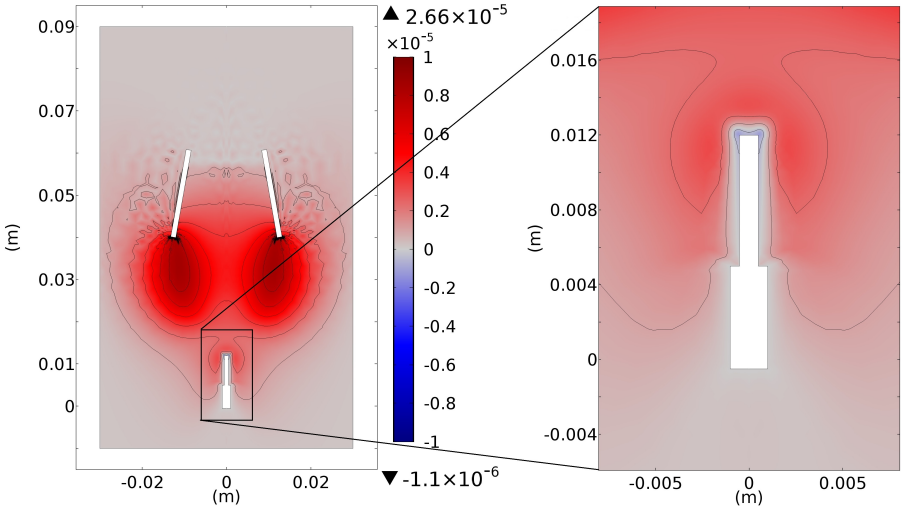

(a)

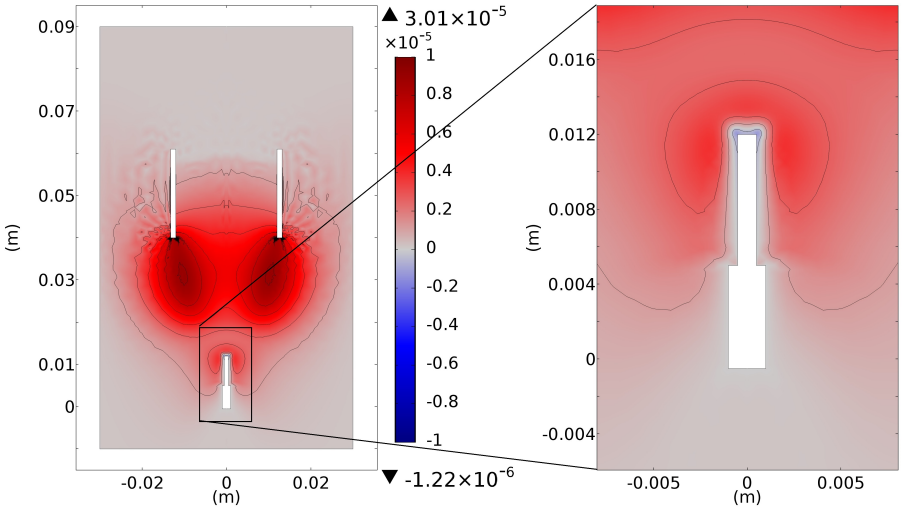

(b)

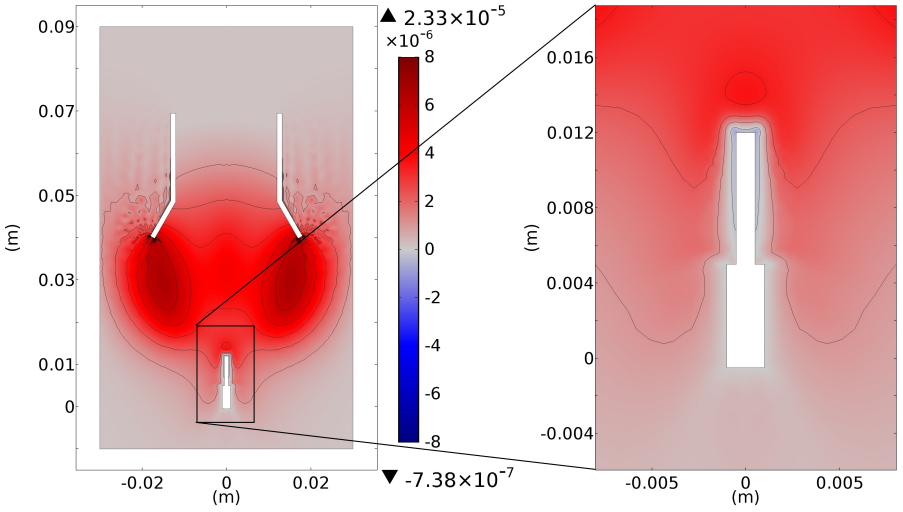

(c)

Figure 5.5: Space charge density distributions (Cm^{-3}), for nitrogen discharges on three cathode geometries. $T_g = 300$ K and $p = 10$ Torr.

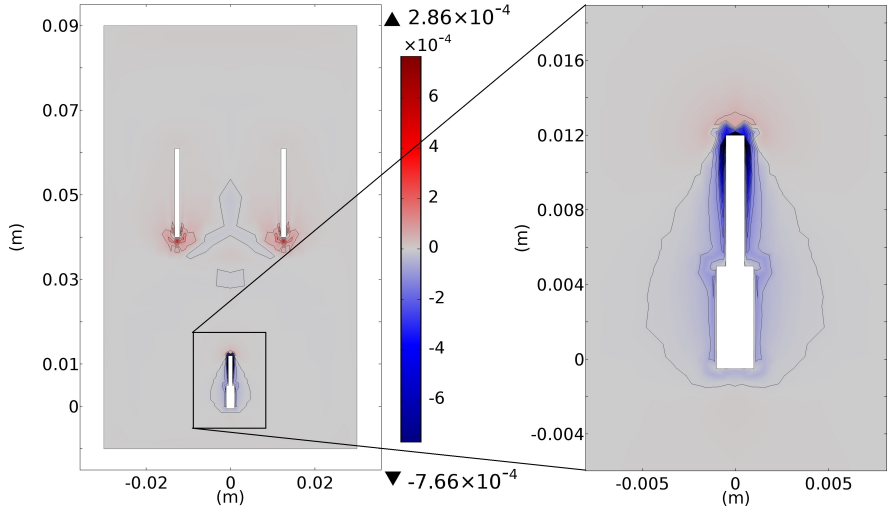

Figure 5.6: Spacial distribution of space charge density (C.m^{-3}) for oxygen discharge on the cylindrical geometry (left side). For a better overview we show a zoom of the charge density near the tip of the anode on the right side. $T_g = 300$ K and $p = 10$ Torr.

balance between ions and electron densities

$$\rho_{c,nitrogen} = e\left([N^+] + [N_2^+] + [N_4^+] - n_e\right) \tag{5.1}$$

As can be seen, the plasma has a low charge density with a modulus below $\sim 10^{-5}$ C.m^{-3}, which means that it is quase-neutral. The low charge concentrations are expected and they build up the space-charge field via the Gauss local equation, $\nabla \cdot \mathbf{E} = \rho_c/\varepsilon_0$. Near the electrodes the distribution magnitude clearly changes from the quase-neutral background, contributing to the space charge field that creates the cathode fall and the anode fall. As an example, using a cylindrical cathode (Figure 5.5b), the charge density changes between a negative values of $\sim$ -1$\times 10^{-6}$ C.m^{-3} near the anode tip and $\sim$+3$\times 10^{-5}$ C.m^{-3} near the cathode entrance. There is a strong field distortion near the anode but inside a limited volume enclosed by the ionization region. The negative values of the space charge density are exclusively situated around the tip of the anode as seen in the zoomed areas on the right side of Figure 5.5. In the region between electrodes the charge density is low but positive due to a large number of positive ions over electrons . We may also notice the zero value at the regions away from the electrodes.

We should point out the different behavior between positive nitrogen and electronegative oxygen gas comparing the distribution of ions (Figures 5.2 and 5.4). In particular, oxygen ions tend to be strongly created and destroyed in the antechamber of the thruster duct (Figure 5.2), thus creating an appropriate electric potential, favoring a convenient slope for the charge particle acceleration and for an efficient momentum transfer to the neutrals (see Figure 5.7 in section III-B).

Figure 5.6, which again considers the cylindrical cathode configuration, shows the spatial distribution of oxygen space charge.

$$\rho_{c,oxygen} = e\left([O^+] + [O_2^+] - ([O^-] + [O_2^-] + n_e)\right) \tag{5.2}$$

where $[O^+]$ and $[O_2^+]$ represent the concentration of oxygen positive ions and $[O^-]$ and $[O_2^-]$ the concentrations of oxygen negative ions, while n_e denotes the electron density. Again, the most negative region is around the tip of the anode.

We verify an increase of the charge density relative to the nitrogen case (about one order of magnitude) resulting from radial constriction phenomenon of the electronegative gas, which takes the positive ions to concentrate in the proximity of the cathode, while confining the negative charges in the cathodic chamber, stratifying the discharge (see Lieberman and Lichtenberg (2005) for more on the topic).

Let us now compare the Figures 5.1f (electron density spatial distribution) and 5.6 (space charge density spatial distribution), both for oxygen gas and a cylindrical cathode, we may notice an extended distribution of the electrons between the anode and cathode in the electron density, which favors the creation of positive ions on the edge of the plasma, as seen by the positive values of space charge density near the cathode edges, meanwhile the negative ions move towards the core of the plasma, not being lost to the walls of the cathode, confined instead by the space charge field created in that region.

5.2 Electric potential distributions

Figure 5.7 displays the electric potential spatial distributions for all studied cases. The anode, at the bottom of each figure, has the onset potential, which is the electric potential from the output of the RC-series circuit to avoid the arc regime between electrodes. The onset potential depends on the working gas and distance between electrodes, as these two parameters influence the equivalent impedance in the discharge region.

The increase of plasma thrust due to electrostatic pressure in the formed sheaths near the wall do not contribute to momentum, but it is rather the potential distribution inside the thruster reaction chamber the important parameter. However, the appropriate location of the plasma sheaths near the walls can favor the formation of the potential slope along which ions flow. These conditions of a potential slope extending to the outlet are clearly favorable to the ions acceleration and, therefore, the more efficient transfer of their momentum to the neutrals.

Since ions and electrons gain kinetic energy at the expense of electric potential, Figure 5.7 also illustrates the importance of an appropriate distance of acceleration (distance from the anode to cathode interior, where potential drops) of about 4 cm in our specific thruster design, which are satisfied for oxygen gas (c), (f), and (i); for argon and nitrogen the distance seems smaller reducing the acceleration region inside the cathode chamber. More attention will be given to the distance between electrodes and their potential drop in our next study about thruster efficiency.

The thruster tends to form a potential plateau inside the chamber. The equipotential lines distribution is such that the electric field is radially predominant and constitutes a less-than-ideal case for accelerating the ions in the axial direction (see the black arrows representing the electric field in Figure 5.7). For argon and nitrogen as working gases, Figure 5.7 shows a decay of the electric potential at the entrance of the cathode chamber even if in nitrogen this plateau extends

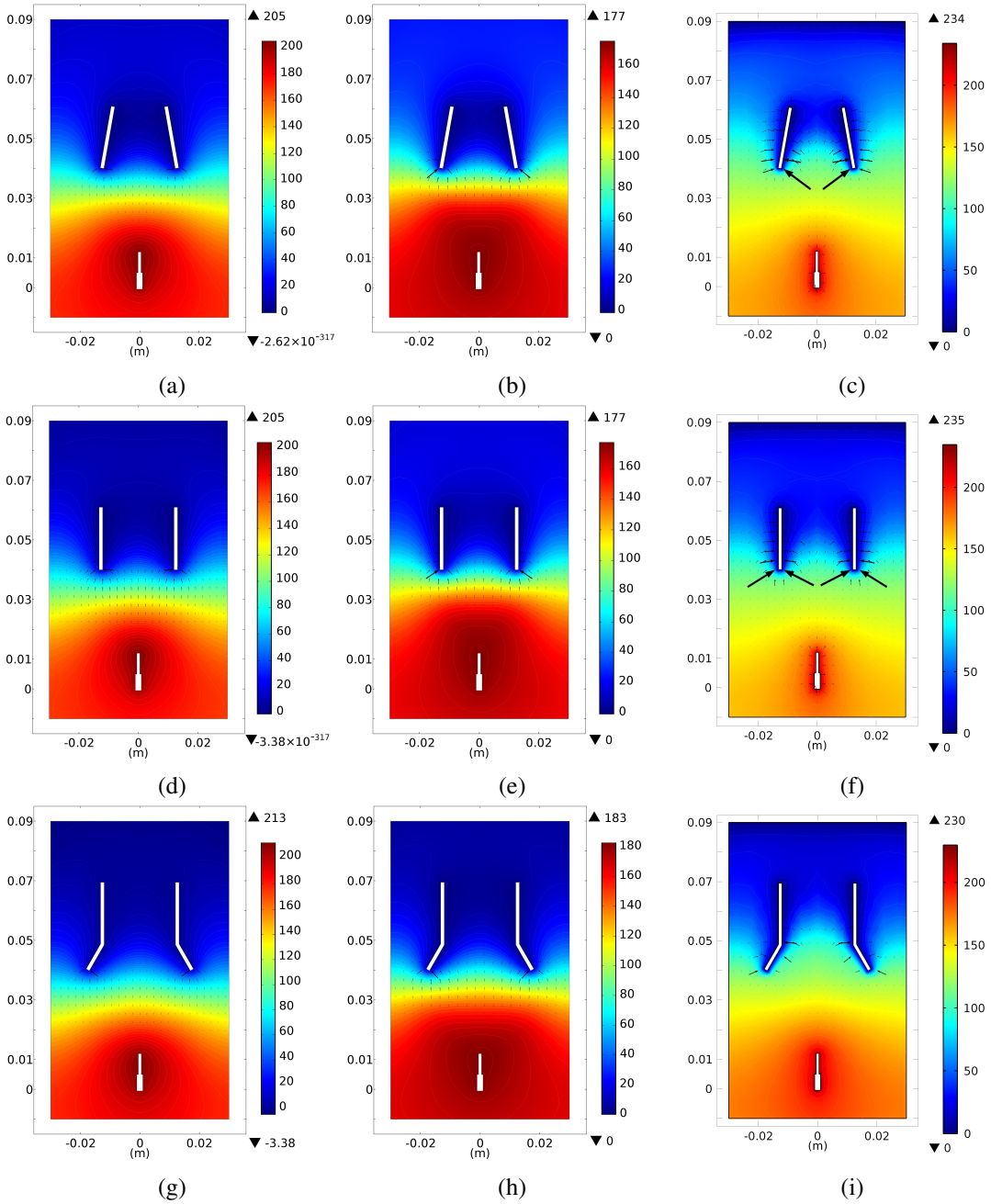

Figure 5.7: Spatial distributions of electric potential (V), for (a, d, g) argon, (b, e, h) nitrogen and (c, f, i) oxygen gases. Black arrows are proportional to the electric field. $T_g = 300$ K and $p = 10$ Torr.

Table 5.2: Net thrust, discharge power and thrust-to-power ratio produced by EHD thrusters on three cathode configurations using different gases at pressure $p = 10$ Torr.

Cathode configuration	Gas	Thrust, T (nN)	Power, P (mW)	T/P ratio (μN/W)
Conical	Ar	1.8	0.23	8.1
	N_2	4.51	0.50	9.03
	O_2	53.7	0.26	206.6
Cylindrical	Ar	4.1	0.23	18.0
	N_2	10.9	0.50	21.8
	O_2	89.0	0.13	685.6
Funnel	Ar	2.8	0.24	11.9
	N_2	5.5	0.51	10.7
	O_2	107.1	0.64	168.4

longer than for argon discharge. This is different from the oxygen gas where we can see that the electric potential drops well inside the chamber, resulting in a higher radial electric field. In consequence, the thrust in oxygen is well above the other studied gases (see Table 5.2).

5.3 Velocity distributions

Figures 5.8 and 5.9 show, respectively, the velocity magnitude of the fluid across the space and the three components of the velocity (total, axial and radial) relative to the electrode reference frame, at the cut line of each thruster's output.

In both Figures 5.8 and 5.9, the oxygen gas exhibit the longest axial and radial (towards the central axis) velocities. Incidentally we may notice that the axial profile is approximately parabolic in argon and nitrogen while in oxygen it presents a more pointy shape. As can be sen in Figure 5.8, the axial flow velocity in oxygen is about 15 cm/s while in the other two gases it does not exceed 5 cm/s.

5.4 Thrust production

Table 5.2 shows the net thrust produced by our EHD thrusters on the three cathode configurations and using the three different gases at the pressure of 10 Torr.

Figure 5.10 allows to compare the thrust production in the three cathode geometries for two values of pressure: 0.5 Torr (from Granados et al. (2016) and Chapter 4 of this thesis). With the conical cathode, thrust increases with pressure for the three gases, with the biggest change of about three orders of magnitude when oxygen is used. We can see the working gases at different pressures as series connected by lines in order to follow the net produced thrust for each cathode geometry. Notice that the three highest series are the gases with the highest pressures so the

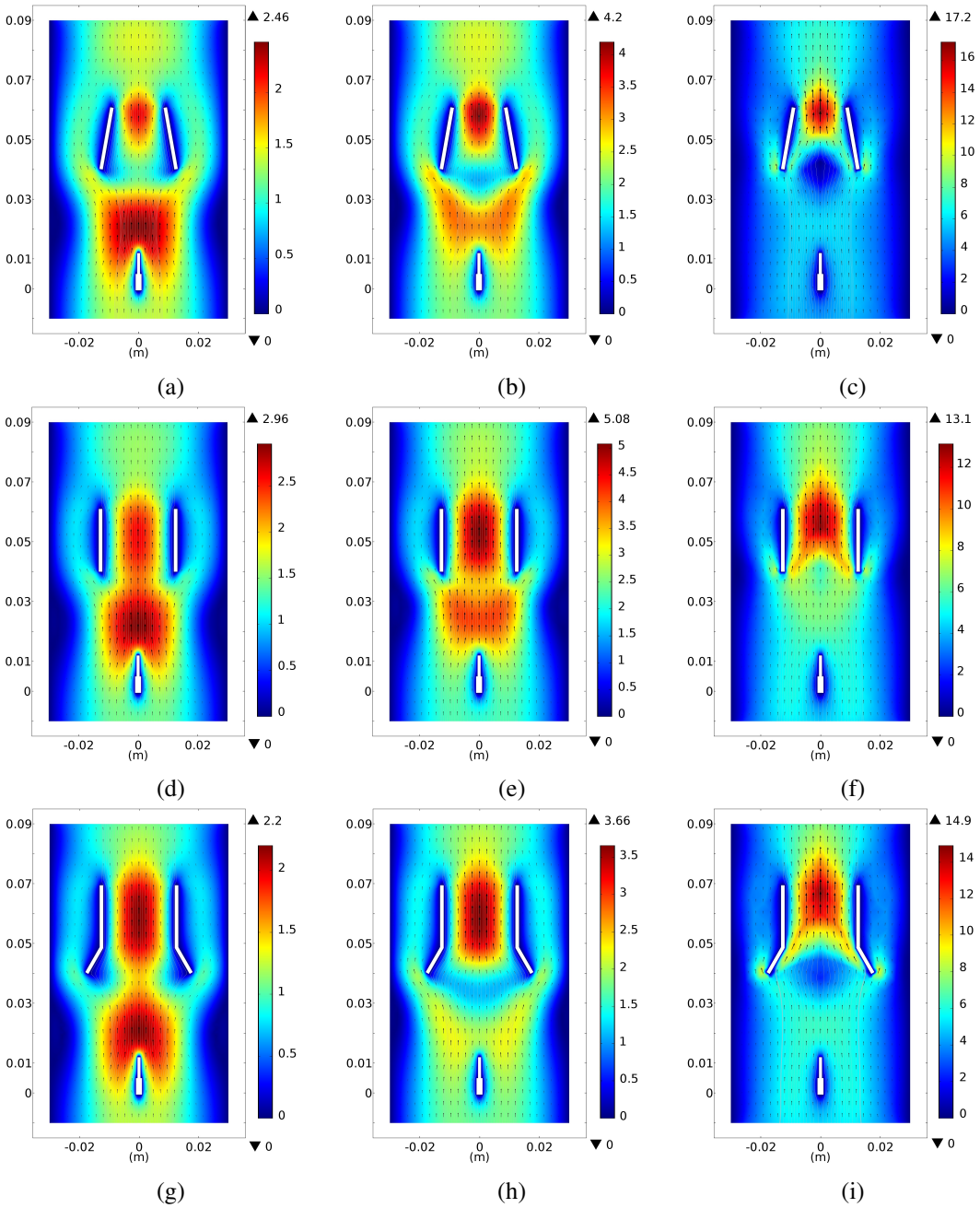

Figure 5.8: Spatial distributions of fluid velocity (cm/s), for (a, d, g) argon, (b, e, h) nitrogen and (c, f, i) oxygen gases. $T_g = 300$ K and $p = 10$ Torr.

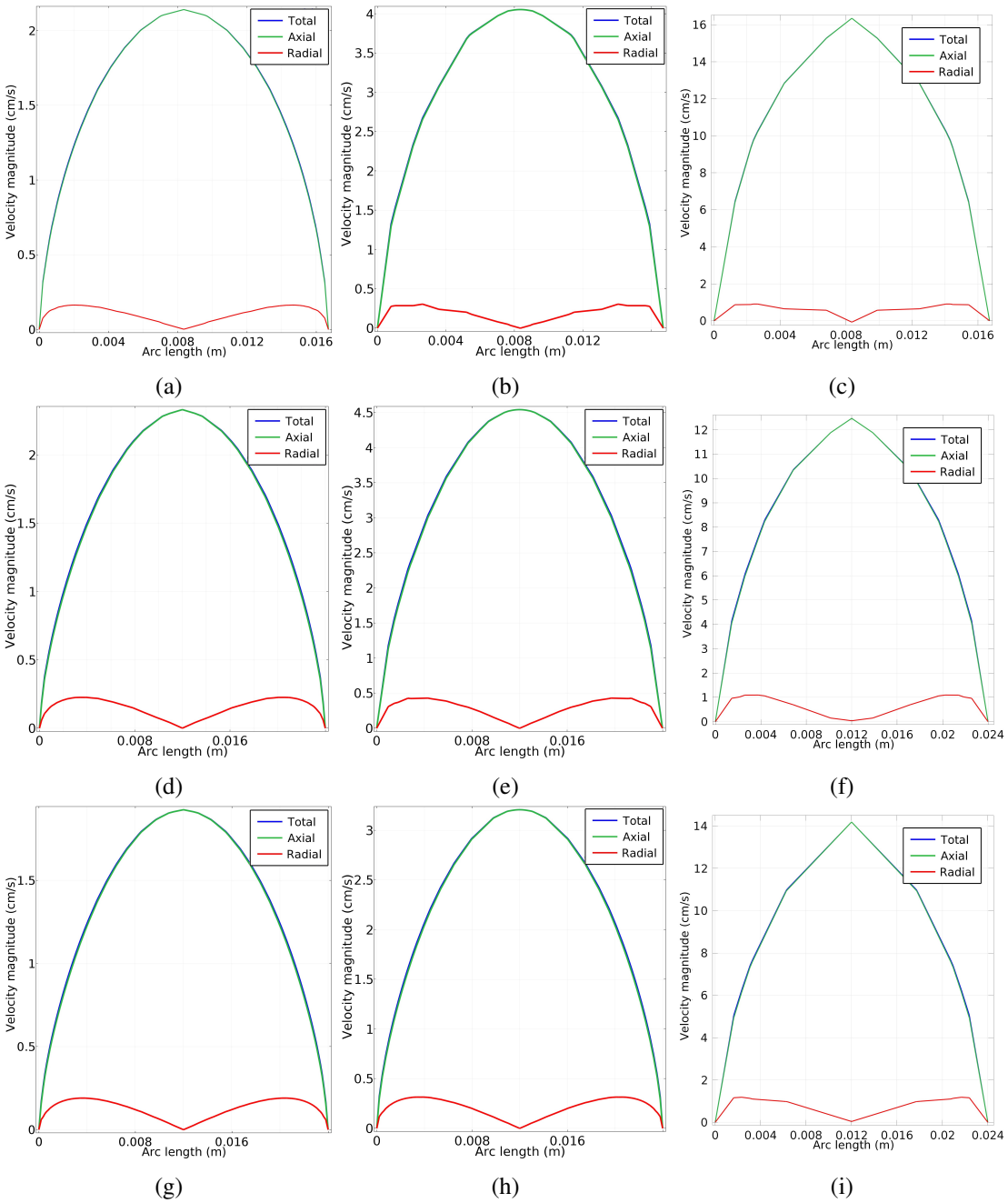

Figure 5.9: Fluid velocity components (blue:total; green:axial; red:radial) at output (cm/s), for (a, d, g) argon, (b, e, h) nitrogen and (c, f, i) oxygen gases. $T_g = 300$ K and $p = 10$ Torr.

increase of pressure from 0.5 Torr to 10 Torr increases several orders of magnitude the net thrust for most cases, being oxygen the gas with the biggest increase.

With cylindrical and funnel cathodes, argon and oxygen also increases about 2-3 orders of magnitude when pressure increases 20 times but in the case of nitrogen this increase is much less pronounced. Figure 5.10 shows that conical cathodes have, in general, the less favorable T/P ratio.

As can be seen on Figures 5.1c, 5.1f and 5.1i, oxygen gas, regardless of the cathode geometry, tends to form an extensive region where electrons are scattered comparing to the other gases that showed a more compacted spatial concentration of electrons, which seems well correlated with higher volume of regions where ohmic heating is intensified (i.e., region with higher electron density).

At the pressure of 10 Torr, the highest T/P is obtained for the highest axial speed, when steep radial velocities and gas flow near the walls were observed. Presumably, the inclusion of the gas temperature equation in our model, would modify the present conclusion, since the flow near the walls, with colder neutral species, would contribute less to ionization and reduce its contribution to thrust.

The funnel cathode geometry using oxygen gas presents the highest net thrust (107.1 nN) from the studied cases, even when this configuration does not present the highest peak velocity (see Figure 5.8). The latter is due to the fact that the case with higher peak velocities (Figure 5.8c) has a smaller chamber size and thus, a smaller volume of gas passing through the chamber.

The highest values of thrust and thrust-to-power ratio are obtained using oxygen as the propellant gas in all three of the studied cathode configurations. For example, when comparing gases in the cylindrical cathode geometry we found a T/P ratio for oxygen of about 690 μN/W while the argon T/P ratio is below 20μN/W.

According to Granados et al. (2017a), since the ballast resistance was the same among cathode geometries, the net thrust values are nearly of the same order of magnitude for the same gas, although they do not represent the optimized result for each gas used. Results for a specific cathode configuration over different values of the ballast resistance will determine how much thrust can a geometry/gas pair produce.

Since we assume a homogeneous, constant gas temperature where the ions have the same temperature as the neutral gas ($T_{ions} = T_g$), we do not consider the ions velocity distribution, which, presumably would lower the thrust efficiency since it would consider the energy losses caused by the wide spread of ions in velocities and the presence of transversal and axial ions. However, we don't expect highly accelerate beam of ions toward the walls since the applied voltage is about 200 V and the plasma potential gradients are not enough to give ions significant acceleration and for this reason we opted for a less cumbersome model aiming to understand the major characteristics of the EHD thruster without losing sight of the future task of building a more complete simulation.

In summary, at a pressure of 10 Torr, argon has the lowest thrust and thrust-to-power ratio values of the three gases and the three cathode geometries under study; nitrogen seems a tiny better than argon but, clearly oxygen has the highest thrust and T/P ratio, which is a consequence of a favorable drop of electric potential in a more extended region entering inside the chamber,

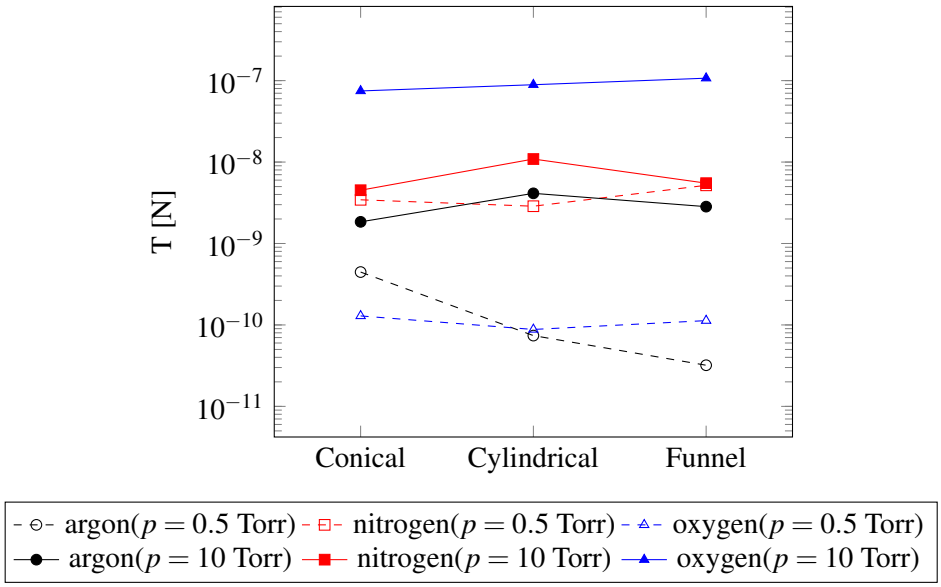

Figure 5.10: Thrust production comparison for three cathode geometries (conical, cylindrical and funel) and two pressure values (0.5 Torr and 10 Torr).

allowing a continuous negative ion acceleration (oxygen is electronegative) instead of a shorter acceleration path build-up for argon and nitrogen (we note that the acceleration region is shorter for nitrogen relative to argon). As the Coulomb force acts during a longer path on oxygen the momentum transfer is higher.

5.5 Conclusions

The present chapter shows the results of the modeling of single stage EHD thrusters with three different cathode configurations and using three different propellent gases at a working pressure of 1.3 kPa (10 Torr).

Additionally, we compare these results with the ones previously obtained with similar cathode configurations and with the same working gases but at the lower pressure of 67 Pa (0.5 Torr)(see Chapter 4).

At a pressure of 1.3 kPa (10 Torr), regardless of the cathode configuration, argon produces the worst values of net thrust and in most cases the worst thrust-to-power ratio (except with the funnel cathode where it slightly overpasses nitrogen), followed by nitrogen and oxygen in increasing performance order.

For argon and nitrogen as propellants, we found the cylindrical cathode to produce slightly better thrust and thrust-to-power ratio. A tendency broken by oxygen gas, performing better in the funnel cathode geometry. Additionally oxygen presented the highest values of thrust as well as T/P ratio amongst all the cathode geometries in this study.

In the 67 Pa (0.5 Torr) gas pressure scenario, nitrogen produced the best performance values, while in the 1.3 kPa (10 Torr) oxygen was the most promising working gas of the three considered.

In the case of oxygen (10 Torr), even though the conical cathode geometry presented the lowest thrust (53.7 nN) and the funnel cathode showed the highest (107.1 nN), the thrust-to-power ratio is slightly higher in the cylindrical case. Additionally the cylindrical cathode performed with a T/P ratio of about three times the value for the conical cathode geometry, making it the most efficient configuration to use with oxygen.

By means of this set of parametric studies we conclude that a convenient thruster inlet surface form is an important parameter in the thruster design since it provides the onset of more appropriate electric field for ionic acceleration. Since the geometry of the electrodes has such a strong impact on the performance of the thrusters, it is necessary to investigate in a carefully manner the optimization of the distance between the electrodes for each one of the three geometries employed and for each working gas, since the arrangement of the equipotential lines is key in forming a desired electric field that accelerates the ions towards the interior of the chamber in the axial direction.

On the next chapter it is investigated how the propulsion force varies with the pressure over a wider range of values as well as with the temperature of the gas, in order to understand its influence on the performance of the EHD thrusters.

Chapter 6

Electrohydrodynamic thrusters response to several simulation conditions in nitrogen gas

On this chapter we will investigate the role that the gas pressure, the gas temperature, the ballast resistant, the discharge current, the secondary electron emission, and the gap between electrodes play in the performance of the proposed two-dimensional EHD thruster model. Nitrogen as the working gas and the funnel-like cathode geometry are employed for the present analysis.

6.1 The influence of the gas pressure

Figure 6.1a shows in detail the pressure dependency of the thrust production, where an increase of several of orders of magnitudes is found when the gas pressure varied from 0.5 Torr to 20 Torr. As the pressure increases, so does the power spent on sustaining the discharge as seen in Figure 6.1b, which is expected, since the gas velocity and thrust both increase as well. The electric current flowing between electrodes diminishes for the increase in pressure, which leads to an increase in the onset potential due to loss of energy for collisions with heavy species, strengthening the electric field on the configuration, and improving the efficiency of the thruster as seen by the thrust-to-power (T/P) ratio on Figure 6.1c since an increasing volume of plasma feed the gas with ions able to transmit momentum to the neutrals. We may also notice on Figure 6.1d how the peak velocity magnitude increases with the pressure, although not as regularly as the rest of the considered parameters.

Figure 6.2 shows the natural logarithm of the electron density depicting how the electron cloud sets on the space between electrodes. For every case the peak of the electron cloud is located at the tip of the anode with the ionization region expanding with pressure. At 0.5 Torr, electrons tend to spread more regularly around the anode, an outcome of the corona effect favoring the increase of the area of the anode, but this mechanism diminishes in the other cases due to the increased velocity of the gas flowing around the anode, meaning a higher rate of collision with neutrals. For

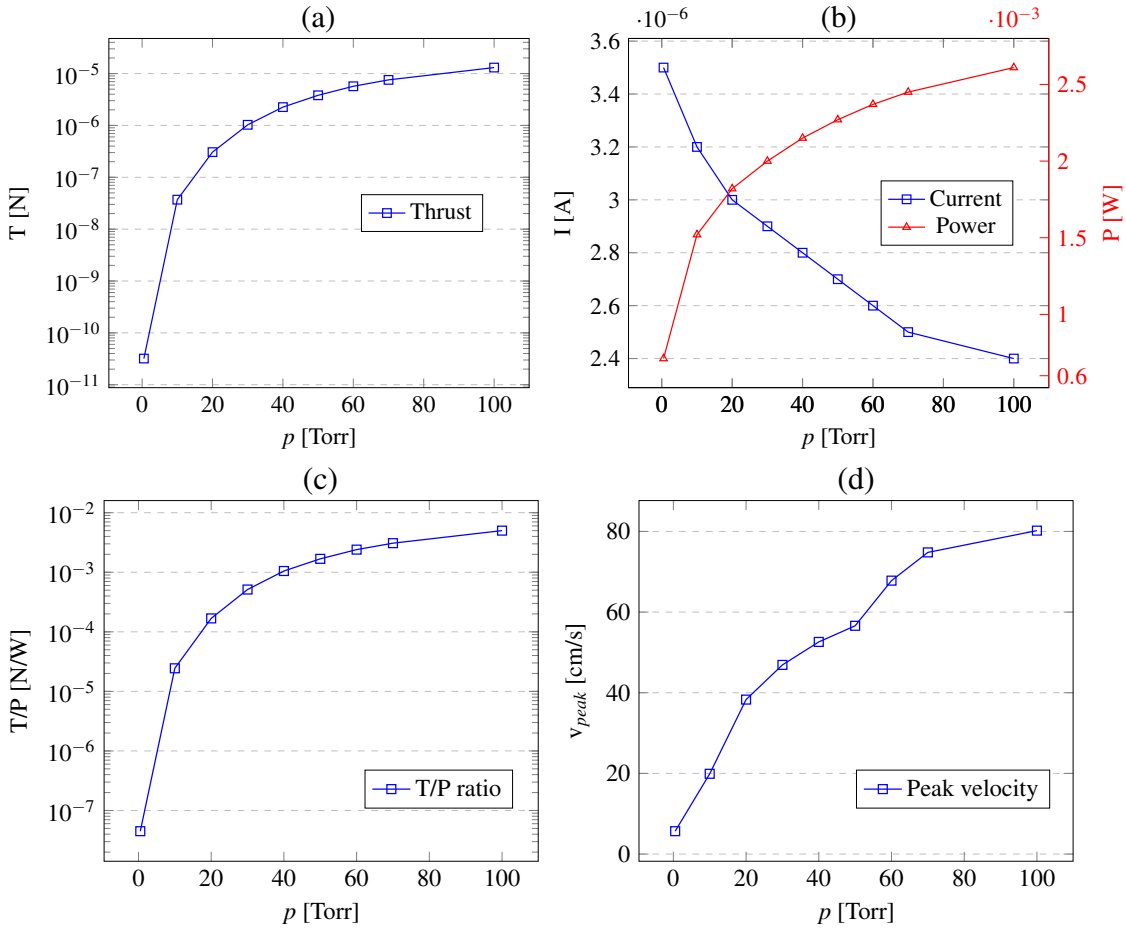

Figure 6.1: (a) Thrust, (b) current and power, (c) T/P ratio, and (d) peak velocity as functions of pressure, $T_g = 300$ K.

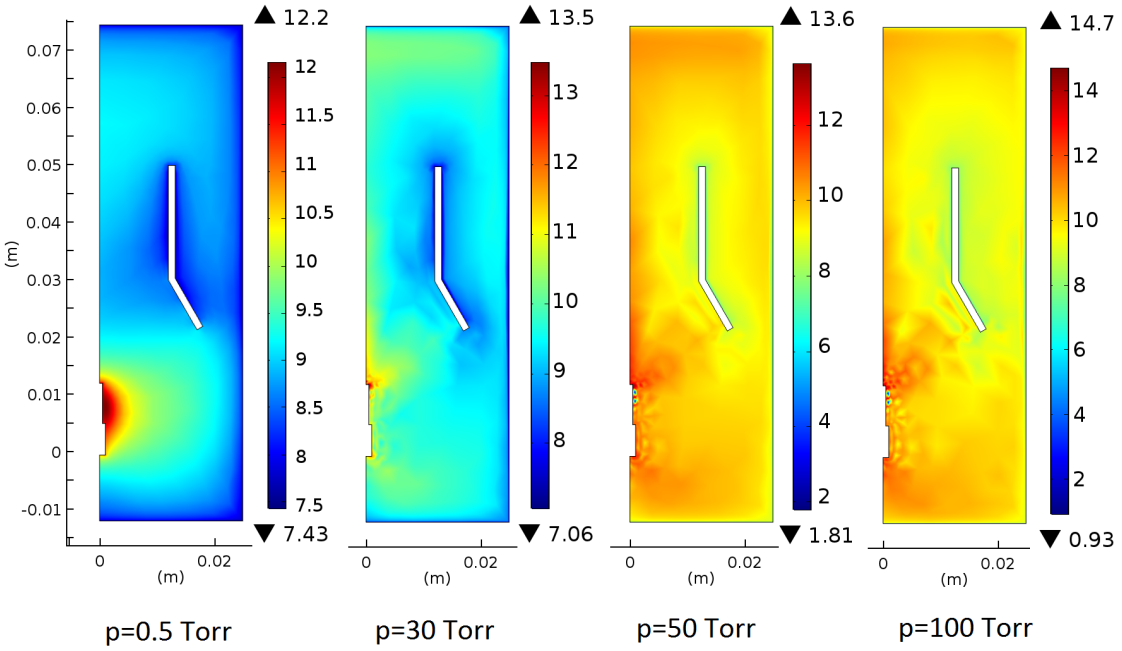

Figure 6.2: Log of electron density, $log_{10}(n_e)$, for several values of gas pressure, $T_g = 300$ K.

p= 30 Torr we notice the electron cloud tends towards the cathode's entrance and along the axis of symmetry, an electron behavior that reinforces with increasing gas pressure.

In Figure 6.3 we may see the gas velocity distribution of the thruster for a range of gas pressures. It is clear how the higher pressures have a directly proportional impact to the fluid velocity. The highest values of the velocity are all located at the tip of the anode. This is due to the increase of power (see Figure 6.1b) with pressure, leading to a higher volume of plasma and an increase of the electrons density. However, the rate of power increase is reduced by the loss of energy due to collision with heavy species, leading to a decrease of the current (Figure 6.1b).

The force acting on charged particles, in a simple approach, is proportional to the current density and inversely proportional to the ionic mobility. Hence, with increasing pressure the ions-neutrals collision frequency also increases and ionic mobility decreases; with current, thrust tends to increase.

6.2 The influence of the gas temperature

As the temperature of the gas ranged between 190 K and 400 K we notice a slight decrease in performance. Namely Figure 6.4 shows the decrease on the produced thrust, peak velocity and T/P ratio for a constant gas pressure of 10 Torr. Additionally, higher values of the gas temperature translate into less power delivered to the thruster with a higher current between electrodes since power loss varies as $\nu(T_e - T_g)$ (with ν the frequency of collision), which means a lower onset potential and consequently, a weaker electric field to accelerate charged particles between electrodes.

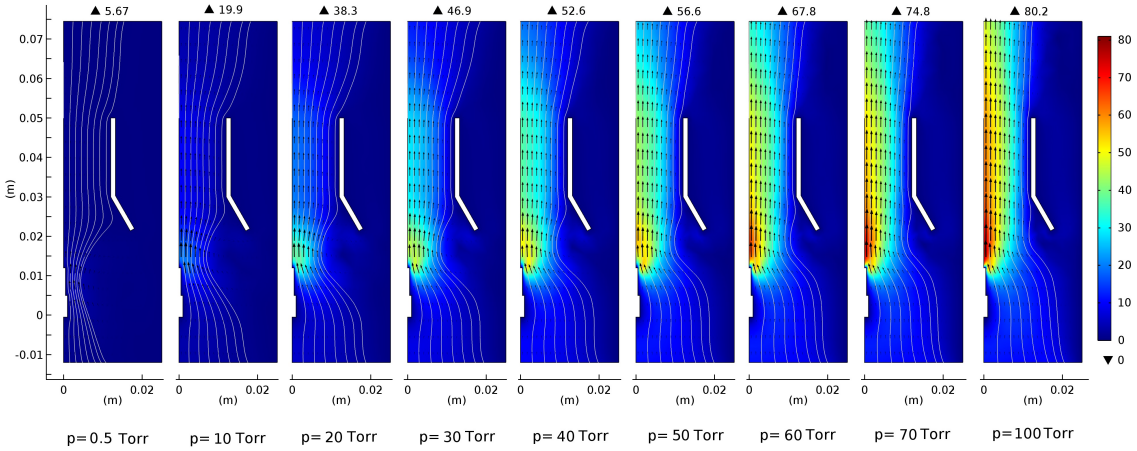

Figure 6.3: Velocity profile [cm/s] for several values of gas pressure, white lines indicate the flux lines crossing the chamber, black arrows are proportional to the velocity field (peak values on top), $T_g = 300$ K.

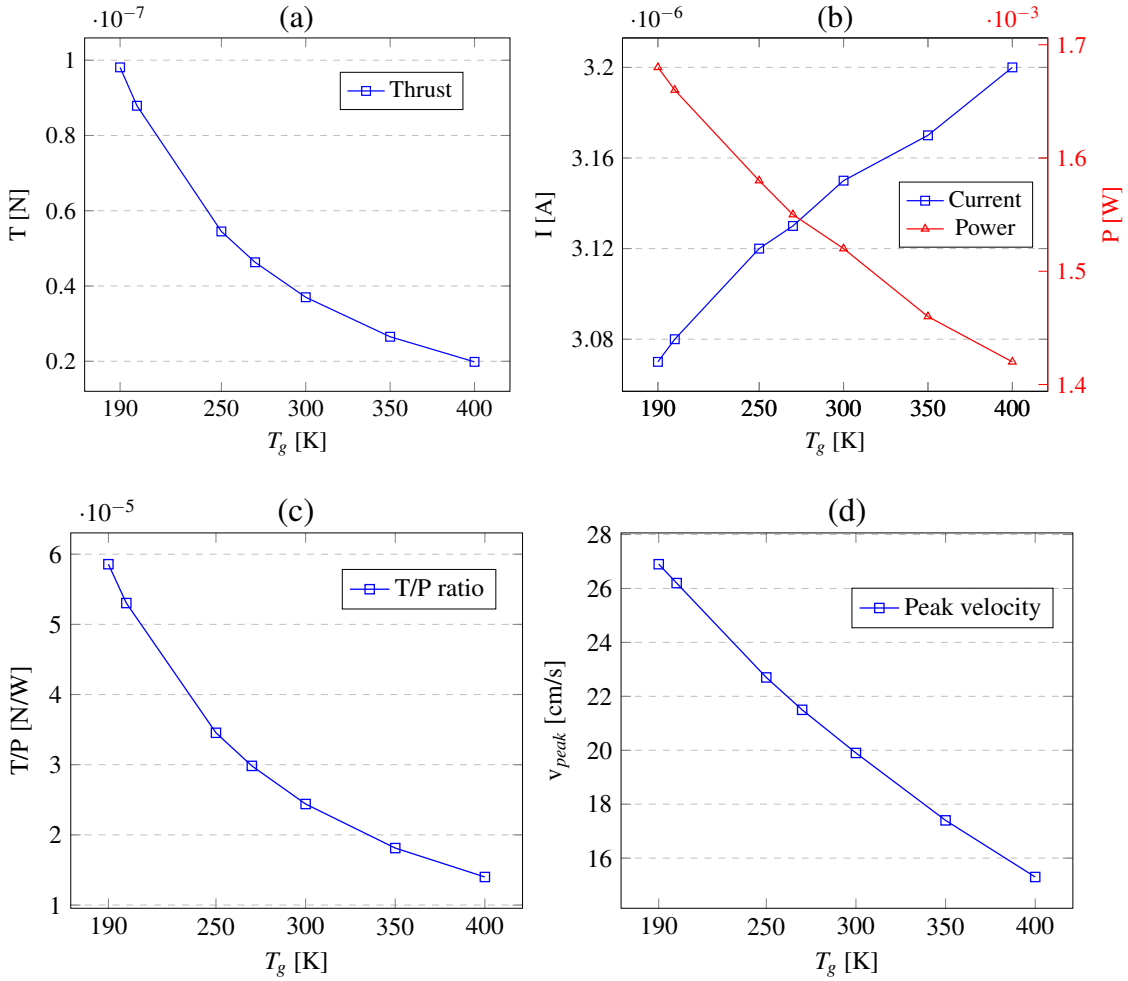

Figure 6.4: (a) Thrust, (b) current and power, (c) T/P ratio, and (d) peak velocity as functions of gas temperature, $p = 10$ Torr.

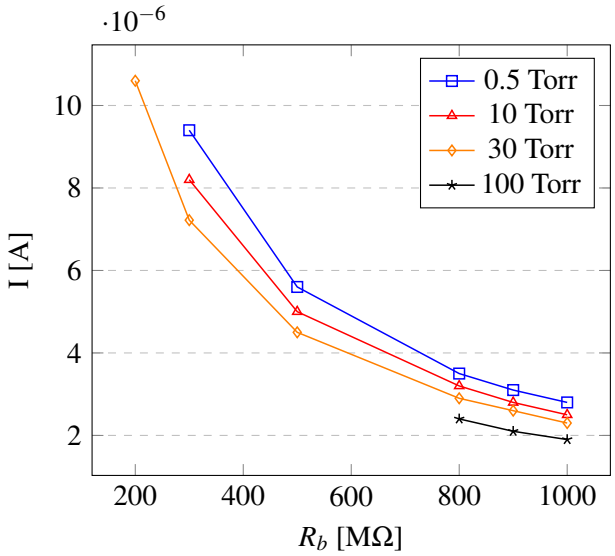

Figure 6.5: Current dependance on the ballast resistance, R_b, for several pressure values, $T_g = 300$ K.

The previous behavior may seem counter-intuitive since we may expect a hotter gas to flow faster through the nozzle, but we also need to consider that a hotter gas decreases the gas density for a fixed pressure, thus lowering the gas mass flow rate going inside the thruster's chamber. Young (2009) points to the same behavior regarding the influence of the gas temperature on the thrust and efficiency of the EHD thrusters.

Although an increase in the gas temperature lowers the performance of the thruster, it has less impact compared to the pressure variations, e.g. the thrust was reduced five times with the temperature (Figure 6.4a) but increased five orders of magnitude with the pressure (Figure 6.1a).

6.3 The influence of the ballast resistance and discharge current

We have seen in the pressure variation results that the produced thrust increased and the current decreased, same relation can be drawn in the case of the temperature variation, i.e. inverse proportionality. However according to Masuyama (2012) and Pekker and Young (2011), the delivered current is directly proportional to the produced thrust (for a fixed pressure and temperature) so we may not see this relation from the previous studies.

In order to see how current affects the thrust we modified the ballast resistance in order to obtain different steady-state discharge currents. The current will be controlled by modifying the ballast resistor and maintaining the input voltage in the RC-series circuit. We found that increasing the ballast resistance lowers the delivered current between electrodes as the input voltage, V_{in} stays unchanged, see Figure 6.5. The latter is expected since the total resistance seen from the voltage source will increase as well.

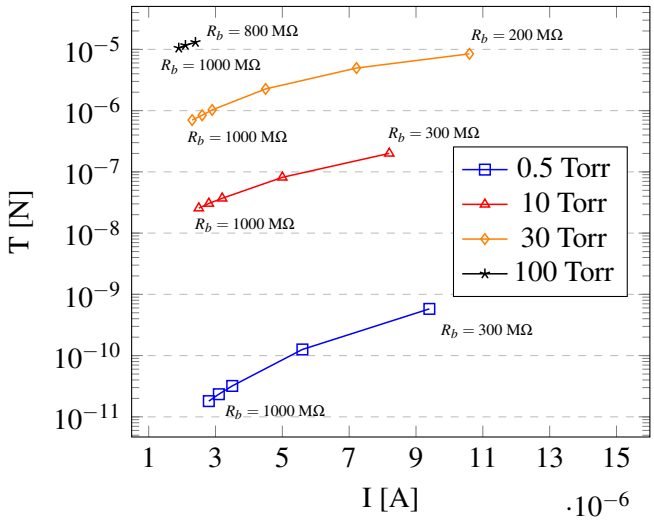

Figure 6.6: Thrust as a function of current for several pressure values. Various ballast resistance values needed to obtain the current are indicated near the points, $T_g = 300$ K.

On Figure 6.6 we may see the relation between the net produced thrust and the current flowing between electrodes for several gas pressures and we may now notice the direct impact of the current on the thrust. In the curves shown in this figure, the thrust increased about one order of magnitude when the current changes from its minimum to its maximum value considered. Although the change in current is relatively small, it took a wide range of ballast resistance to achieve it, i.e. [200-1000] MΩ. As expected from the previous analysis, the series with higher pressures produced higher thrust values for a given current between electrodes.

Due to the transitory nature of the discharge at the beginning of the simulation, we can not always decrease the ballast resistance until any desired value without creating a spike in the current and losing convergence of the time-dependent simulation. Such effect was noted in the series of $p = 100$ Torr of Figure 6.5 when no steady-state solution was found for ballast resistances lower than 800 MΩ.

We may infer that our methodology, searching for consistency among variables, allows direct comparison with Masuyama (2012) and Pekker and Young (2011).

6.4 The influence of the secondary electron emission coefficient, γ_i

We investigated the effect that the secondary electron emission from the cathode has over the discharge, which is of especial interest since the electrodes are not parallel and have different sizes. The electric field accelerate ions towards the cathode surface, which impinge on its surface. Ions with sufficient energy upon impact with the cathode will release electrons, commonly called secondary electrons, which in turn contribute to the total current between electrodes. According to Donkó (2001), the electron emission yield may vary considerably with discharge operating

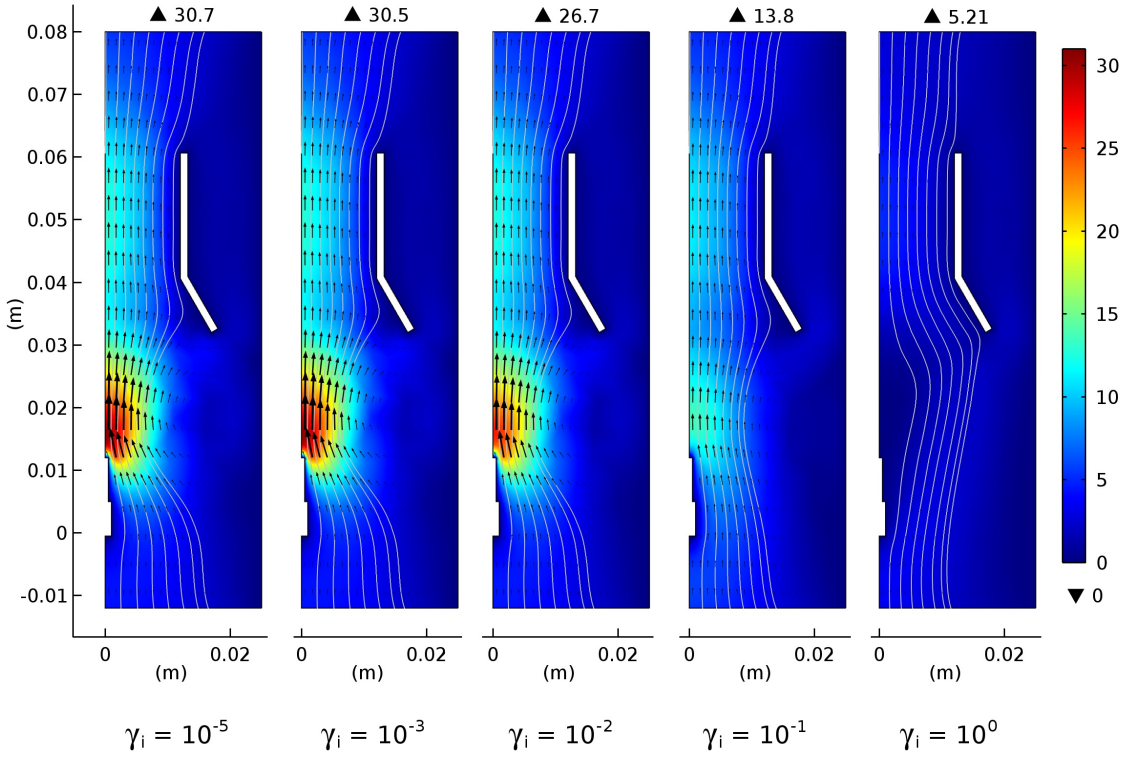

Figure 6.7: Velocity profile [cm/s] for several values of SEEC (peak values on top), $T_g = 300$ K and $p = 10$ Torr.

conditions, in particular with the reduced electric field E/N, which we calculate in each point of space over time. We expect to have a different solution from cases where E/N is a constant.

The secondary electron source induces the modification of the electric potential distribution, deviating the ionic flow to the boundaries, instead of the shortest trajectories to the end of the nozzle.

Figure 6.7 shows the thruster velocity profile for several values of the secondary electron emission coefficient, γ_i. We may notice the loss of fluid velocity for increasing values of γ_i, and the accumulation of stationary fluid near the anode's tip, the region typically presenting its highest value for the extreme case where $\gamma_i = 1$. The gas pressure and temperature were maintained constant at 10 Torr and 300 K, respectively.

In Figure 6.8 we may identify two regions presenting different behaviors for all considered parameters: i) $10^{-5} < \gamma_i < 10^{-2}$ where the thrust, current, power, T/P ratio and even peak velocity remain fairly indifferent to the change in the secondary electron yield, and ii) $10^{-2} < \gamma_i < 10^{0}$ where a clear decrease of thrust, power, T/P ratio and peak velocity may be observed due to an unfavorable distortion of streamlines, accompanied by an increase in the discharge current, an undesired effect for the purposes of thrust production since this effect is accompanied by a power loss. This case study may shed light on the appropriate choice of electrodes to improve the thrust.

As we may infer from the previous results, whenever we encounter with an increase in current and a decrease on the delivered power we notice a degradation of the thrust and T/P ratio, which

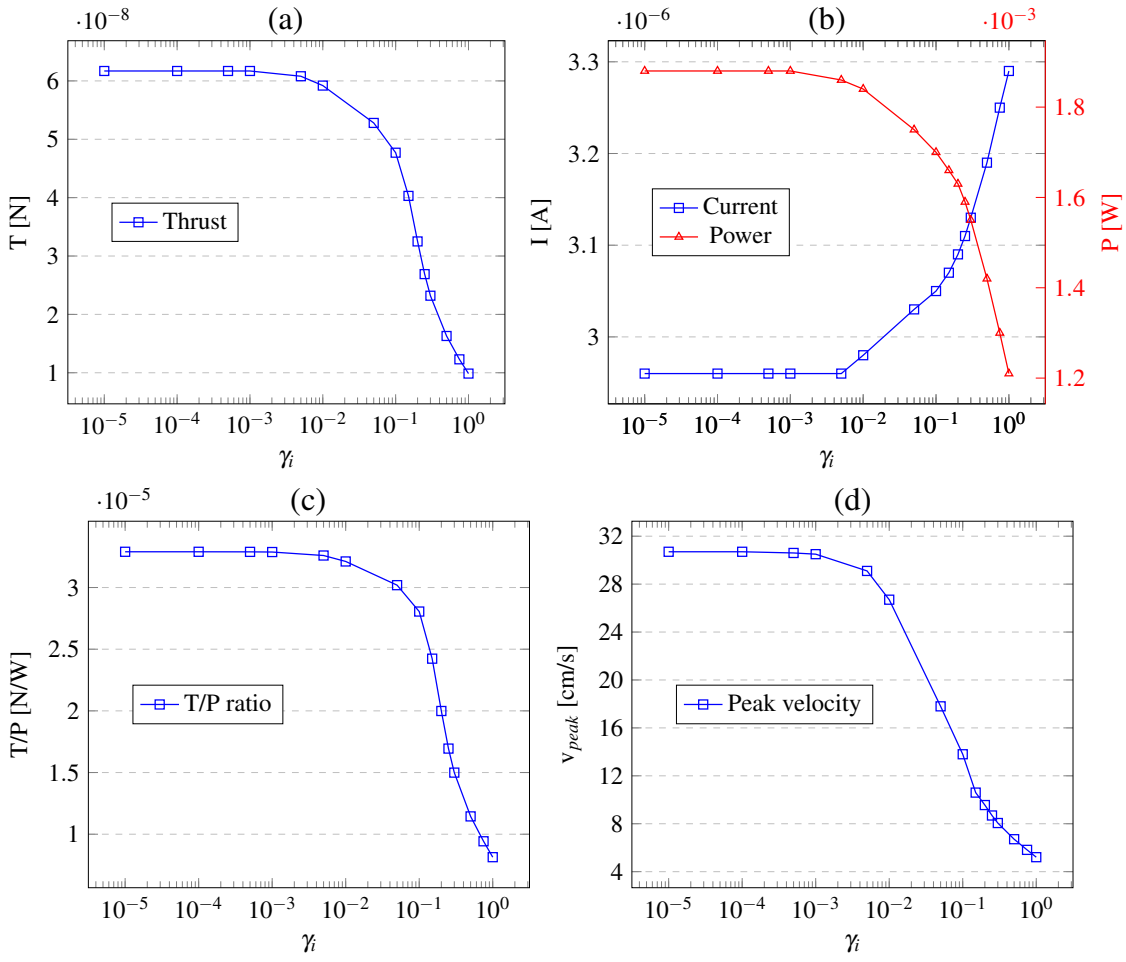

Figure 6.8: (a) Thrust, (b) current and power, (c) T/P ratio, and (d) peak velocity as functions of SEE coefficient, $T_g = 300$ K and $p = 10$ Torr.

occurs for values of $\gamma_i > 10^{-2}$. The secondary electron stream released from the cathode adds up to the total current between electrodes, so higher SEEC values will diminish the performance of the thruster. γ_i is a value that depends on both the impinging ions and the material of the cathode's surface, which must be considered when building the thrusters to avoid undesired operation region.

6.5 The influence of the gap between electrodes, d

An additional parameter with impact on the discharge profile response, is the distance between electrodes. Two sets of simulations were carried in this section, the first one employs a gas pressure of 0.5 Torr while the second one sets the pressure to 10 Torr. In each set of simulations the distance between electrodes was varied from 0 cm up to 10 cm. The thrust, current between electrodes, power of the discharge, thrust-to-power ratio and peak value of the velocity magnitude are presented and compared.

For a gas pressure of 0.5 Torr we may see the velocity spatial distribution on Figure 6.9, were we notice a higher value of the flow velocity magnitude around the anode for a gap between electrodes of 2 cm (7.36 cm/s) compared to the other cases with different gaps, where most of the them present peak values of less than 3 cm/s. While the velocity magnitude around the anode diminishes after the gap of 4 cm, the velocity inside the chamber increases and becomes closer to the highest value of its spatial distribution.

Figure 6.10 presents the performance values of the plasma discharge for several values of the gap between electrodes, d, for a gas pressure of 0.5 Torr. We notice that the total thrust is increasing as the gap increases as well as the power that sustains the discharge. On the other hand, the current between electrodes slightly lowers, which in turn implies that the onset potential between electrodes is increasing proportional to the the distance between electrodes, strengthening the electric field, which explains the tendency of the produced thrust to rise.

For a gas pressure of 10 Torr we found that the flow speed increases with gap distance, even when the velocity around the anode gets diminished. As illustrated on Figure 6.11, with increasing gap, the highest speeds tend to occur near the cathode. This is due to the increase of the reduced electric field and deposited power that favors the formation of streamers which tends to increase in length and number with the applied voltage and gap distance.

The net produced thrust increases with the electrodes's gap for the considered values, as seen on Figure 6.12a. Since the input voltage, V_{in}, is higher than the onset potential of the anode due to the voltage drop on the ballast resistance, when the distance between electrodes increases so will the total plasma resistance. This effect, therefore, decreases the electric current flowing between electrodes but strengthens the onset potential and with it the electric field. The combination of those factors driving thrust explains the thrust increase, even when the current decays.

There is, presumably, a gap value at which the electric field becomes weak enough so that this tendency breaks down; such distance must lower the current until the voltage between electrodes becomes close to the input voltage, and after that, the electric field should start decreasing its strength because the potential will not grow any longer as the distance will. This presumed gap

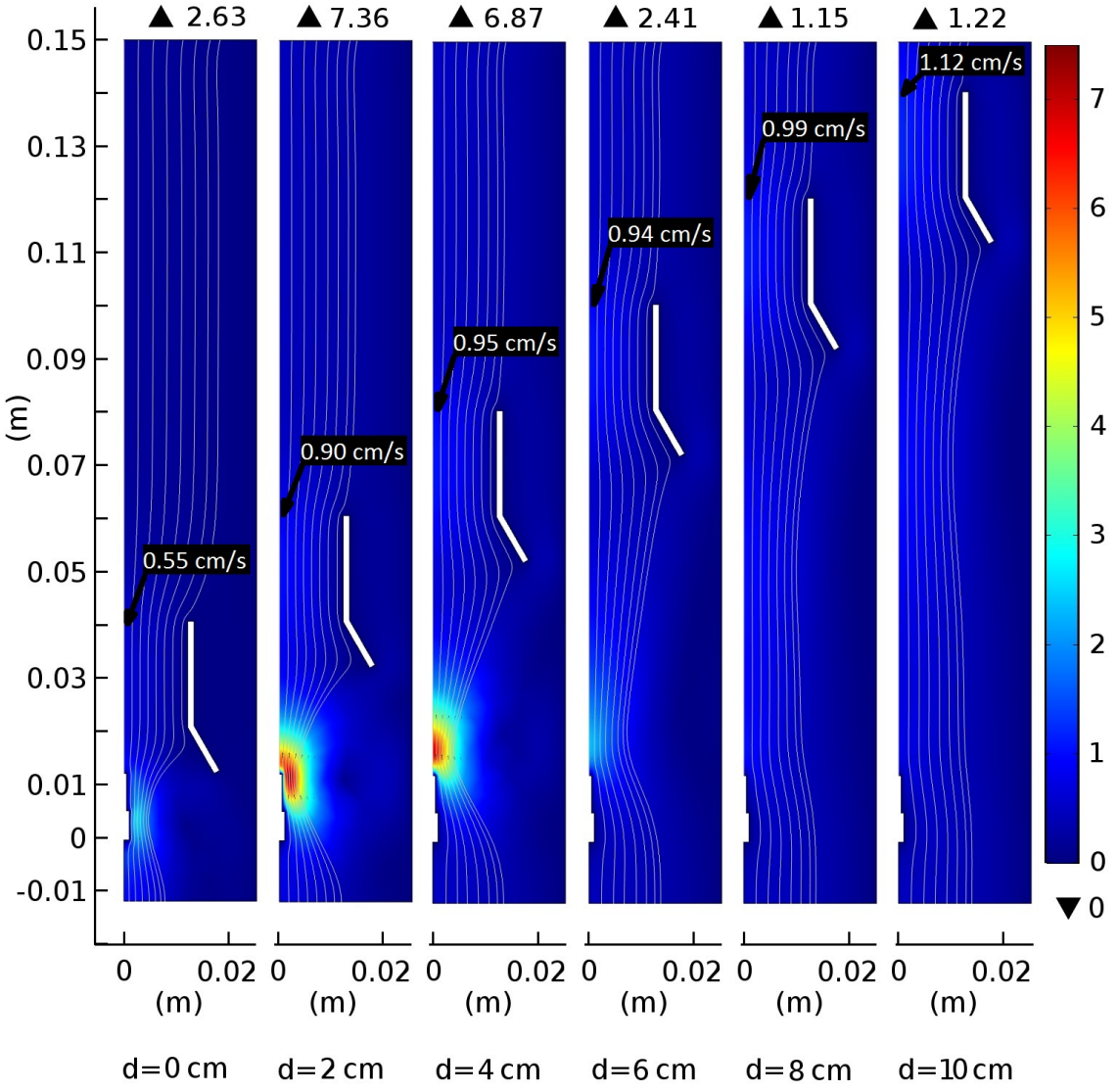

Figure 6.9: Velocity profile [cm/s] (peak values on top) for several values of gap between electrodes. Values in center line of chamber's output are indicated for clarification. $T_g = 300$ K and $p = 0.5$ Torr.

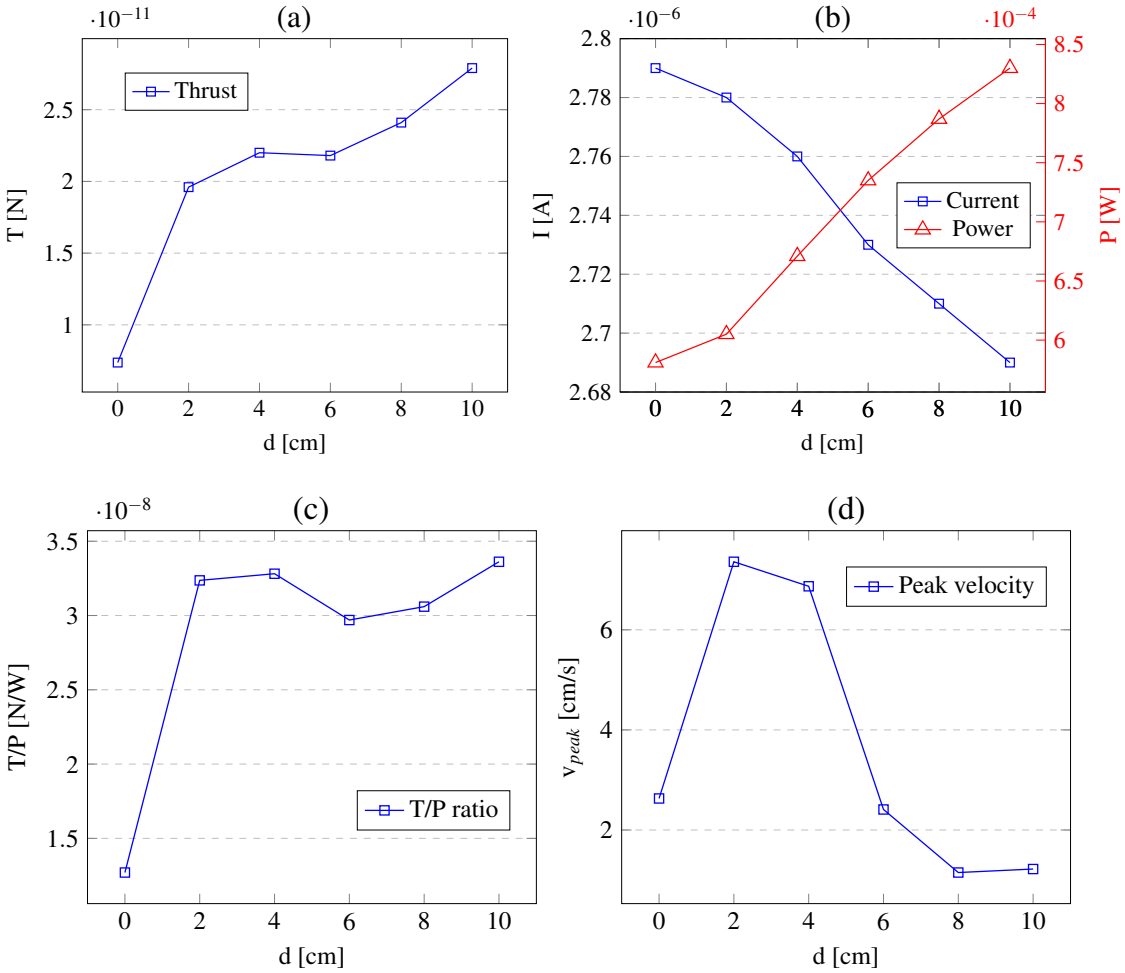

Figure 6.10: (a) Thrust, (b) current and power, (c) T/P ratio, and (d) peak velocity as functions of gap between electrodes, $T_g = 300$ K and $p = 0.5$ Torr.

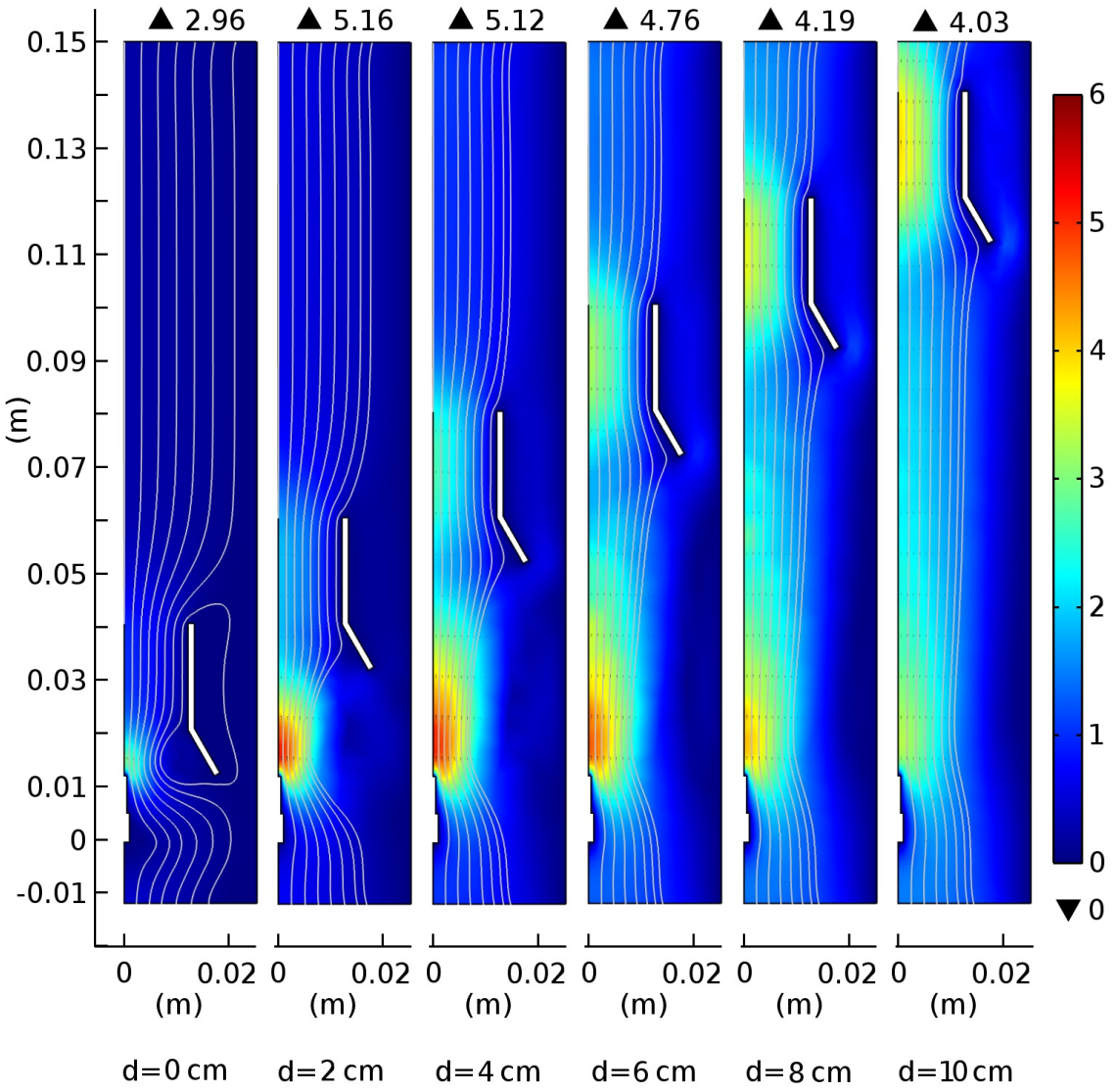

Figure 6.11: Velocity profile [cm/s] (peak values on top) for several values of gap between electrodes, $T_g = 300$ K and $p = 10$ Torr.

limit was not reached due to computational constraints and will be address in a future work but it was pointed out before by Masuyama (2012).

As shown in Figure 6.12c, the thrust-to-power ratio, T/P, also increases, an evidence of the optimization of momentum transfer and absorption of energy. Although the peak velocity of the distribution was found higher for a gap of 3 cm (see Figure 6.12d) while decreasing for longer electrodes's gaps, the T/P ratio kept increasing for all the distances considered in the study.

When comparing the two scenarios, the gas pressure of 0.5 Torr and 10 Torr, the tendencies of the performance parameters prove to be similar, as the all increase or decrease with the gap between electrodes in a consistent manner in both cases. The best performance of the EHD thruster is clearly given by the case with a gas pressure of 10 Torr (as expected from the discussion on gas pressure dependency on section 6.1) for the cases with the highest gap was considered, i.e. d=10 cm.

The results, in the range of the gap between electrodes that were considered here, point towards a direct proportionality between the produced thrust and the gap distance. An inversely-proportional relation between thrust and gap was predicted in the one-dimensional analysis, specifically in Equation 3.2. It must be noticed that the results of the variation of gap between electrodes presented here do not impose the discharge current, and consequently the onset voltage between electrodes. As the gap slightly increases the onset voltage increases in a bigger proportion, producing an ever-increasing total thrust.

6.6 Conclusions

An axisymmetric 2-D simulation of a one-stage DC-powered EHD thruster with a funnel-like cathode that runs with nitrogen gas shows that the net produced thrust, thrust efficiency and the peak gas velocity vary proportionally with pressure. The systematic study carried out in this work has shown that gas pressure plays an important role in the performance of the thruster since it is the variable that impacts the most the fluid between electrodes.

The EHD thruster performed better under lower gas temperatures, suggesting that cold neutral gas flowing between electrodes is the target flow for improving the thruster's operation.

This model also has shown that thrust increases with the electric current flowing between electrodes and this variable can be optimized by appropriate control of the ballast resistance for several gas pressure values.

The secondary electron emission is often considered a necessary phenomenon for sustaining DC-discharges; we show how the performance of the discharge decreases when the SEE coefficient, γ_i, is greater than 10^{-2} for the proposed geometry at 10 Torr and 300 K.

The distance between electrodes influences the onset potential and the total current. When increased sufficiently, the gas velocity peak transits from the anode's tip to the interior of the thruster's chamber. More research is needed into finding the limits to which the distance can be extended and while maintaining the discharge and its performance.

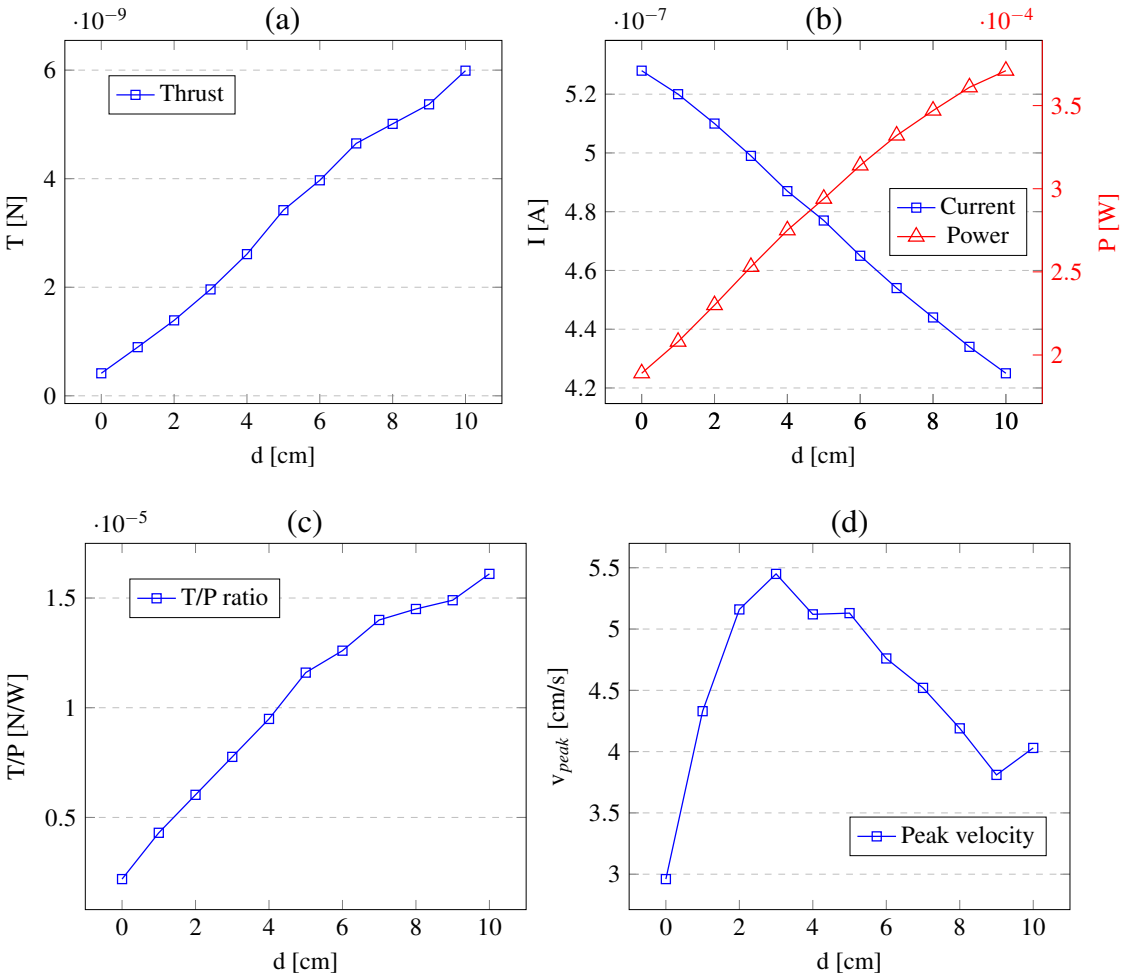

Figure 6.12: (a) Thrust, (b) current and power, (c) T/P ratio, and (d) peak velocity as functions of gap between electrodes, $T_g = 300$ K and $p = 10$ Torr.

Chapter 7

Conclusions and Future Work

On this chapter we discuss the main conclusions drawn from the results of the investigation along with lines of work that could be developed on the future to further the understanding in the topic of electrohydrodynamic thrusters.

7.1 Discussion

The basic variables and parameters that characterize the space propulsion systems were identify and defined in order to frame the investigation of the EHD thrusters with the electric propulsion subject, even including the chemical propulsion principles.

A comparison between plasma-based and chemical technologies was made in terms how they may be applicable for different scenarios (e.g., duration of the trips, attainable travel velocities and total thrust). There is not a single best propulsion system, but some of them are better in specific tasks, and so we need to consider the characteristics of each flight before choosing its adequate propulsion system.

The new proposed model for EHD thrusters combines several modules that contain different aspects of the physical phenomena and couples them in order to find steady state solutions to several geometrical configurations and propellant gases.

Single-stage, hallow-cathode, electrohydrodynamic thruster models were implemented in a finite-element methodology for solving its differential equations across a two-dimensional axisymmetric space.

The performance of the considered thrusters was evaluated and compared when using three cathode geometries (conical, cylindrical and funnel-like), each employing three working gases (argon, nitrogen and oxygen).

For a gas pressure of 0.5 Torr, the funnel-like cathode presented the best thrust value (5.18 nN) for nitrogen gas, while the most efficient configuration (24.59 μN/W) was presented by the conical cathode, also using nitrogen gas. The most promising gas with a pressure of 0.5 Torr is nitrogen.

At a gas pressure of 10 Torr, the highest thrust value (107.1 nN) was obtained using the funnel-like cathode with oxygen as the working gas, while the highest thrust-to-power ratio (685.6 μN/W) was obtained using the cylindrical cathode, also using oxygen gas.

The gas pressure was found to have a strong impact on the performance of the EHD thruster, specially for pressures in the range of [0.25-20] Torr. The pressure should not be deliberately increased in the model without considering that the set of reactions representing the discharge changes with the pressure. New species, not considered here, are present more significantly as we get closer to atmospheric pressure.

The gas temperature mildly affects the performance of the thruster. Contrary to common intuition, it was found that lower gas temperatures improve the thrust production since the gas density increases for colder gases if pressure is maintained constant. Gas density is directly proportional to thrust.

The discharge current was found to have a directly proportional relation with the produced thrust, when gas pressure, gas temperature and distance between electrodes was kept constant, similarly to the analysis of one-dimensional EHD thrusters.

Secondary electron emission from the cathode introduces electrons into the plasma bulk and sustains the discharge between electrodes, but if the emission becomes too high, a current channel seems to form, lowering the electric field responsible for the acceleration of ions and thus diminishing the gas velocity.

The distance between electrodes is directly proportional to the produced thrust, taking into consideration that the current between electrodes must be kept constant. The discharge current does not maintain constant naturally after changing the separation of the electrodes so adjusting the voltage or the ballast resistance must be taken into consideration.

7.2 Future Work

The following are lines of work that are worth exploring since they all point towards the improvement of the presented models of EHD thrusters.

The models for the EHD thrusters studied in this work are single-stage, meaning that only two current-carrying electrodes are present in the thruster. It is possible to add more electrodes and thus, increase have a multi-stage thruster. According to Ieta and Ellis (2013), we could increase the stages up to three, since results show that after that number the thrust obtained increases only marginally while consuming more power and the system increases in complexity unnecessarily.

The introduction of other working gases such as xenon, and mixtures of gases (e.g., N_2-O_2), might contribute to improve the operation of the EHD thrusters.

The inclusion of a more complete set of reactions for the nitrogen and oxygen gases, specifically the vibrational and rotational states.

To implement the solution to the Boltzmann equation (Boltzmann EEDF) in order to find the reaction rates of the electron impact reactions and the transport parameters of the discharge. An implementation of the Boltzmann equation is expected to increase the level of detail in the

simulation of the EHD thrusters, in contrast to the currently assumed Maxwellian EEDF, which, as explained in Chapter 3, has its inherent limitations.

The geometrical characteristics of the electrodes is an ever-present challenge, the use of more complex (and proven) geometries might improve the performance of the EHD thruster, for example a cathode in the form de Laval nozzle (convergent-divergent nozzle).

A clear step towards improving the reliability of the results is to build and test EHD thrusters in a controlled environment so that comparison can be made with the expected values given by the simulations.

Other discharge regimes (in counterpart to the currently used DC mode) are also worth exploring, such as: pulsed mode or alternate current (AC) mode.

Appendix A

Code flowchart

The following is a representation of the flowchart of modules or groups of equations solved on each simulation step in order to achieve steady state solutions for the EHD thrusters for any given working gas and electrode's geometry.

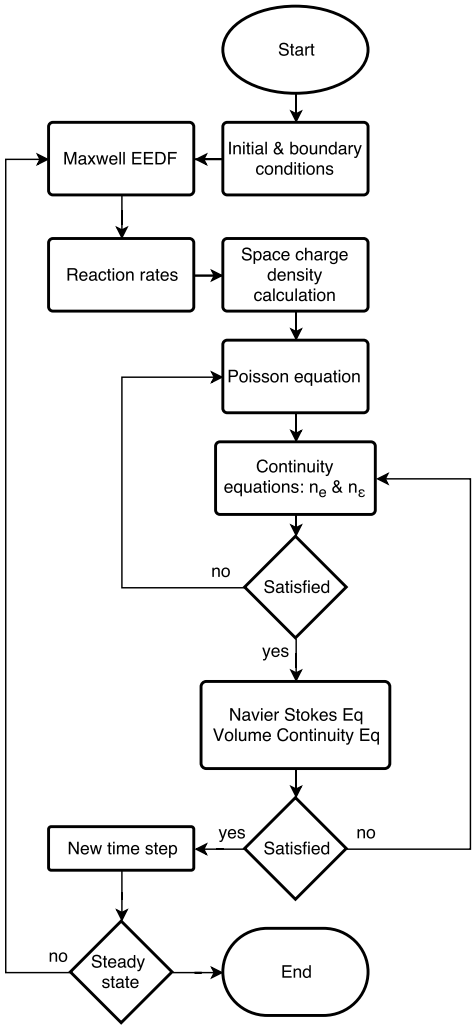

Figure A.1: Flow chart of for the steady state simulations of EHD thrusters

Appendix B

Model implementation on COMSOL Multiphysics

The present section depicts a simplified and representative view of a typical implementation report for the EHD thruster model in the software COMSOL Multiphysics® for the case of funnel cathode geometry and nitrogen gas at gas pressure of 10 Torr.

In order to compact the available data the definitions and characteristics of all species are not shown. The simulation steps taken by the solver and other non-interesting features are not shown either.

1 Component 1

1.1 DEFINITIONS

1.1.1 Variables

Name	Expression	Unit	Description
V0	3[kV]	V	Electric Potential on Anode
Vin	V0*tanh(1E6*t[1/s])	V	
p0	10[Torr]	Pa	Gas Pressure
Rb	5000[Mohm]	Ω	Ballast Resistance
mueN	2.102E24 [1/(V*m*s)]	1/(V·m·s)	Electron mobility
Wf	5 [V]	V	Work Fuction
gammai	0.05		Secondary electron emission coefficient
qe	1.602176487E-19[C]	C	Electron charge
T0	300 [K]	K	Gas Temperature
N_A	6.02214129E23[1/mol]	1/mol	Avogadro Constant
M	28.0134E-3 [kg/mol]	kg/mol	Molar Mass N2
R	8.314 [J/(K*mol)]	J/(mol·K)	Ideal gas constant

1.2 MATERIALS

1.2.1 Nitrogen

Description	Value
Dynamic viscosity	eta(T[1/K])[Pa*s]
Ratio of specific heats	1.4
Heat capacity at constant pressure	Cp(T[1/K])[J/(kg*K)]
Density	rho(pA[1/Pa], T[1/K])[kg/m^3]
Thermal conductivity	{{k(T[1/K])[W/(m*K)], 0, 0}, {0, k(T[1/K])[W/(m*K)], 0}, {0, 0, k(T[1/K])[W/(m*K)]}}

FUNCTIONS

Function name	Type
eta	Piecewise
Cp	Piecewise
rho	Analytic
k	Piecewise

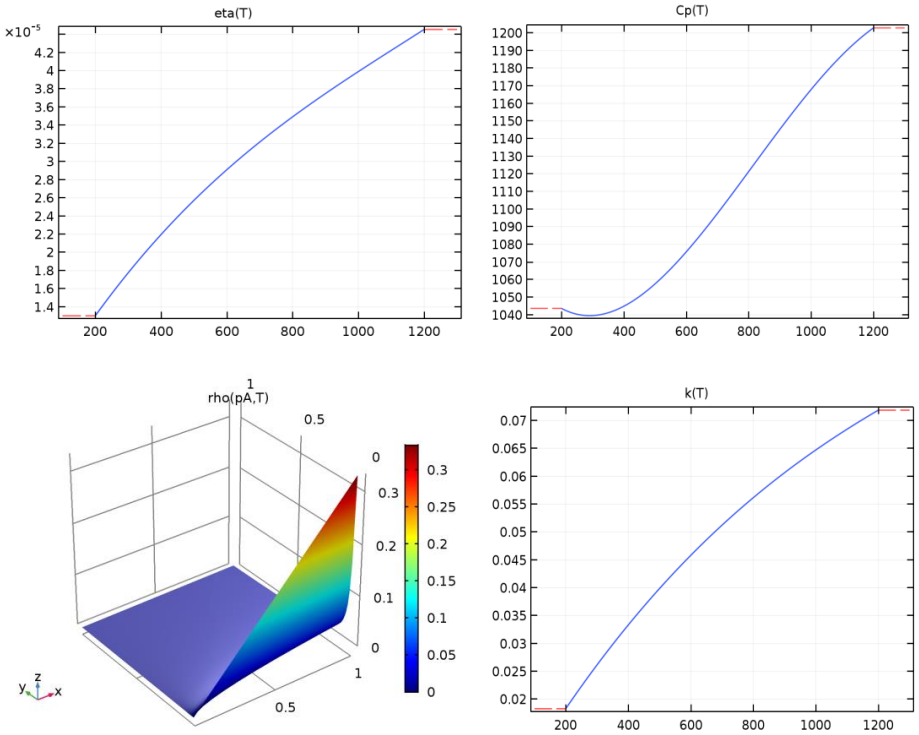

1.3 DC DISCHARGE

EQUATIONS

$$\nabla \cdot \mathbf{D} = \rho_q \qquad \frac{\partial n_e}{\partial t} + \nabla \cdot \mathbf{\Gamma}_e = R_e - (\mathbf{u} \cdot \nabla) n_e$$

$$\mathbf{E} = -\nabla V \qquad \frac{\partial n_\epsilon}{\partial t} + \nabla \cdot \mathbf{\Gamma}_\epsilon + \mathbf{E} \cdot \mathbf{\Gamma}_e = S_{en} - (\mathbf{u} \cdot \nabla) n_\epsilon + (Q + Q_{gen})/q$$

1.3.1 Cross section import

1.3.2 1: e+N2=>e+N2

EQUATIONS

$$r = k^f \prod_{k=1}^{Q} c_k^{\nu} \qquad k^f = \gamma \int_0^{\infty} \epsilon \sigma_k(\epsilon) f(\epsilon) d\epsilon$$

SETTINGS

Description	Value
Formula	e+N2=>e+N2
Valid reaction	1

Description	Value
Reaction defined	0
Use Arrhenius expressions	Off
Reverse frequency factor	1
Reverse rate constant	1
Equilibrium constant	0
Specify equilibrium constant	Off
Forward stoichiometric array	{-1, -1, 0, 0, 0, 0}
Reverse stoichiometric array	{1, 1, 0, 0, 0, 0}
Stoichiometric array	{0, 0, 0, 0, 0, 0}
Reactant	{e, N2}
Product	{e, N2}
Species	{e, N2}
Reaction sequence number	1
Reaction type	Irreversible
Reverse activation energy	0
Collision sequence number	0
Electron mass ratio	1.959600e-5
Scaling of electron energy	1
Scaling of cross section data	1
Collision type	Elastic
Electron energy	{0.000000e+0, 1.000000e-3, 2.000000e-3, 3.000000e-3, 5.000000e-3, 7.000000e-3, 8.500000e-3, 1.000000e-2, 1.500000e-2, 2.000000e-2, 3.000000e-2, 4.000000e-2, 5.000000e-2, 7.000000e-2, 1.000000e-1, 2.000000e-1, 3.000000e-1, 4.000000e-1, 5.000000e-1, 6.000000e-1, 7.000000e-1, 8.000000e-1, 9.000000e-1, 1.000000e+0, 1.100000e+0, 1.200000e+0, 1.300000e+0, 1.400000e+0, 1.500000e+0, 1.600000e+0, 1.700000e+0, 1.800000e+0, 1.900000e+0, 2.000000e+0, 2.100000e+0, 2.200000e+0, 2.300000e+0, 2.400000e+0, 2.500000e+0, 2.600000e+0, 2.700000e+0, 2.800000e+0, 2.900000e+0, 3.000000e+0, 3.100000e+0, 3.200000e+0, 3.300000e+0, 3.400000e+0, 3.500000e+0, 3.600000e+0, 3.700000e+0, 3.800000e+0, 3.900000e+0, 4.000000e+0, 4.100000e+0, 4.200000e+0, 4.300000e+0, 4.400000e+0, 4.500000e+0, 4.600000e+0, 4.700000e+0, 4.800000e+0, 4.900000e+0, 5.000000e+0, 5.100000e+0, 5.200000e+0, 5.300000e+0, 5.400000e+0, 5.500000e+0, 5.600000e+0, 5.700000e+0, 5.800000e+0, 5.900000e+0, 6.000000e+0, 6.100000e+0, 6.200000e+0, 6.300000e+0, 6.400000e+0, 6.500000e+0, 6.600000e+0, 6.700000e+0, 6.800000e+0, 6.900000e+0, 7.000000e+0, 8.000000e+0, 1.000000e+1, 1.200000e+1, 1.500000e+1, 1.700000e+1, 2.000000e+1, 2.500000e+1, 3.000000e+1, 4.000000e+1, 5.000000e+1, 7.500000e+1, 1.000000e+2, 1.500000e+2, 2.000000e+2, 3.000000e+2, 5.000000e+2, 7.000000e+2, 1.000000e+3, 1.500000e+3, 2.000000e+3, 3.000000e+3, 5.000000e+3, 7.000000e+3, 1.000000e+4, 1.001000e+4}
Collision cross section data	{1.100000e-20, 1.360000e-20, 1.490000e-20, 1.620000e-20, 1.810000e-20, 2.000000e-20, 2.100000e-20, 2.190000e-20, 2.550000e-20, 2.850000e-20, 3.400000e-20, 3.850000e-20, 4.330000e-20, 5.100000e-20, 5.950000e-20, 7.900000e-20, 9.000000e-20, 9.680000e-20, 9.900000e-20, 9.950000e-20, 1.000000e-19, 1.000000e-19, 1.000000e-19, 1.000000e-19, 1.010000e-19, 1.040000e-19, 1.100000e-19, 1.150000e-

Description	Value
	19, 1.200000e-19, 1.270000e-19, 1.380000e-19, 1.530000e-19, 1.960000e-19, 2.350000e-19, 2.700000e-19, 2.850000e-19, 2.930000e-19, 2.980000e-19, 3.000000e-19, 3.000000e-19, 2.970000e-19, 2.800000e-19, 2.500000e-19, 2.170000e-19, 2.040000e-19, 1.850000e-19, 1.720000e-19, 1.630000e-19, 1.540000e-19, 1.470000e-19, 1.400000e-19, 1.350000e-19, 1.300000e-19, 1.260000e-19, 1.230000e-19, 1.200000e-19, 1.175000e-19, 1.150000e-19, 1.130000e-19, 1.120000e-19, 1.108000e-19, 1.097000e-19, 1.092000e-19, 1.090000e-19, 1.085000e-19, 1.082000e-19, 1.080000e-19, 1.074000e-19, 1.070000e-19, 1.068000e-19, 1.060000e-19, 1.052000e-19, 1.048000e-19, 1.040000e-19, 1.030000e-19, 1.025000e-19, 1.020000e-19, 1.018000e-19, 1.015000e-19, 1.012000e-19, 1.012000e-19, 1.012000e-19, 1.010000e-19, 1.010000e-19, 1.000000e-19, 1.040000e-19, 1.090000e-19, 1.100000e-19, 1.070000e-19, 1.020000e-19, 9.500000e-20, 9.000000e-20, 8.800000e-20, 8.600000e-20, 6.600000e-20, 5.800000e-20, 4.900000e-20, 4.200000e-20, 3.300000e-20, 2.440000e-20, 1.960000e-20, 1.550000e-20, 1.120000e-20, 8.100000e-21, 6.300000e-21, 4.000000e-21, 2.900000e-21, 2.100000e-21, 1.000000e-50}
Specify reaction using	Cross section data
Electron energy distribution function	From physics interface property
Townsend coefficient	1
Electron energy	V
Collision cross section data	m^2
Reduced electric field	V*m^2

1.3.3 Species: N2

EQUATIONS

$$w = 1 - \sum_{k=1}^{Q} w_k$$

SETTINGS

Description	Value
Species is defined	1
Dependent	0
Surface sequence number	0
Lock concentration/activity	Off
Lock concentration/activity	Off
Species label	N2
Charge	0
Old rate expression	0
Rate expression	0
Surface rate expression	0
Old surface rate expression	0

Description	Value
Molar entropy	0
Molar enthalpy	0
Heat capacity at constant pressure	0
Diffusivity	1E-4[m^2/s]
Mobility	dc.Dm_wN2*e_const/k_B_const/dc.T
Dynamic viscosity	0
Thermal conductivity	0
Feed inlet selection	0
Feed stream concentration	0
Feed stream molar enthalpy	0
Inlet molar flow	0
Volumetric feed rate	0
Feed stream temperature	0
Additional enthalpy contribution	0
Species level	Gas phase
Species type	Neutral
Mass fraction	1E-8
Thermal diffusion coefficient	0
From mass constraint	On
Site occupancy number	0
Specification	Compute mobility and diffusivity
Ion temperature	Use gas temperature
Specify using	Constant value
Ion mobility	{{0, 0, 0}, {0, 0, 0}, {0, 0, 0}}
Electric field	0
Reduced electric field	0
Preset species data	N2
Polarizability	1.64[angstrom^3]
Cross section	7e-19[m^2]

1.3.4 Species: N2+

EQUATIONS

$$\rho\frac{\partial w}{\partial t}+\rho(\mathbf{u}\cdot\nabla)w=\nabla\cdot\mathbf{j}+R_i \qquad \mathbf{j}=\rho w\boldsymbol{V}_d \qquad \boldsymbol{V}_d=D_i^m\nabla\ln(w)+D_i^m\nabla\ln(M_n)+\frac{D_i^T}{\rho w}\nabla\ln(T)-z_iu_m\mathbf{E}$$

SETTINGS

Description	Value
Species is defined	1
Dependent	0
Surface sequence number	0
Lock concentration/activity	Off
Lock concentration/activity	Off
Species label	N2+
Reset to default	0
Charge	1
Old rate expression	0
Rate expression	0
Surface rate expression	0
Heat capacity at constant pressure	0
Diffusivity	1E-4[m^2/s]
Mobility	2.01E-4
Dynamic viscosity	0
Thermal conductivity	0
Species type	Ion
Mass fraction	1E-8
Thermal diffusion coefficient	0
Initial value from electroneutrality constraint	On
Specification	Specify mobility, compute diffusivity
Ion temperature	Use gas temperature
Specify using	Constant value
Ion mobility	{{0, 0, 0}, {0, 0, 0}, {0, 0, 0}}
Electric field	0
Reduced electric field	0
Preset species data	N2
Polarizability	1.64[angstrom^3]
Cross section	7e-19[m^2]

1.3.5 1: N2+=>N2

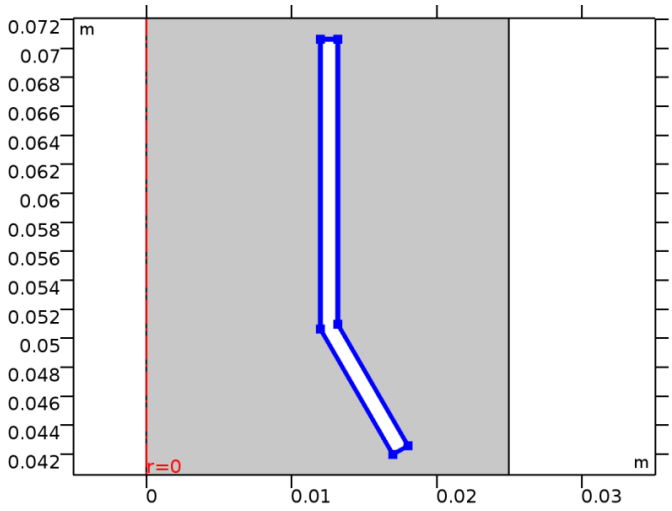

EQUATIONS

$$r = k_s^f \prod_{k=1}^{Q} c_k^{\nu}$$

$$k_s^f = \left(\frac{\gamma_f}{1-\gamma_f/2}\right) \frac{1}{(\Gamma_{tot})^m} \frac{1}{4} \sqrt{\frac{8RT}{\pi M_n}}$$

SETTINGS

Description	Value
Formula	N2 + =>N2
Valid reaction	1
Reaction defined	0
Use Arrhenius expressions	Off
Forward sticking coefficient	1
Forward stoichiometric array	{0, 0, -1, 0, 0, 0}
Reverse stoichiometric array	{0, 1, 0, 0, 0, 0}
Stoichiometric array	{0, 1, -1, 0, 0, 0}
Reactant	N2+
Product	N2
Species	{N2_1p, N2}
Reaction sequence number	1
Secondary emission coefficient	gammai
Mean energy of secondary electron	15.5 - 2*Wf
Specify reaction using	Sticking coefficient
Motz-Wise correction	On

1.3.6 Plasma Model 1

EQUATIONS

$$\frac{\partial n_e}{\partial t} + \nabla \cdot \mathbf{\Gamma}_e = R_e - (\mathbf{u} \cdot \nabla) n_e$$
$$\mathbf{\Gamma}_e = -(\mu_e \cdot \mathbf{E}) n_e - \mathbf{D}_e \cdot \nabla n_e$$
$$\frac{\partial n_\epsilon}{\partial t} + \nabla \cdot \mathbf{\Gamma}_\epsilon + \mathbf{E} \cdot \mathbf{\Gamma}_e = S_{en} - (\mathbf{u} \cdot \nabla) n_\epsilon + (Q + Q_{gen})/q$$
$$\mathbf{\Gamma}_\epsilon = -(\mu_{en} \cdot \mathbf{E}) n_\epsilon - \mathbf{D}_{en} \cdot \nabla n_\epsilon$$
$$\mathbf{E} = -\nabla V$$
$$\nabla \cdot (\epsilon_0 \epsilon_r \mathbf{E}) = \rho_q$$

SETTINGS

Description	Value
Magnetic flux density	User defined
Magnetic flux density	{0, 0, 0}
Reduced electron mobility	{{mueN, 0, 0}, {0, mueN, 0}, {0, 0, mueN}}
DC electron mobility	4E4[m^2/(V*s)]
Reduced DC electron mobility	4E4[m^2/(V*s)]
Electron flux norm	0
Electron transport properties	Specify mobility only
Velocity field	Velocity field (spf)
Mixture density	Ideal gas
Temperature	User defined
Temperature	T0
Absolute pressure	User defined
Absolute pressure	root.comp1.p + p0
Total mass flow	0
Initial mean electron energy	3
Power absorbed	0
Mean kinetic energy lost per electron lost	0
Mean kinetic energy lost per ion lost	0
Mean electron energy	0

1.3.7 Initial Values 1

SETTINGS

Description	Value
Initial electron density	1E13 [1/m^3]
Initial mean electron energy	4 [V]
Electric potential	0

Variables

Name	Expression	Unit	Description	Selection
dc.neinit	1.0E13[1/m^3]	$1/m^3$	Initial electron density	Domain 1
dc.ebarinit	4[V]	V	Initial mean electron energy	Domain 1

1.3.8 Wall 1

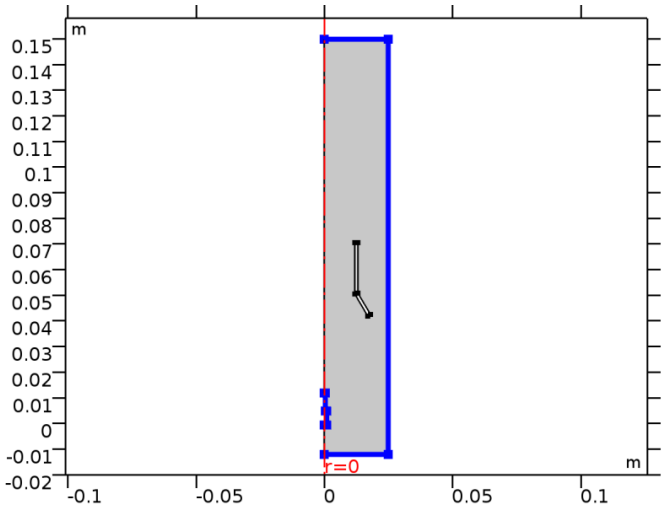

EQUATIONS

$$\mathbf{n}\cdot\boldsymbol{\Gamma}_e = \frac{1-r_e}{1+r_e}\left(\frac{1}{2}\nu_{e,th}n_e\right) - \left(\sum\gamma_i(\boldsymbol{\Gamma}_i\cdot\mathbf{n}) + \boldsymbol{\Gamma}_t\cdot\mathbf{n}\right)$$

$$\mathbf{n}\cdot\boldsymbol{\Gamma}_\epsilon = \frac{1-r_e}{1+r_e}\left(\frac{5}{6}\nu_{e,th}n_\epsilon\right) - \left(\sum\gamma_i\epsilon_i(\boldsymbol{\Gamma}_i\cdot\mathbf{n}) + \epsilon(\boldsymbol{\Gamma}_t\cdot\mathbf{n})\right)$$

SETTINGS

Description	Value
Reflection coefficient	0
Drift direction	0
Thermal emission flux	0
Mean thermionic energy	0

Description	Value
Mean electron energy at the wall	0
Use wall for electron density	On
Use wall for electron energy	On
Include migration effects	Off

1.3.9 Ground 1

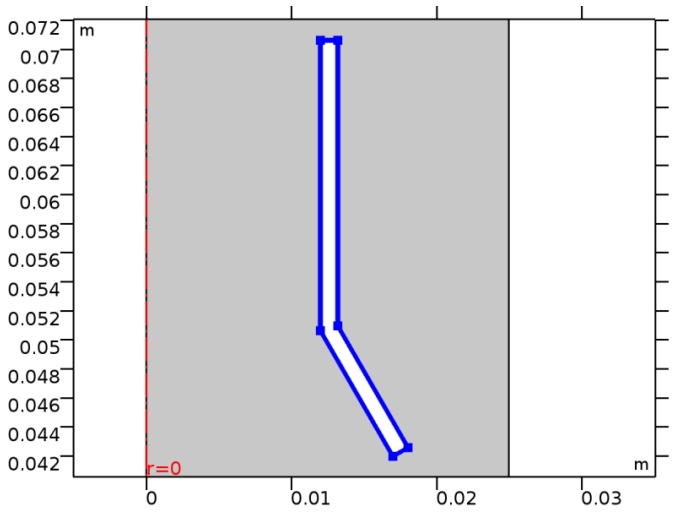

EQUATIONS

$V = 0$

SETTINGS

Description	Value
Apply reaction terms on	All physics (symmetric)
Use weak constraints	Off
Constraint method	Elemental

Variables

Name	Expression	Unit	Description	Selection
dc.V0	0	V	Electric potential	Boundaries 11–16

1.3.10 Metal contact (Electric Potential 1)

This feature was created from the selection of an Electric Potential feature on boundaries adjacent to the plasma domain.

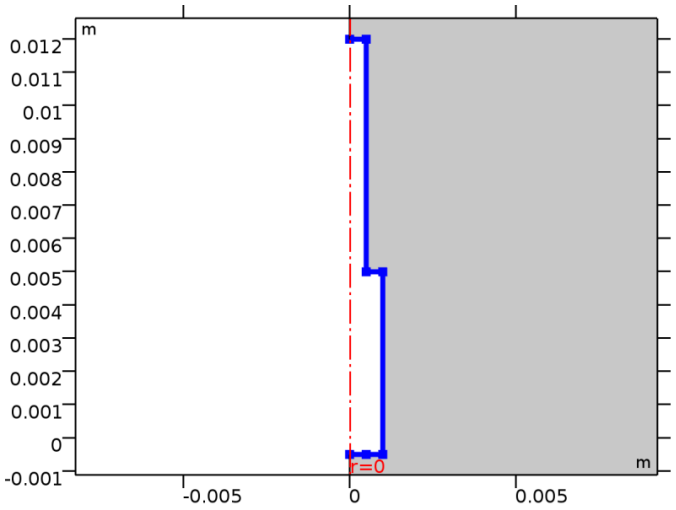

Metal contact (Electric Potential 1)

EQUATIONS

$$V = V_0 - I_p R_b$$

$$I_p = \int_{\partial\Omega} (\mathbf{n}\cdot\mathbf{J}_i + \mathbf{n}\cdot\mathbf{J}_e + \mathbf{n}\cdot\mathbf{J}_d)\mathrm{d}S$$

SETTINGS

Description	Value
Terminal name	pot1_mc
Electric potential	Vin
Quick circuit type	Ballast resistor
Ballast resistor	Rb
Apply reaction terms on	All physics (symmetric)
Use weak constraints	Off
Constraint method	Elemental
Current	User defined
Current	0
Terminal type	Voltage

1.3.11 Dielectric contact (External Surface Charge Accumulation 1)

This feature replaces the Surface Charge Accumulation feature on boundaries adjacent to the plasma domain.

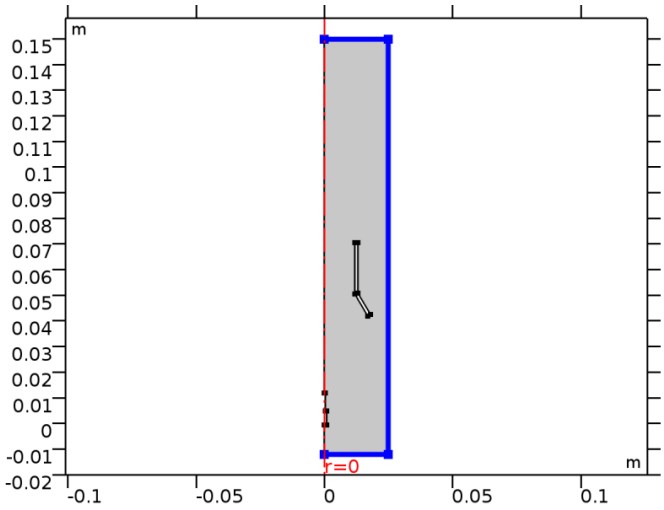

Dielectric contact (External Surface Charge Accumulation 1)

EQUATIONS

$$-\mathbf{n}\cdot\mathbf{D}=\sigma_s$$

$$\frac{\partial\sigma_s}{\partial t}=\mathbf{n}\cdot\mathbf{J}_i+\mathbf{n}\cdot\mathbf{J}_e$$

SETTINGS

Description	Value
Surface charge type	Surface charge accumulation
Enable distributed capacitance	Off

1.4 LAMINAR FLOW

EQUATIONS

$$\rho\frac{\partial \mathbf{u}}{\partial t}+\rho(\mathbf{u}\cdot\nabla)\mathbf{u}=$$
$$\nabla\cdot\left[-p\mathbf{I}+\mu\left(\nabla\mathbf{u}+(\nabla\mathbf{u})^{T}\right)\right]+\mathbf{F}$$
$$\rho\nabla\cdot(\mathbf{u})=0$$

SETTINGS

Description	Value
Discretization of fluids	P1 + P1
Value type when using splitting of complex variables	{Real, Real, Real, Real, Real, Real, Real, Real, Real, Real, Real, Real}
Isotropic diffusion	Off
Compressibility	Incompressible flow
Turbulence model type	None
Reference pressure level	p0
Reference temperature	T0
Use pseudo time stepping for stationary equation form	Off
Streamline diffusion	On
Crosswind diffusion	On

1.4.1 Fluid Properties 1

EQUATIONS

$$\rho\frac{\partial \mathbf{u}}{\partial t}+\rho(\mathbf{u}\cdot\nabla)\mathbf{u}=$$
$$\nabla\cdot\left[-p\mathbf{I}+\mu\left(\nabla\mathbf{u}+(\nabla\mathbf{u})^{T}\right)\right]+\mathbf{F}$$
$$\rho\nabla\cdot(\mathbf{u})=0$$

SETTINGS

Description	Value
Density	User defined
Density	M*p0/(R*T0)
Dynamic viscosity	User defined
Dynamic viscosity	1.79E-5

1.4.2 Wall 1

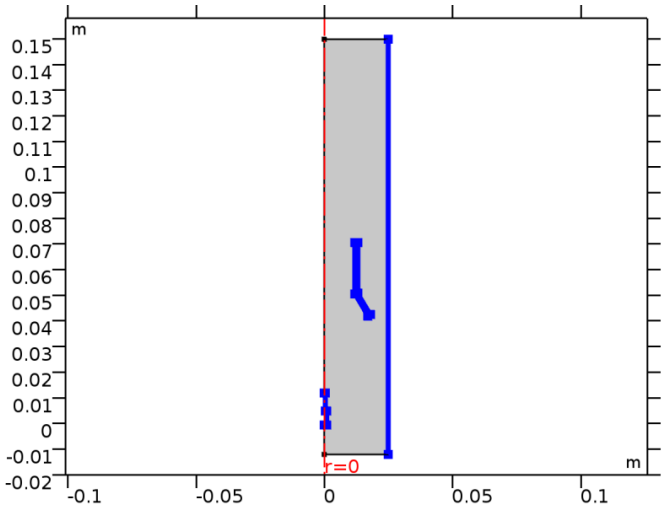

Wall 1

SELECTION

Geometric entity level	Boundary
Selection	Boundaries 3, 5, 7–17

EQUATIONS

$$\mathbf{u} = \mathbf{0}$$

SETTINGS

Description	**Value**
Boundary condition	No slip
Apply reaction terms on	Individual dependent variables
Use weak constraints	Off
Constraint method	Elemental

1.4.3 Outlet 1

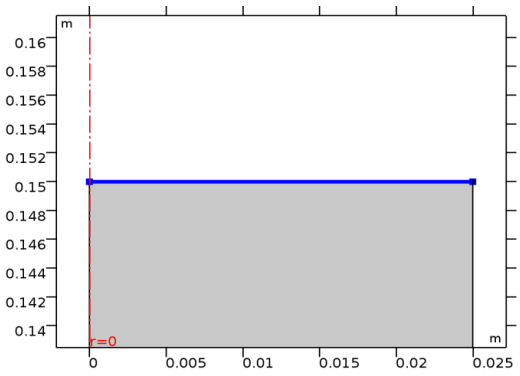

SELECTION

Geometric entity level	Boundary
Selection	Boundary 6

EQUATIONS

$$\left[-p\mathbf{I}+\mu\left(\nabla\mathbf{u}+(\nabla\mathbf{u})^{\mathrm{T}}\right)\right]\mathbf{n}=-\hat{p}_0\mathbf{n}$$

$$\hat{p}_0 \le p_0,$$

SETTINGS

Description	Value
Boundary condition	Pressure
Pressure	p0
Normal flow	Off
Suppress backflow	On
Apply reaction terms on	All physics (symmetric)
Use weak constraints	Off

1.4.4 Inlet 1

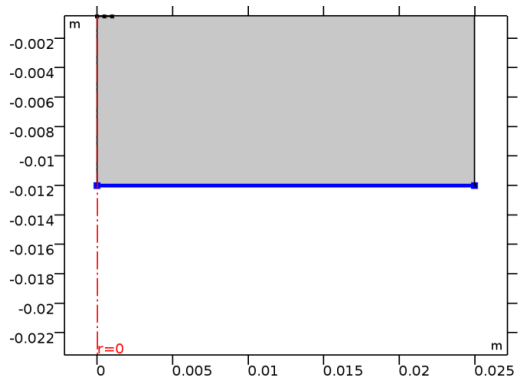

SELECTION

Geometric entity level	Boundary
Selection	Boundary 2

EQUATIONS

$$p = p_0,\ \left[\mu\left(\nabla\mathbf{u}+(\nabla\mathbf{u})^{\mathrm{T}}\right)\right]\mathbf{n}=0$$

SETTINGS

Description	Value
Apply reaction terms on	All physics (symmetric)
Use weak constraints	Off
Boundary condition	Pressure, no viscous stress
Pressure	p0

1.4.5 Volume Force 1

EQUATIONS

$$\rho\frac{\partial \mathbf{u}}{\partial t}+\rho(\mathbf{u}\cdot\nabla)\mathbf{u}=\nabla\cdot\left[-p\mathbf{I}+\mu\left(\nabla\mathbf{u}+(\nabla\mathbf{u})^{T}\right)\right]+\underline{F}$$

Variables

Name	Expression	Unit	Description	Selection
spf.Fr	qe*(-dc.ne+dc.n_wN2_1p+dc.n_wN_1p+dc.n_wN4_1p)*dc.Er	N/m^3	Volume force, r component	Domain 1
spf.Fphi	0	N/m^3	Volume force, phi component	Domain 1
spf.Fz	qe*(-dc.ne+dc.n_wN2_1p+dc.n_wN_1p+dc.n_wN4_1p)*dc.Ez	N/m^3	Volume force, z component	Domain 1

1.5 MESH 1

MESH STATISTICS

Description	Value
Minimum element quality	0.03343
Average element quality	0.7203
Triangular elements	823
Quadrilateral elements	164
Edge elements	137
Vertex elements	17

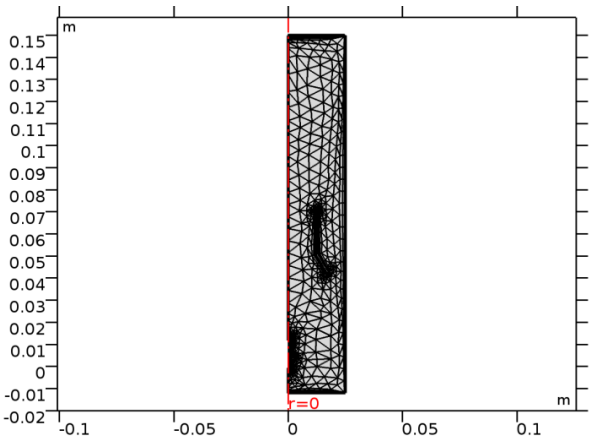

Mesh 1

1.5.1 Size (size)

SETTINGS

Description	Value
Calibrate for	Fluid dynamics
Maximum element size	0.0055
Minimum element size	1.75E-4
Resolution of narrow regions	0.9
Maximum element growth rate	1.4
Predefined size	Extremely coarse

2 Study 1

COMPUTATION INFORMATION

CPU	Intel(R) Core(TM) i5-3570K CPU @ 3.40GHz, 4 cores
Operating system	Windows 7

2.1 TIME DEPENDENT

Times	Unit
0 10^{range(-10,10/20,0)}	s

2.2 SOLVER CONFIGURATIONS

2.2.1 Solver 1

TIME STEPPING

Description	Value
Initial step	1.0E-13
Initial step	On
Maximum BDF order	2
Fraction of initial step for Backward Euler	0.0010
Error estimation	Exclude algebraic

```
Dependent Solver 1 in Solver 1: Solution time: 1588 s (26 minutes, 28 seconds)
                                      Physical memory: 1.22 GB
                                      Virtual memory: 1.25 GB
```

Fully Coupled 1 (fc1)

GENERAL

Description	Value
Linear solver	Direct 1

METHOD AND TERMINATION

Description	Value
Jacobian update	Once per time step
Maximum number of iterations	6

Direct 1 (d1)

Description	Value
Solver	PARDISO
Multithreaded forward and backward solve	Off
Out-of-core	Off

3 Results

3.1 ELECTRON DENSITY (DC)

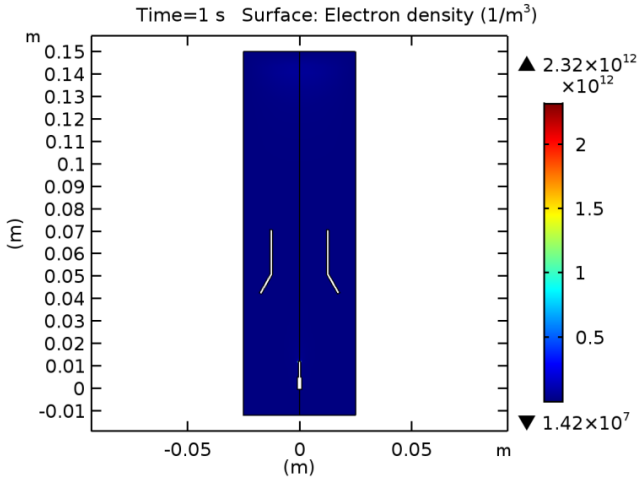

Time=1 s Surface: Electron density (1/m^3)

3.2 ELECTRON TEMPERATURE (DC)

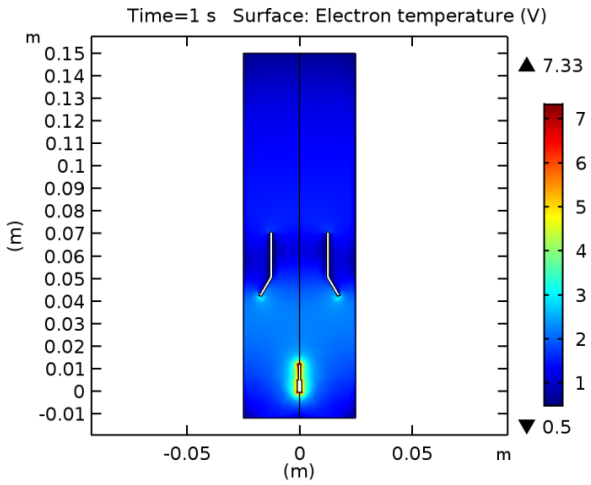

Time=1 s Surface: Electron temperature (V)

3.3 ELECTRIC POTENTIAL (DC)

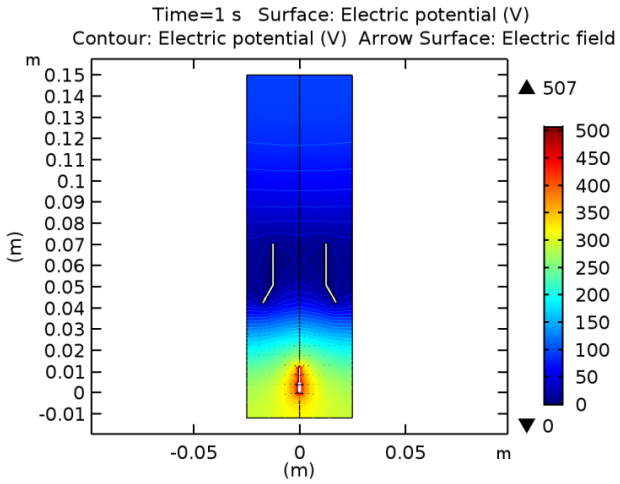

Time=1 s Surface: Electric potential (V) Contour: Electric potential (V) Arrow Surface: Electric field

3.4 VELOCITY

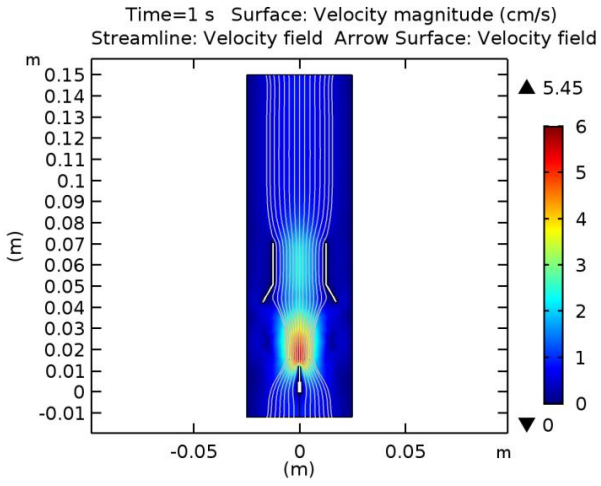

Time=1 s Surface: Velocity magnitude (cm/s) Streamline: Velocity field Arrow Surface: Velocity field

3.5 PRESSURE

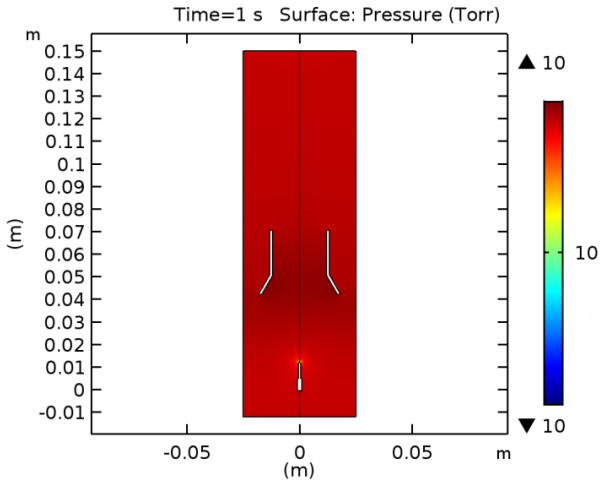

Time=1 s Surface: Pressure (Torr)

3.6 VOLTAGES

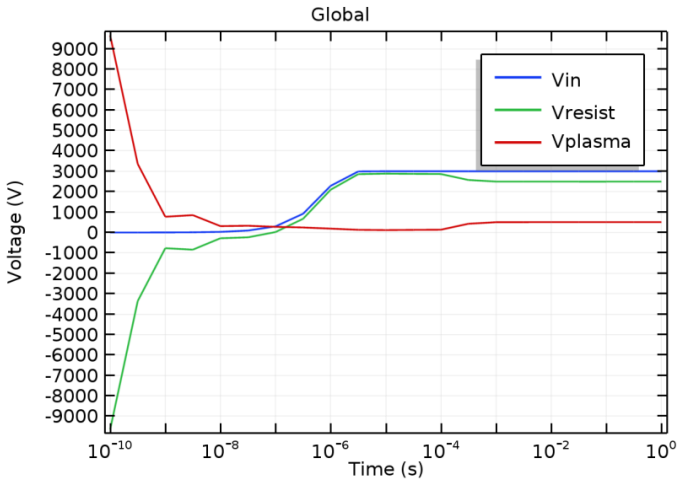

Global

3.7 CURRENT

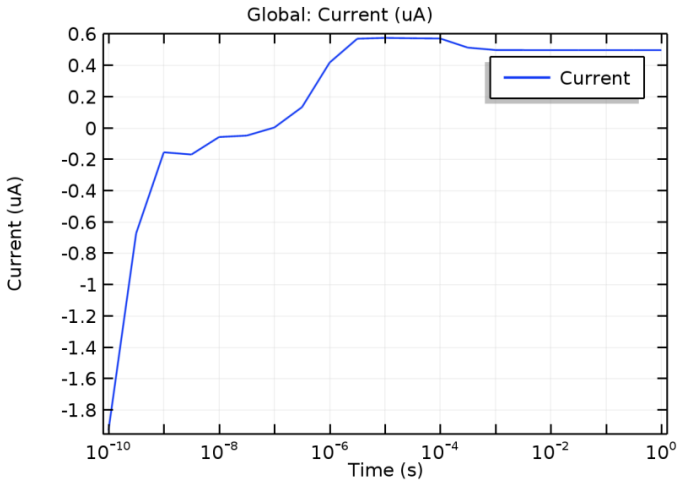

Global: Current (uA)

3.8 POWER SPENT ON PLASMA

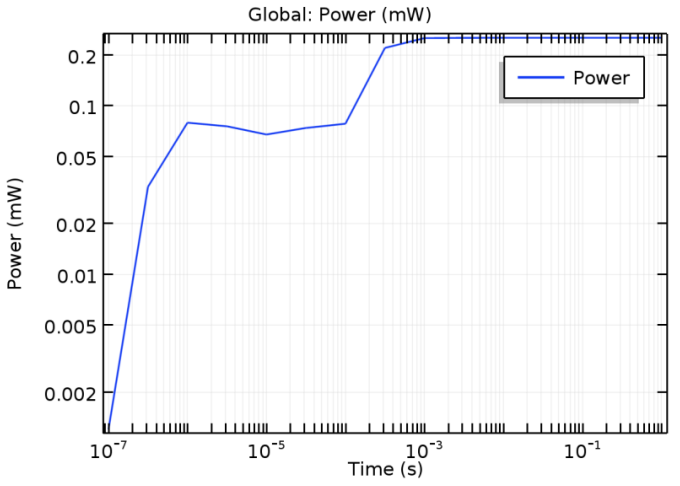

Global: Power (mW)

3.9 RESISTANCE OF PLASMA

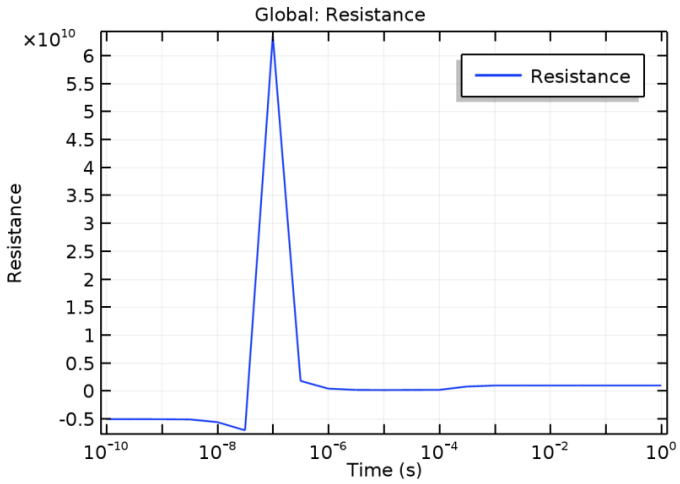

Global: Resistance

3.10 SECONDARY EMISSION ELECTRON FLUX

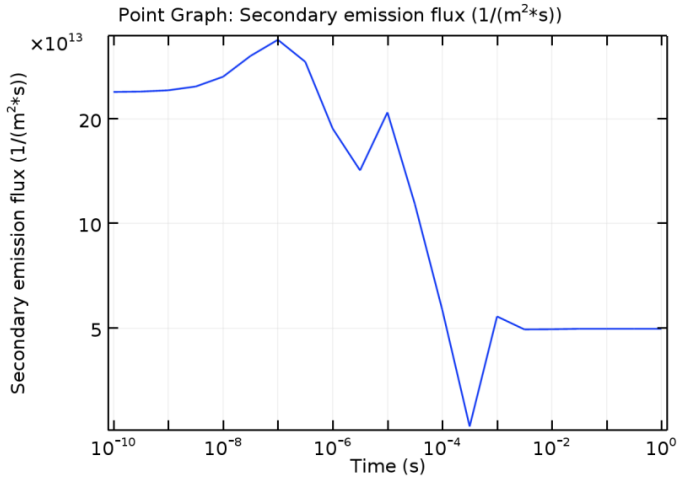

*Point Graph: Secondary emission flux (1/(m^2*s))*

3.11 NUMBER DENSITY N2

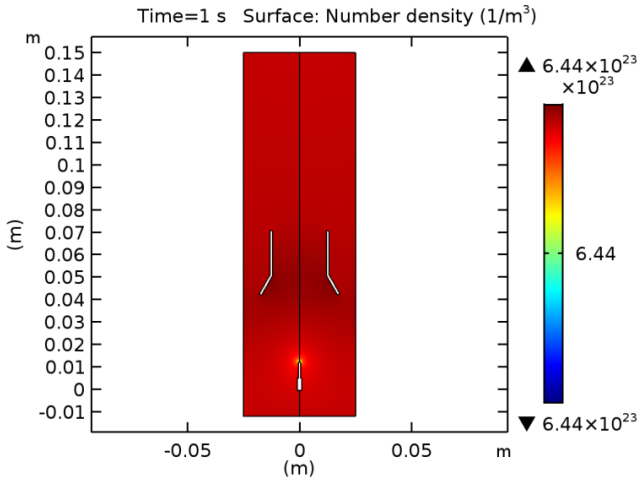

Time=1 s Surface: Number density (1/m³)

3.12 NUMBER DENSITY N

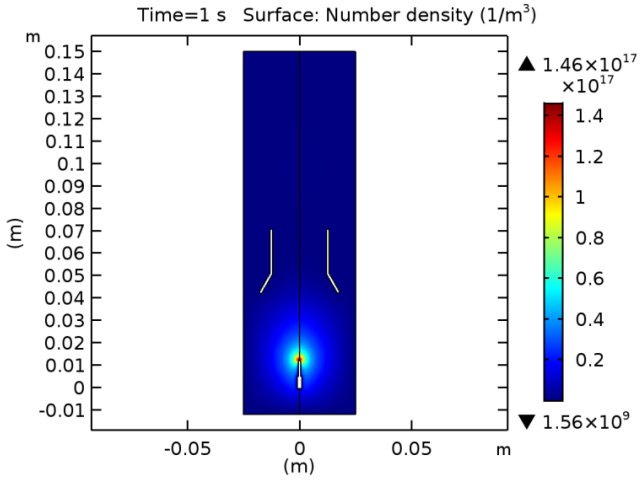

Time=1 s Surface: Number density (1/m³)

3.13 NUMBER DENSITY N+

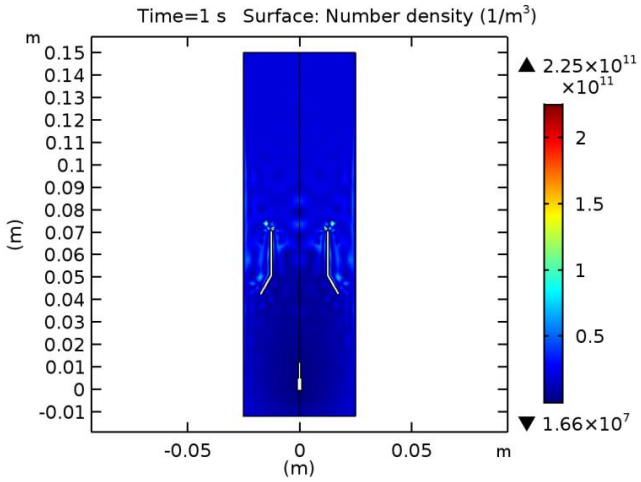

Time=1 s Surface: Number density (1/m³)

3.14 NUMBER DENSITY N4+

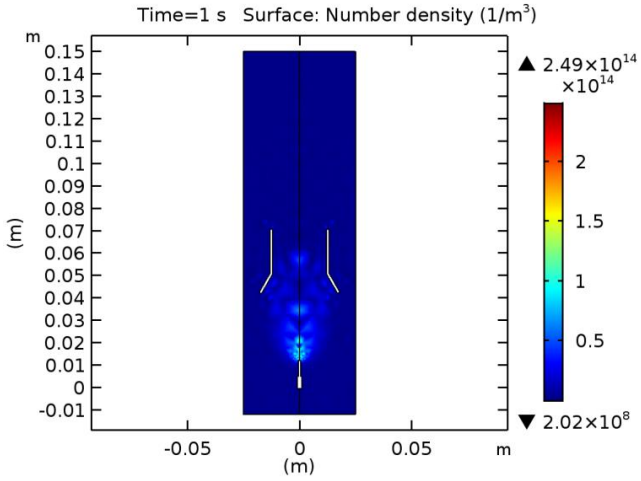

Time=1 s Surface: Number density (1/m³)

3.15 NUMBER DENSITY N2+

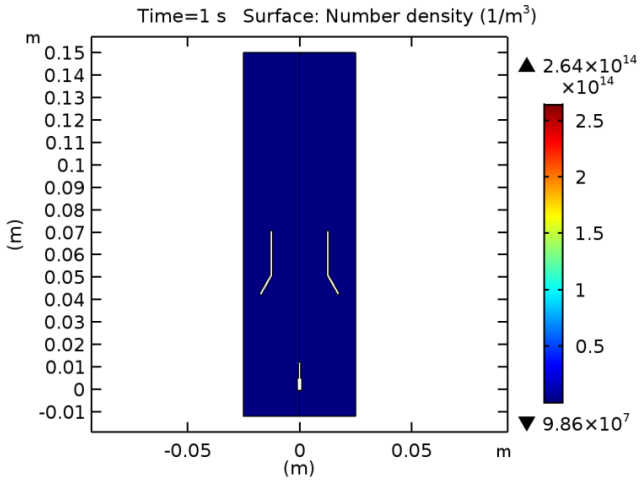

Time=1 s Surface: Number density (1/m³)

3.16 VELOCITY_LINE

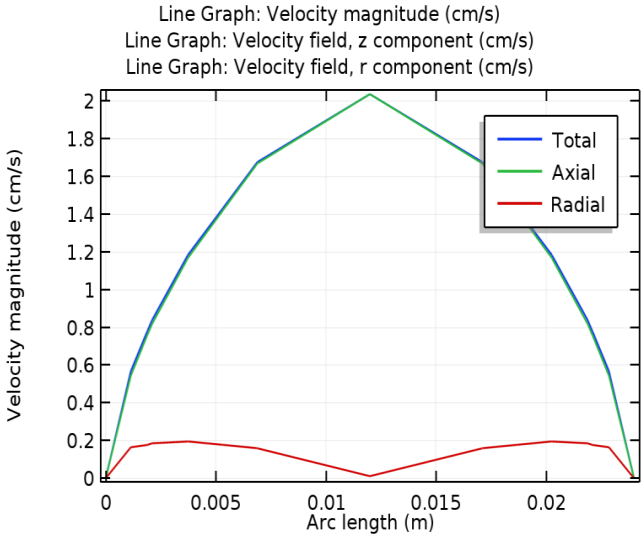

Line Graph: Velocity magnitude (cm/s) Line Graph: Velocity field, z component (cm/s) Line Graph: Velocity field, r component (cm/s)

References

I. Adamovich, S. D. Baalrud, A. Bogaerts, P. J. Bruggeman, M. Cappelli, V. Colombo, U. Czarnetzki, U. Ebert, J. G. Eden, P. Favia, D. B. Graves, S. Hamaguchi, G. Hieftje, M. Hori, I. D. Kaganovich, U. Kortshagen, M. J. Kushner, N. J. Mason, S. Mazouffre, S. Mededovic Thagard, H-R. Metelmann, A. Mizuno, E. Moreau, A. B. Murphy, B. A. Niemira, G. S. Oehrlein, Z. Lj. Petrovic, L. C. Pitchford, Y-K. Pu, S. Rauf, O. Sakai, S. Samukawa, S. Starikovskaia, J. Tennyson, K. Terashima, M. M. Turner, M. C. M. van de Sanden, and A. Vardelle. The 2017 Plasma Roadmap: Low temperature plasma science and technology. *Journal of Physics D: Applied Physics*, 50(32):323001, 2017. URL http://stacks.iop.org/0022-3727/50/i=32/a=323001.

W. P. Allis. *Motions of Ions and Electrons*, pages 383–444. Springer Berlin Heidelberg, Berlin, Heidelberg, 1956. ISBN 978-3-642-45844-6. doi: 10.1007/978-3-642-45844-6_5. URL https://doi.org/10.1007/978-3-642-45844-6_5.

S. Anthony. NASA's NEXT ion drive breaks world record, will eventually power interplanetary missions, December 2012. URL "https://www.extremetech.com/extreme/144296-nasas-next-ion-drive-breaks-world-record-will-eventually-power-interplanetary-missions".

A. Arefiev and B. Breizman. Magnetohydrodynamic scenario of plasma detachment in a magnetic nozzle. *Physics of Plasmas*, 12(4):043504, 2005. doi: 10.1063/1.1875632. URL http://link.aip.org/link/?PHP/12/043504/1.

L. Austin and H. Starke. Über die Reflexion der Kathodenstrahlen und die eine damit verbundene neue Erscheinung sekundärer Emission. *Ann. Phys. Lpz.*, 314:271, 1902.

E. Bering, F. Chang-Díaz, J. Squire, M. Brukardt, T. Glover, R. Bengtson, V. Jacobson, G. McCaskill, and L. Cassady. Electromagnetic ion cyclotron resonance heating in the VASIMR. *Advances in Space Research*, 42(1):192 – 205, 2008. ISSN 0273-1177. doi: 10.1016/j.asr.2007.09.034. URL http://www.sciencedirect.com/science/article/pii/S0273117707009787.

A. Blanco and S. Roy. Rarefied gas electro jet (RGEJ) micro-thruster for space propulsion. *Journal of Physics D: Applied Physics*, 50(45):455201, 2017. URL http://stacks.iop.org/0022-3727/50/i=45/a=455201.

V. Blickle, T. Speck, C. Lutz, U. Seifert, and C. Bechinger. Einstein relation generalized to nonequilibrium. *Phys. Rev. Lett.*, 98:210601, May 2007. doi: 10.1103/PhysRevLett.98.210601. URL https://link.aps.org/doi/10.1103/PhysRevLett.98.210601.

J. P. Boeuf. A two-dimensional model of DC glow discharges. *Journal of Applied Physics*, 63(5):1342–1349, 1988. doi: 10.1063/1.339961. URL https://doi.org/10.1063/1.339961.

J. P. Boeuf. Tutorial: Physics and modeling of hall thrusters. *J. Appl. Phys.*, 121:011101, 2017.

A. Bogaerts and R. Gijbels. Modeling of metastable argon atoms in a direct-current glow discharge. *Phys. Rev. A*, 52:3743, 1995.

H. Bondar and F. Bastien. Effect of neutral fluid velocity on direct conversion from electric to fluid kinetic energy in an electro-fluid-dynamic (efd) device. *J. Phys. D: Appl. Phys.*, 19:1657, 1986.

H. Bruining. *Physics and applications of secondary electron emission*. McGraw-Hil, 1954.

D. C. Byers. An experimental investigation of a high-voltage electron-bombardment ion thruster. *Journal of The Electrochemical Society*, 116(1):9–17, 1969. doi: 10.1149/1.2411785. URL http://jes.ecsdl.org/content/116/1/9.abstract.

F. X. Canning, C. Melcher, and E. Winet. Asymmetrical capacitors for propulsion. *Technical Report NASA/CR-2004-213312, National Aeronautics and Space Administration, Washington, DC*, 2004.

M. Capitelli, C. M. Ferreira, B. F. Gordiets, and A. I. Osipov. *Plasma Kinetics in Atmospheric Gases*, volume 31. Springer-Verlag, 1 edition, 2000. ISBN 978-3-642-08683-0. doi: 10.1007/978-3-662-04158-1.

M. D. Carter, F. W. Baity Jr, G. C. Barber, R. H. Goulding, Y. Mori, D. O. Sparks, K. F. White, E. F. Jaeger, F. R. Chang-Diaz, and J. P. Squire. Comparing experiments with modeling for light ion helicon plasma sources. *Physics of Plasmas*, 9:5097, 2002.

F. R. Chang-Diaz, J. P. Squire, A. V. Ilin, G. E. McCaskill, T. X. Nguyen, D. S. Winter, A. J. Petro, G. W. Goebel, L. Cassady, K. A. Stokke, et al. The development of the VASIMR engine. In *International Conference of Electromagnetics in Advanced Space Applications*, 1999.

C. Charles. Plasmas for spacecraft propulsion. *Journal of Physics D: Applied Physics.*, 42(16): 163001, 2009. doi: 10.1088/0022-3727/42/16/163001. URL http://stacks.iop.org/0022-3727/42/i=16/a=163001.

A. Chattock. On the velocity and mass of ions in the electric wind in air. *Philos. Mag.*, 48:401, 1899.

E. Choueiri. A critical history of electric propulsion: The first 50 years (1906-1956). *Journal of Propulsion and Power*, 20(2):193–203, 2004.

E. Choueiri. New dawn for electric rockets. *Scientific American*, 300:58–65, 2009. doi: 10.1038/scientificamerican0209-58.

E. Christenson and P. Moller. Ion-neutral propulsion in atmosphere media. *AIAA J.*, 5:1768, 1967. doi: 10.2514/3.4302. URL https://doi.org/10.2514/3.4302.

J. Chu. Electrohydrodynamic effect offers promise for efficient propulsion in air, April 2013. URL "http://lae.mit.edu/ehd/".

Comsol.com. COMSOL Multiphysics® Modeling Software, 2016. URL http://www.comsol.com.

P. Cooperman. A theory for space-charge limited currents with application to electrical precipitation. In *AIEE Trans., pages 47-50*, 1960.

N. P. Curran, M. B. Hopkins, D. Vender, and B. W. James. The effect of the addition of noble gases on H^- production in a dc filament discharge in hydrogen. *Plasma Sources Science and Technology*, 9(2):169, 2000. URL http://stacks.iop.org/0963-0252/9/i=2/a=309.

A. J. Dekker. Secondary electron emission. In Frederick Seitz and David Turnbull, editors, *Advances in Research and Applications*, volume 6 of *Solid State Physics*, pages 251 – 311. Academic Press, 1958. doi: 10.1016/S0081-1947(08)60728-6. URL http://www.sciencedirect.com/science/article/pii/S0081194708607286.

Z. Donkó. Apparent secondary-electron emission coefficient and the voltage-current characteristics of argon glow discharges. *Phys. Rev. E*, 64:026401, 2001. doi: 10.1103/PhysRevE.64.026401. URL https://link.aps.org/doi/10.1103/PhysRevE.64.026401.

R. L. Fitzwilson and L. M. Chanin. Positive ion ratio measurements in Ar, Kr, and Xe glow discharges. *Journal of Applied Physics*, 44(12):5337–5346, 1973. doi: 10.1063/1.1662153. URL http://dx.doi.org/10.1063/1.1662153.

A. Fridman and L. A. Kennedy. *Plasma Physics and Engineering*. Taylor & Francis, 2004. ISBN 1560328487. doi: 10.4324/9780203334874.

E. Fylladitakis. Review on the history, research, and applications of electrohydrodynamics. *IEEE Trans. Plasma Sci.*, 42:358, 2014.

D. M. Goebel and I. Katz. *Fundamentals of Electric Propulsion: Ion and Hall Thrusters*. JPL Space Science and Technology Series. Wiley, 2008. ISBN 9780470436264. URL https://books.google.pt/books?id=P5OGFXcBKcwC.

E. Gogolides and H. H. Sawin. Continuum modeling of radio-frequency glow discharges. I. Theory and results for electropositive and electronegative gases. *Journal of Applied Physics*, 72(9):3971–3987, 1992. doi: 10.1063/1.352250. URL https://doi.org/10.1063/1.352250.

B. F. Gordiets, C. M. Ferreira, V. Guerra, J. M. A. H. Loureiro, J. Nahorny, D. Pagnon, M. Touzeau, and M. Vialle. Kinetic model of a low-pressure N_2-O_2 flowing glow discharge. *IEEE Transactions on Plasma Science*, 23(4):750–768, Aug 1995. ISSN 0093-3813. doi: 10.1109/27.467998.

B. F. Gordiets, C. M. Ferreira, M. J. Pinheiro, and A. Ricard. Self-consistent kinetic model of low-pressure N_2-H_2 flowing discharges: I. Volume processes. *Plasma Sources Science and Technology*, 7(3):363, 1998a. URL http://stacks.iop.org/0963-0252/7/i=3/a=015.

B. F. Gordiets, C. M. Ferreira, M. J. Pinheiro, and A. Ricard. Self-consistent kinetic model of low-pressure N_2-H_2 flowing discharges: II. Surface processes and densities of N, H, NH_3 species. *Plasma Sources Science and Technology*, 7(3):379, 1998b. URL http://stacks.iop.org/0963-0252/7/i=3/a=016.

G. Gousset, C. M. Ferreira, M. J. Pinheiro, P. A. Sá, M. Touzeau, M. Vialle, and J. Loureiro. Electron and heavy-particle kinetics in the low pressure oxygen positive column. *Journal of Physics D: Applied Physics*, 24(3):290, 1991. URL http://stacks.iop.org/0022-3727/24/i=3/a=010.

V. H. Granados, M. J. Pinheiro, and P. A. Sá. Electrostatic propulsion device for aerodynamics applications. *Physics of Plasmas*, 23(7):073514, 2016. doi: 10.1063/1.4958815. URL http://dx.doi.org/10.1063/1.4958815.

V. H. Granados, M. J. Pinheiro, and P. A. Sá. Single-stage EHD thruster response to several simulation conditions in nitrogen gas. *Physics of Plasmas*, 24(9):093508, 2017a. doi: 10.1063/1.4986219. URL http://dx.doi.org/10.1063/1.4986219.

V. H. Granados, M. J. Pinheiro, and P. A. Sá. Study of the design and efficiency of single stage EHD thrusters at the sub-atmospheric pressure of 1.3 kPa. *Physics of Plasmas*, 24(12):123513, 2017b. doi: 10.1063/1.5018424. URL https://doi.org/10.1063/1.5018424.

J. T. Gudmundsson and A. Hecimovic. Foundations of DC plasma sources. *Plasma Sources Science and Technology*, 26(12):123001, 2017. URL http://stacks.iop.org/0963-0252/26/i=12/a=123001.

V. Guerra. Theoretical investigation of the influence of the wall temperature on the probability for surface atomic recombination of a single species. *Japanese Journal of Applied Physics*, 45 (10S):8200, 2006. URL http://stacks.iop.org/1347-4065/45/i=10S/a=8200.

V. Guerra, P. Sá, and J. Loureiro. Kinetic modeling of low-pressure nitrogen discharges and post-discharges. *Eur. Phys. J. Appl. Phys.*, 28(2):125–152, 2004. doi: 10.1051/epjap:2004188. URL "https://doi.org/10.1051/epjap:2004188".

G. J. M. Hagelaar and L. C. Pitchford. Solving the Boltzmann equation to obtain electron transport coefficients and rate coefficients for fluid models. *Plasma Sources Science and Technology*, 14 (4):722, 2005. URL http://stacks.iop.org/0963-0252/14/i=4/a=011.

F. Hauksbee. *Physico-Mechanical Experiments on Various Subjects*. R. Brugis, London, 1 edition, 1709.

A. Ieta and R. Ellis. Characterization of corona wind in a modular electrode configuration. In *Proc. ESA Annual Meeting on Electrostatics*, 2013.

IST-Lisbon. database www.lxcat.net. 2015. retrieved on January 25.

Itikawa. database www.lxcat.net. 2015. retrieved on January 25.

R. Jahn and E. Choueiri. Electric propulsion. *Princeton University, Encyclopedia of Physical Science and Technology*, 5:125–141, 2002.

N. Jewell-Larsen, S. Karpov, I. Krichtafovitch, V. Jayanty, C. Hsu, and A. Mamishev. Modeling of corona-induced electrohydrodynamic flow with COMSOL Multiphysics. In *Proc. ESA Annual Meeting on Electrostatics, Paper E1*, 2008.

I. J.E. Jordan. Electric Propulsion: Which one for my spacecraft? *Space Systems I course at JHU, Whiting School of Engineering*, 2000. URL http://www.stsci.edu/~jordan/other/electric_propulsion_3.pdf.

I. D. Kaganovich, Y. Raitses, D. Sydorenko, and A. Smolyakov. Kinetic effects in a Hall thruster discharge. *Physics of Plasmas*, 14(5):057104, 2007. doi: 10.1063/1.2709865. URL http://dx.doi.org/10.1063/1.2709865.

I. A. Kossyi, A. Yu Kostinsky, A. A. Matveyev, and V. P. Silakov. Kinetic scheme of the non-equilibrium discharge in nitrogen-oxygen mixtures. *Plasma Sources Science and Technology*, 1(3):207, 1992. URL http://stacks.iop.org/0963-0252/1/i=3/a=011.

S. Lam, C.-E. Zheng, D. Lo, A. Dem'yanov, and A. Napartovich. Kinetics of Ar_2^* in high-pressure pure argon. *J. Phys. D: Appl. Phys.*, 33(3):242, 2000. doi: 10.1088/0022-3727/33/3/310. URL http://stacks.iop.org/0022-3727/33/i=3/a=310.

M. A. Lieberman and A. J. Lichtenberg. *Principles of Plasma Discharges and Materials Processing*. John Wiley & Sons, Inc., 2005. ISBN 9780471724254. doi: 10.1002/0471724254.refs. URL http://dx.doi.org/10.1002/0471724254.refs.

V. A. Lisovskiy, S. D. Yakovin, and V. D. Yegorenkov. Low-pressure gas breakdown in uniform DC electric field. *Journal of Physics D: Applied Physics*, 33(21):2722, 2000.

J. Loureiro and C. M. Ferreira. Coupled electron energy and vibrational distribution functions in stationary N_2 discharges. *Journal of Physics D: Applied Physics*, 19(1):17, 1986. URL http://stacks.iop.org/0022-3727/19/i=1/a=007.

V. Lj. Marković, Z. Lj. Petrović, and M. M. Pejović. Surface recombination of atoms in a nitrogen afterglow. *The Journal of Chemical Physics*, 100(11):8514–8521, 1994. doi: http://dx.doi.org/10.1063/1.466750. URL http://scitation.aip.org/content/aip/journal/jcp/100/11/10.1063/1.466750.

M. Martínez-Sánchez and J. E. Pollard. Spacecraft electric propulsion: An overview. *J. Propul. Power*, 14:688, 1998.

K. Masuyama. Performance characterization of electrohydrodynamic propulsion devices. Master's thesis, Massachusetts Institute of Technology, September 2012. URL http://hdl.handle.net/1721.1/77114.

K. Masuyama and S. Barret. On the performance of electrohydrodynamic propulsion. In *Proceedings of the Royal Society, 469: 20120623*, 2013. doi: 10.1098/rspa.2012.0623.

J. W. McCormack. Space handbook: Astronautics and its Applications, Oct 2004. URL "https://history.nasa.gov/conghand/spcover.htm". Pursuant to H. Res. 496 (85th Cong.) USA.

H. Miyoshi, S. Ichimura, H. Kuninakat, K. Kuriki, and Y. Horiuchi. Microwave ion thruster with electron cyclotron resonance discharge. *22nd International Electric Propulsion Conference, IEPC-91-084, Viareggio, Italy, October 14-17*, 1991.

M. Miyoshi, N. Yamamoto, and H. Nakashima. Microwave discharge ion thruster using argon as a propellant. *30th International Electric Propulsion Conference, IEPC-2007-205, Florence, Italy September 17-20*, 2007.

P. A. Molina-Cabrera and N. Tolyarenko. The VASIMR engine: Benefits, drawbacks, and technological challenges. *32nd International Electric Propulsion Conference, Wiesbaden, Germany*, (IEPC-2011-251), 2011.

P. A. Molina-Cabrera, G. Herdrich, M. Lau, S. Fausolas, T. Schoenherr, and K. Komurasaki. Pulsed plasma thrusters: a worldwide review and long yearned classification. *32nd International Electric Propulsion Conference, Wiesbaden, Germany*, (IEPC-2011-340), 2011.

Morgan. database www.lxcat.net. 2015. retrieved on January 25.

T. F. O'Malley, A. J. Cunningham, and R. M. Hobson. Dissociative recombination at elevated temperatures. II. Comparison between theory and experiment in neon and argon afterglows. *J. Phys. B: Atom. Mol. Phys.*, 5(11):2126, 1972. doi: 10.1088/0022-3700/5/11/019. URL http://stacks.iop.org/0022-3700/5/i=11/a=019.

L. Pekker and M. Young. Model of ideal electrohydrodynamic thruster. *J. Propul. Power*, 27:786, 2011.

A. V. Phelps and S. C. Brown. Positive ions in the afterglow of a low pressure helium discharge. *Physical Review*, 86:102–105, 1952. doi: 10.1103/PhysRev.86.102. URL https://link.aps.org/doi/10.1103/PhysRev.86.102.

M. J. Pinheiro, C. M. Ferreira, and G. Gousset. *Multicomponent Reactive Gas Dynamic Model for Low-Pressure Discharges in Flowing Oxygen*, pages 485–494. Springer Netherlands, Dordrecht, 1996. ISBN 978-94-009-0267-1. doi: 10.1007/978-94-009-0267-1_31. URL http://dx.doi.org/10.1007/978-94-009-0267-1_31.

L. Prevosto, H. Kelly, and B. Mancinelli. Modelling of an atmospheric pressure nitrogen glow discharge operating in high-gas temperature regimes. *Plasma Chemistry and Plasma Processing*, 36(4):973–992, Jul 2016. ISSN 1572-8986. doi: 10.1007/s11090-016-9716-3. URL https://doi.org/10.1007/s11090-016-9716-3.

Y. P. Raizer. *Gas Discharge Physics*. Springer Science + Business Media, 1991. doi: 10.1007/978-3-642-61247-3. URL http://dx.doi.org/10.1007/978-3-642-61247-3.

M. Rickard, D. Dunn-Rankin, F. Weinberg, and F. Carleton. Maximizing ion-driven gas flows. *Journal of Electrostatics*, 64(6):368–376, 2006. doi: 10.1016/j.elstat.2005.09.005. URL https://doi.org/10.1016/j.elstat.2005.09.005.

M. Robinson. Movement of air in the electric wind of the corona discharge. *Transactions of the American Institute of Electrical Engineers, Part I: Communication and Electronics*, 80(2):143–150, 1961. doi: 10.1109/TCE.1961.6373091.

M. Robinson. A history of the electric wind. *American Journal of Physics*, 30(5):366–372, 1962. doi: 10.1119/1.1942021. URL https://doi.org/10.1119/1.1942021.

S. D. Rockwood. Elastic and inelastic cross sections for electron-Hg scattering from Hg transport data. *Physical Review A*, 8:2348–2358, Nov 1973. doi: 10.1103/PhysRevA.8.2348. URL https://link.aps.org/doi/10.1103/PhysRevA.8.2348.

S. D. Rockwood. Effect of electron-electron and electron-ion collisions in Hg, CO2/N2/He, and CO/N2 discharges. *Journal of Applied Physics*, 45(12):5229–5234, 1974. doi: 10.1063/1.1663221. URL https://doi.org/10.1063/1.1663221.

J. Roth. *Industrial Plasma Engineering*, volume 2. IOP Publishing Ltd, Bristol, 2001.

P. A. Sá, J. Loureiro, and C. M. Ferreira. Effects of electron-electron collisions on the characteristics of DC and microwave discharges in argon at low pressures. *J. Phys. D: Appl. Phys.*, 25:960, 1992.

A. Seversky. Ionocraft, 04 1964. Patent U.S. 3130945A.

V. Singhal and S. Garimella. Influence of bulk fluid velocity on the efficiency of electrohydrodynamic pumping. *Trans. ASME*, 127:484, 2005.

J. P. Squire, C. S. Olsen, F. R. Chang-Díaz, L. D. Cassady, B. W. Longmier, M. G. Ballenger, M. D. Carter, T. W. Glover, and G. E. McCaskill. VASIMR® VX-200 operation at 200 kW and plume measurements: Future plans and an ISS EP test platform. In *32nd International Electric Propulsion Conference*, 2011.

D. Staack, B. Farouk, A. Gutsol, and A. Fridman. DC normal glow discharges in atmospheric pressure atomic and molecular gases. *Plasma Sources Science and Technology*, 17(2):025013, 2008.

G. Sutton. Rocket Propulsion. "http://www.accessscience.com/content/rocket-propulsion/592500", 2000.

G. Sutton. *Rocket propulsion elements - An introduction to the engineering of rockets (7th edition)*. Wiley-Interscience, 2000.

E. Tatarova, F. Dias, C. Ferreira, V. Guerra, J. Loureiro, E. Stoykova, I. Ghanashev, and I. Zhelyazkov. Self-consistent kinetic model of a surface-wave-sustained discharge in nitrogen. *J. Phys. D: Appl. Phys.*, 30:2663, 1997.

T. Townsend Brown. A method for and an apparatus or machine for producing force or motion, GB300311 (A), November 1928.

H. Wang, V. S. Sukhomlinov, I. D. Kaganovich, and A. S. Mustafaev. Ion velocity distribution functions in argon and helium discharges: detailed comparison of numerical simulation results and experimental data. *Plasma Sources Science and Technology*, 26(2):024002, 2017. URL http://stacks.iop.org/0963-0252/26/i=2/a=024002.

J. Wilson, H. Perkins, and W. Thompson. An investigation of ionic wind propulsion. *NASA technical reports*, page 43, 2009. Washington, DC, USA.

R. Wirz, J. Polk, C. Marrese, and J. Mueller. Development and testing of a 3cm electron bombardment micro-ion thruster. *IEPC Paper 01-343, 27th IEPC, Pasadena, CA*, 2001.

A. Wootton. *An Introduction to plasma physics*. University of Texas at Austin, 1997.

X. Wu. V2 rocket technology, August 2014. URL "http://v2.x-factorial.com/".

L. Young. An overview of advanced concepts for near-space systems. *AIAA Paper*, pages 2009–4805, 2009.

L. Zhao, K. Adamiak, and M. Mazumder. Numerical and experimental studies of the electrohydrodynamic pump for sampling system on mars. In *Proc. ESA Annual Meeting on Electrostatics, Paper O3*, 2008.